2017

# Matrix-Isolation Studies of Ionic CO2 Clusters and Improvements on the Counter Ion Co-Deposition Technique

Michael Edward Goodrich
*Lehigh University*

# Matrix-Isolation Studies of Ionic $CO_2$ Clusters And Improvements on the Counter Ion Co-Deposition Technique

by

Michael Edward Goodrich

A Dissertation

Presented to the Graduate and Research Committee

of Lehigh University

in Candidacy for the Degree of

Doctor of Philosophy

in

Chemistry

Lehigh University

May 2017

Approved and recommended for acceptance as a dissertation in partial fulfillment of the requirements for the degree of Doctor of Philosophy

Michael Goodrich

Matrix-Isolation Studies of Ionic $CO_2$ Complexes and
Improvements on the Counter Ion Co-Deposition Technique

_____

Defense Date

_____

Dr. Xiaoji Xu

_____

Approved Date

Committee Members:

_____

Dr. David T. Moore

_____

Dr. Gregory S. Ferguson

_____

Dr. James Roberts

_____

Dr. Nicholas Strandwitz

## ACKNOWLEDGMENTS

I would like to begin by thanking my high school chemistry teacher, Mr. John Munday, who inspired my interest in chemistry. I dedicate this dissertation to his memory.

To my research advisor, Dr. David Moore: Thank you for being a wonderful teacher and mentor over these past five years, and of course, for teaching me that "you gotta want it."

Thank you to the rest of my dissertation committee, Dr. Ferguson, Dr. Roberts, Dr. Strandwitz, and Dr. Xu, for your guidance and support.

I would like to thank my former lab mates, especially Ryan Ludwig, who was a great mentor and friend throughout our time in the Moore group.

Succeeding in graduate school would not have been possible without the constant encouragement and support of my parents, my wife Kim, and countless friends.

I would especially like to thank Kim for her love and unending support during my time in graduate school, and for always being there to talk me off the ledge when I was convinced I wasn't going to make it through. I couldn't have done it without you!

## TABLE OF CONTENTS

## LIST OF FIGURES

## LIST OF TABLES

## Abstract

This dissertation presents work performed using the counter ion co-deposition technique to deposit ions in a controlled manner for matrix-isolation spectroscopy experiments. Matrix-isolation experiments involving ionic species require that both anions and cations be present in the matrix, which the counter ion co-deposition technique achieves by externally generating separate beams of anions and cations, combining them in a quadrupole bender, and co-depositing the combined ion beam with a cryogenic matrix. The conditions under which ions are deposited into a cryogenic matrix can significantly impact the formation and behavior of the resulting ionic species observed in the matrix. These results provide insights into the mechanism by which matrix-isolated species are formed. This dissertation presents results examining the behavior of matrix-isolated species formed in $CO_2$ and CO-doped matrices formed following co-deposition of ions under a variety of experimental conditions.

Co-deposition of $Cu^-$ with a counter cation in a $CO_2$-doped matrix produces $CuCO_2^-$ and a number of ionic nonmetal $CO_2$ species. Ionic $CO_2$ complexes, which have been previously observed in argon and neon matrices, are identified in nitrogen and krypton matrices for the first time. High-energy deposition of $Ar^+$ without a specific anionic counter ion alters the behavior of the ionic $CO_2$ complexes. These experiments reveal that two anionic $CO_2$ dimers, $(CO_2)(CO_2^-)$ and $C_2O_4^-$, undergo a reversible conversion with temperature, and analysis shows the two species are in thermodynamic equilibrium. A complete kinetic analysis of the system was performed, and the thermodynamic and kinetic characterizations of the system produced results in agreement with one another. The equilibrium process is endothermic and driven by a substantial

increase in entropy. The exact nature of the entropy increase is yet to be understood, but may arise from the surrounding matrix environment, rather than the two species involved in the equilibrium. Comparison of the system with existing gas-phase studies provided interesting insight into the role of the matrix in the stabilization of the dimeric $CO_2$ anions.

The formation of matrix-isolated copper carbonyl anions following deposition of $Cu^-$ and $Ar^+$ into a CO-doped argon matrix had a strong dependence on the temperature at which the matrix was deposited. At constant CO concentration, lower deposition temperatures favored the formation of $CuCO^-$, while high temperatures favor the formation of $Cu(CO)_3^-$. This behavior appears to be a result of the rate at which deposited species become trapped in the matrix. Lower deposition temperatures result in more efficient trapping, which prevents the formation of highly coordinated copper carbonyls and solvation complexes.

The final results presented in this dissertation are of initial experiments performed following an improvement of the counter ion co-deposition system to allow simultaneous mass resolution of both the anionic and cationic beam. The addition of a second mass resolving quadrupole allowed the use of more complex counter ion gases while maintaining the desired level on control over ionic species deposited in the matrix. A single ionization product of a gas that fragments upon ionization can now be selected for deposition. For the first time, with the counter ion co-deposition system, a specific IR active counter ion could be deposited, so there are both anionic and cationic spectroscopic signatures in the matrix following deposition. The presence of a cationic spectroscopic signature allowed clear tracking of the fate of electrons in photolysis

experiments. Photodetached electrons from anionic species combined with the cation in the matrix, producing its neutral analogue. Future experiments should make use of the expanded capabilities of the counter ion co-deposition instrument, including the potential to generate complex cations in a chemical ionization source, as well as generating anions in the chemical ionization source allowing for co-deposition experiments of metal cations.

# Chapter 1

## Matrix Isolation Spectroscopy and its Application for the Study of Ionic Species

### 1.1 Matrix Isolation Spectroscopy

Although chemists are often primarily interested in understanding intermolecular interactions and reactions, understanding the structure and properties of a molecule is paramount to understanding its reactivity. Obtaining the unperturbed molecular spectrum of a species often requires gas-phase experiments, as a molecule in a condensed phase will be perturbed by interactions with its neighbors. Additionally, highly reactive molecules, such as ions and radicals, often have very short lifetimes and are thus difficult to study spectroscopically. Such species require fast characterization methods, or a stabilization technique allowing characterization on standard experimental time scales. The matrix-isolation technique was developed by Pimentel to provide a means for structural characterization of highly reactive molecules or ions *via* stabilization in a cryogenic solid.[1, 2] Matrix isolation involves trapping the guest species of interest in an inert matrix, most commonly a noble gas, which is condensed over time on a cold surface until a spectroscopically relevant concentration of trapped species is built up. Matrix isolation spectroscopy experiments necessitate low temperature, as the matrix will begin to sublime above approximately one third of the melting point of the matrix material.[3] As a result, an argon matrix will begin to sublime above ~30K, and a neon matrix will begin to sublime above ~10K. Such low temperatures require that matrix isolation experiments be performed in a high-vacuum environment. Experimental design is dictated by the requirement of keeping the matrix cold in a vacuum environment while being able to

study the matrix spectroscopically. Common methods of analysis include UV-Vis, FTIR, and electron spin resonance spectroscopy.

Species of interest are trapped in a rigid cage formed by the solid matrix, which isolates them from other potential reactants.[3-5] Spectra obtained using the matrix-isolation technique are considered to be close to a true molecular spectrum because the inert matrix only weakly perturbs the trapped species. For this reason, the applications of matrix isolation spectroscopy have expanded beyond the original scope of trapping reactive species. Matrix isolation has been widely used as a technique for obtaining spectral information for a vast number of organic and inorganic molecules. Two reviews by Jacox provide a reference for over 3000 ions and molecules which have been spectroscopically characterized using the matrix isolation technique.[6, 7] In addition to the matrix cage effect acting as a physical barrier between reactants, the low temperature of the matrix ensures a low-energy environment, so isolated species are trapped in low energy states and only minimal energy is available for reactions to occur.[8, 9] This effect can extend the short lifetime of a highly reactive species to a timescale that is spectroscopically relevant.

### 1.1.1 Matrix Materials

The only two properties required for a matrix material is that it remain rigid over the temperature range required for the experiment, and that it is optically transparent in the spectral region of interest. For most matrix-isolation experiments, noble gases are chosen as the matrix gas because they lack an infrared signature and are highly inert, which minimizes the interaction between the matrix and the isolated species.[3, 5] Argon and neon are the most commonly used matrix materials in the literature, though krypton and xenon are also utilized as matrix gases.[3] Nitrogen is another common choice for a

matrix gas, as it is inert and lacks spectroscopic signal, similar to the noble gases. In some cases a more reactive matrix material is used, such as CO or $O_2$, because the interaction between the trapped guest molecule and the matrix material itself is of interest.[3, 4]

### 1.1.2 Crystal Structure of the Matrix

Three models have been proposed to explain the crystal structure of cryogenic matrices. The single crystal model treats the matrix as a single, homogeneous crystal and is the simplest model.[3] It has the advantage that the crystal structures of many common matrix materials are known. Additionally, the possible sites where trapped molecules could exist are well defined. Unfortunately, due to the conditions under which matrices are formed, specifically at very low temperatures and over a large surface area, the true structure of the matrix is not a single crystal.[4, 5] The glassy model suggests that the matrix consists of a completely random arrangement of atoms. The arrangement of atoms is similar to that of a liquid or a completely amorphous solid. Matrix trapping sites and the number of nearest neighbors would be random, which would lead to the broadening of spectral bands of the matrix isolated species. One of the striking features of a matrix isolated spectrum is very narrow bands, so a purely glassy arrangement of matrix atoms is unlikely to be the true structure of the matrix.

The most accurate model for the structure of a cryogenic matrix is the microcrystalline model.[10] The matrix is considered to have small regions of atoms arranged in a crystalline manner separated by regions of atoms with an amorphous arrangement, which are treated like grain boundaries. Crystalline regions are believed to account for roughly half of the bulk solid, with the remaining half being in an amorphous

state.[3] Unfortunately, this model is difficult to treat quantitatively. As the matrix is rigid at experimentally relevant temperatures, there is no requirement that isolated crystalline regions have the same orientation or even the same crystal structure, and there are a large number of possible trapping environments at the boundaries between the crystalline and amorphous regions. Due to these limitations, it is most common to model the matrix as a single crystal, while understanding that perturbations may arise due to the true structure of the matrix.

The most stable crystal structure of the commonly used noble gas matrix materials is face-centered cubic.[3, 11] Each atom in this arrangement has twelve nearest neighbors and has octahedral, $O_h$, symmetry. These gases can also crystallize in a hexagonal close-packed arrangement. The hexagonal close packed arrangement is only slightly less thermodynamically stable, so it may still form during deposition. Atoms in this arrangement still have twelve nearest neighbors, but the symmetry of each site is lowered to $D_{3h}$. The presence of small amounts of nitrogen or oxygen in solid argon is known to stabilize the hexagonal close packed arrangement,[11] so it is possible that other impurities, or trapped species of interest, could lead to this arrangement.

### 1.1.3 Trapping Sites

Interstitial sites in the matrix lattice are the simplest locations where species could be trapped. A close-packed arrangement of spheres only fills approximately 74% of the available space, and in theory the remaining space could be filled by matrix isolated molecules. The two types of interstitial sites in a cubic close packed lattice are tetrahedral and octahedral, with four and six neighboring atoms.[3] The tetrahedral sites are too small to be occupied by an isolated species, as only a sphere with diameter of at most ¼$^{th}$ the

size of the lattice atoms could occupy the space.[3] Octahedral sites are larger, allowing a sphere up to one half the diameter of the lattice atom to fit without distortion. Thus, hydrogen atoms could occupy these sites, and with some distortion of the matrix lattice, larger atoms could occupy these sites.[10, 12]

Due to size limitations of interstitial lattice sites, it is much more likely for atoms and molecules to occupy substitution sites, in which a matrix atom in the lattice is replaced by the trapped species. Due to their size, atoms will tend to occupy single substitution sites, in which the guest atom replaces a single matrix atom in the lattice.[3] Additionally, very small molecules such as $H_2$ can occupy a single substitution site in matrices formed with larger atoms.[10] In general, any trapped species larger than the smallest molecules will occupy multiple substitution sites, in which multiple continuous matrix atoms in the lattice are displaced by the trapped species.[4] A single substitution site will have twelve nearest neighbors. A double substitution site will have eighteen unevenly distributed nearest neighbors and will occupy an approximately cylindrical shape. Multiple trapping orientations become possible for species occupying larger than a double substitution site. A triple substitution site can take the shape of a cylinder, if three atoms in a row are replaced, or it can take a triangular shape. These two sites have 24 and 22 nearest neighbors, respectively.[3, 4]

The substitution site containing the trapped molecule is referred to as the matrix cage, and as the size of the cage grows (more atoms in the lattice replaced), the potential shapes of the cage and number of nearest neighbors also continue to grow. It is generally believed that the shape of the cage orients itself to the molecule trapped inside, and that the effect of the cage on the lattice is not localized to the replaced atoms, such that some

longer range perturbations to the lattice are experienced.[3] Any molecule larger than a diatomic will occupy at least a triple substitution site with a minimum 22 nearest neighbors and larger molecules can occupy significantly more complex sites. Due to the potentially large number of nearest neighbors, larger molecules are less likely to be fully isolated from other guest molecules in the matrix.[3]

### 1.1.4 Annealing and Diffusion

In matrix-isolation experiments, the matrix is rigid below 30% of the melting point of the matrix material.[3] Below this threshold, trapped species and the surrounding matrix are considered to be immobile. This consideration is important for interpreting spectra of the matrix because temperature induced changes in the matrix can create complications for analysis. Annealing of the matrix occurs between 30% and 50% of the melting point.[3] Annealing of the matrix can result in the rearrangement of the crystal structure of the matrix. A microcrystalline or glassy matrix will begin to form larger regions of uniform crystallinity, and cages surrounding trapped molecules can rearrange to form more stable sites.[4, 5] While some small atoms and molecules can diffuse freely in a matrix, diffusion of larger species can typically only occur above 50% of the melting point of the matrix.[3] Above this temperature threshold, the matrix is no longer considered rigid. Experimentally, diffusion is unsustainable as the matrix will evaporate too quickly at these temperatures.

There is minimal control over conditions in the matrix during deposition. Since the matrix gas must be cooled from room temperature to the deposition temperature, there is a time period between when reactive species are initially deposited on the matrix surface and when they can be considered trapped. During this period, they are assumed to

diffuse and react with other guest species. To minimize this diffusion period, matrices should be deposited at a temperature below 30% of the melting point to ensure they are rigid, and a slow deposition rate ensure the refrigerator has ample cooling power to quickly cool the matrix to a rigid state. As is in Chapters 3 and 5, depositing at a higher temperature to extend the diffusion period can result in the appearance of new and interesting species not observed following deposition at lower temperatures.

### 1.1.5 Probability of Isolation

In theory, the caging effect of the matrix creates a physical barrier isolating guest molecules trapped in the matrix. The likelihood of a guest molecule being fully isolated depends on the size of the cage the molecule occupies, the concentration of guest species in the matrix, and strength of interaction between guest molecules. Guest molecules with very weak intermolecular interactions have a probability being isolated given by

$$P = (1 - r)^n \tag{1.1}$$

where r is the matrix ratio, the ratio of the number of guest molecules to matrix atoms, and n is the number of nearest neighbors, or number of matrix atoms forming the cage.[3] Carbon monoxide, for example, occupies a single substitution site in an argon matrix,[13] which has twelve nearest neighbors. If a matrix contained 1% CO, the likelihood that CO is isolated would be $P = (1 - \frac{1}{100})^{12} = 0.886$, so there is a 88.6% chance that the CO molecule does not have another CO molecule as one of its twelve nearest neighbors. The likelihood of isolation effectively decreases as the intermolecular forces between guest molecules increases. For example, if the force could be felt through the first layer of cage

atoms, the percent of truly isolated molecules would decrease. This calculation also shows the importance of ensuring the matrix gas being used has high purity, as even 1% impurities result in over 10% of sites having a non-matrix atom nearest neighbor. Table 1.1, which has been adapted from Reference 3, shows the probability that a guest molecule is completely isolated as a function of concentration.

**Table 1.1 Probability of Isolation as a Function of Molecule Size and Strength of Interaction***

| Matrix Ratio | 100 (1%) | 1000 (0.1%) | 10,000 (0.01%) |
|---|---|---|---|
| **Single Site, Weak Interaction** | | | |
| **% isolated** | **88.6** | **98.8** | **99.9** |
| **% non-isolated** | **11.4** | **1.2** | **0.1** |
| **Multiple Site, Weak Interaction** | | | |
| **% isolated** | **29.3** | **88.5** | **98.8** |
| **% non-isolated** | **70.7** | **11.5** | **1.2** |
| **Single Site, Strong Interaction** | | | |
| **% isolated** | **42.1** | **91.8** | **99.1** |
| **% perturbed** | **41.3** | **6.4** | **0.7** |
| **% dimerized** | **16.5** | **1.8** | **0.2** |

***Adapted from Tables 2.4, 2.5, and 2.6 in reference 3

### 1.1.6 Matrix Effects on Spectroscopy

An attractive aspect of matrix isolation spectroscopy is that it provides an alternative to gas phase spectroscopic methods to obtain molecular spectra, though a matrix-isolated spectrum is not a true, isolated gas phase spectrum and therefore is subject to some perturbations.[11, 14] The position of peaks in the spectrum can change, as can the number of peaks and their shape. The peak position can shift due to the interaction of the matrix with the trapped molecule.[3] This shifting can be especially apparent with ions, and the degree of shifting depends on the polarizability of the matrix material. In the study of metal carbonyl ions, for example, Andrews observed smaller shifts in the spectra of species trapped in neon than those trapped in argon. He attributed

this difference to a stronger interaction between the argon matrix and the trapped species, due to the increased polarizability of argon compared to neon.[15] A single type of molecular vibration can yield multiple peaks in a matrix isolated spectrum due to the variety of orientations in which a molecule can be trapped in the matrix cage. Multiple orientations can yield slightly shifted peaks due to differing strengths in the interaction between the matrix and the trapped species.[16] The difference in shape between a gas-phase and matrix-isolated spectrum will depend on the spectroscopic technique. Matrix-isolated vibrational spectra, which will be predominantly discussed in this dissertation, are generally simpler than their gas phase counterparts, as the caging effect of the matrix prevents all but the smallest molecules from rotating, eliminating ro-vibrational bands from the spectrum.[3]

Since spectroscopy is the only characterization tool available for matrix isolation experiments, assigning species in the matrix to observed spectral bands can be difficult. A combination of techniques is employed to arrive at band assignments, including comparison to existing gas phase spectra, computational techniques, and isotopic substitution. Isotopic substitution results in shifting of vibrational bands due to the dependence of vibrational frequency on the reduced mass of the oscillator, and the expected shift can be calculated based on the change in reduced mass upon isotopic substitution. Additionally, deposition of a matrix consisting of a known mixture of isotopes can aid in the assignment of spectral bands due to splitting patterns due to isotopic substitution.[17] Photolysis experiments can be used to detect ionic species trapped in matrices. Irradiation with sufficiently energetic light can result in the photodetachment of the extra electron in anionic species, resulting in the formation of the corresponding

neutral species. Wavelength-dependent irradiation of the matrix can provide information about the relative binding energies of different matrix-isolated anions.[18]

### 1.1.7 Reaction Kinetics in Matrix-Isolation

Very early after its development, Pimentel recognized the potential to study the rates of chemical reactions using the matrix-isolation technique.[19] He proposed that due to the properties of the matrix, reactions with very low activation barriers of one or two kilocalories per mole could be studied. Several classes of reactions were suggested for kinetic study using the matrix-isolation technique, including the deactivation of an excited state, or simple bond-breaking or bond-forming reactions. He posited that the matrix cage would affect these processes, so the calculated activation energy would shift from the gas phase dependent on the matrix environment.[19] For example, reactions involving the breaking of a bond would be influenced by the size of the cage relative to the transition state, or the matrix may hinder motion along the reaction coordinate, which would introduce a barrier to reaction dependent upon the ability of the trapped species to diffuse within the matrix.[20] Similarly, for bond-formation reactions, if the formation requires an isolated species to diffuse through the matrix, the enthalpy of diffusion will have an effect upon the overall rate of reaction.[4] Isomerization processes can also be influenced by the matrix. A study by Ozin observed the formation of the trigonal bipyramidal isomer of $Cr(CO)_5$ upon deposition, which only rearranged to the thermodynamically stable square pyramidal isomer following annealing of the matrix.[21] In such cases, the activation barrier to rearrangement is likely to exceed the gas phase barrier due to the influence of the matrix cage. In Chapter 4, kinetics measurements will

be utilized to characterize the reversible interconversion of two isomers of dimeric $CO_2$ anions.

## 1.2 Ion Generation for Matrix-Isolation Studies

The results presented in this dissertation discuss the characterization of ionic species trapped in cryogenic matrices. Any matrix isolation experiment involving ions is limited by the requirement that the matrix remains electrically neutral. Since noble gas matrices are insulators, there must be a balanced number of anions and cations in the matrix, or a charge will build up on the matrix which repels the addition of further ions of one type or the other. Therefore, any method for delivering or generating ions for matrix isolation experiments must ensure that both anions and cations are present in the matrix. The earliest matrix-isolation experiments to study ions used an *in situ* photoionization process to generate ions from deposited precursor molecules. An example of this early method, an argon matrix was deposited containing Na atoms to act as electron donors, and $B_2H_6$ to act as an electron acceptor. Electron spin resonance spectroscopy was used to observe $B_2H_6^-$ following photolysis of the matrix.[22]

### 1.2.1 High-Energy Deposition of Externally Generated Ions

One technique for ensuring charge balance is to use high-energy processes that generate both anions and cations in close proximity to the matrix. Ions are swept up with the matrix gas and deposited on the cold IR window. Two prominent examples of this technique are laser ablation and microwave discharge sources. The laser ablation technique was first developed by Bondybey,[23] and Andrews is well known for using the technique to obtain the spectra for a vast range of matrix-isolated metal-ligand complexes.[24-28] A high-energy pulsed laser is focused on a rotating metal target,

generating a plume of metal atoms, positively charged metal ions, and electrons. The electrons can attach to neutral atoms resulting in the generation of metal anions. This method is inherently neutral as an equal number of cations and electrons will be generated in the process. The laser ablation target is located in close proximity to the cold deposition window, and the ablated metal species are co-deposited along with the matrix gas of choice. The high laser power also ensures the ejected species have sufficiently high energy to undergo reactions with the dopants in the matrix gas.

Jacox and Andrews both used microwave discharge techniques which form anions and cations *via* a Penning ionization mechanism, generating ions through collisions between electronically excited gas phase atoms and the target molecule.[29, 30] Early experiments performed *via* microwave discharge of argon created experimental complications because precursor molecules were introduced in the ionization region, including isotope mixing and large amounts of atomization. Jacox later developed an improved ionization method that used neon as the discharge gas and eliminated many of the complications by introducing the matrix gas and precursor molecules outside the ionization region.[31] Similar to laser ablation, this method produces both anions and cations in an external source, and relies on each being trapped in the matrix to ensure charge balance.

### 1.2.2 Deposition of Mass-Selected Cations

The Maier group was the first to introduce mass selection by coupling ion delivery to the output of a mass spectrometer.[32] Molecular ions were generated in an electron-impact ionization source and were directed into a mass-selecting quadrupole. In these studies, deposition of mass selected $C_2N_2^+$ led to the observation of bands assigned

to the mass selected ion as well as to fragment ions including $C_2^+$ and $N_2^+$. Maier estimated cation number densities of $10^{16}$ $cm^{-3}$, but no anionic spectroscopic signals were observed. Due to the high density of cations, anions must also be trapped in the matrix, so he hypothesized that the high energy (150+ eV) of the cation beam was sufficient to induce secondary ionization events of either the matrix or grounded metal of the sample holder, which could result in the formation of anions. This hypothesis was later confirmed in a study by the Leroi group,[33] in which they observed the formation of $CO_2^-$ radicals following the deposition of a high-energy cation beam. They suggested that precursor $CO_2$ molecules were trapped on surrounding metal, and were ejected upon ionization and trapped in the matrix. Coupling ion-deposition with mass spectrometry provided a higher degree of control over the deposited ions when compared to the methods employed by Jacox and Andrews. Directing an externally generated beam of mass selected ions into the matrix also reduced the complexity of the spectrum by limiting the number of trapped ionic species, though fragment ions were still observed as a result of high deposition energy. Several groups have successfully employed this method for the controlled deposition and observation of cationic species.[34-38]

### 1.2.3 The Counter Ion Co-Deposition Method

Maier's technique improved the control over ion delivery for matrix isolation by introducing mass selection, though the method cannot be used at arbitrary energies because high energy deposition is required for counter ion generation in the matrix. An attempt to deposit a beam of anions and cations simultaneously was made by focusing two mass spectrometers onto a cold matrix window by Leroi, but this was approach ultimately unsuccessful and no ion signal was observed in the resulting spectra.[39]

However, attempts in our group to simultaneously deposit anions and cations while coupling mass selection were successful through use of a quadrupole ion bender.[40, 41] Beams of anions and cations were externally generated and combined in a bender, and then a single combined beam was deposited into the matrix. The counter ion co-deposition technique was developed in the Moore group, and first demonstrated by Ryan Ludwig, a previous group member. The technique allows low-energy deposition of a mass-selected anion beam by simultaneously co-depositing a beam of low-energy cations. A beam of anionic metal ions is generated and passes through a mass resolving quadrupole, before being directed into a quadrupole ion bender.

A beam of noble gas counter ions are generated in an electron impact ionization source and guided into the opposite side of the bender. Due to the construction of the bender, oppositely charged ion beams entering opposite sides will be combined and exit as a single beam of ions. The combined beam then passed through an octopule ion guide, whose output was directed at the deposition window. Charge balance was ensured by depositing an equal current of anions and cations, as detected at a Faraday plate. In addition to the control the method provided over the species of ions deposited into the matrix, this technique also allows ions to be deposited at low energy, thus minimizing secondary ionization processes. This approach provides significantly more control over the ion species present in the matrix compared to previous ion deposition methods, which in turn results in simpler spectra to interpret. The clear limitation to the counter ion co-deposition technique in this form, however, is the lack of mass resolution of the counter ion beam. As stated above, earlier attempts at simultaneously depositing multiple mass selected beams of ions into a matrix were unsuccessful. An improvement on the original

design of the counter ion co-deposition technique that allows simultaneous deposition of both anions and cations is discussed in Chapter 6.

### 1.3 Matrix-Isolated Metal Carbonyls

Chapters 5 and 6 both focus on the behavior of copper carbonyls as a function of various matrix- and ion-deposition conditions. The counter ion co-deposition technique was originally intended to be used to study the mechanism of CO oxidation on metals, because it was believed that the matrix environment would provide a highly controlled environment for these mechanistic studies. As a test system, we were interested in studying CO oxidation on copper, as copper carbonyls have been well characterized in cryogenic matrices. Unexpected difficulties with the catalysis project arose, but copper carbonyls were still used extensively to study other deposition parameters, because changes in the well-understood behavior of the matrix isolated copper carbonyls could be easily tracked.

Copper carbonyls can be characterized in matrix isolation spectroscopy by the shift in the CO stretching mode. Both neutral and anionic copper carbonyls result in a red shift of the CO stretching frequency from the neutral free CO stretching frequency appearing at 2138 $cm^{-1}$.[13] Cationic copper carbonyls are blue-shifted from the free CO peak. Neutral copper carbonyls were first characterized in matrix-isolation experiments by Ozin and Moskovits.[42] A molecular beam of neutral copper atoms generated in a Knudsen oven source was deposited into a CO-doped argon matrix at 10K or 15K. They were able to assign peaks corresponding to CuCO, $Cu(CO)_2$, $Cu(CO)_3$, and $Cu_2(CO)_6$. Multiple peaks for each complex were attributed to site effects, as each should only produce one vibrational mode. Ozin and Moskovits proposed a formation mechanism for

the copper carbonyl neutrals which assumed only Cu and CO were mobile in the matrix. Following the formation of CuCO, larger complexes formed via stepwise additions of CO molecules that diffused toward the existing metal CO complex.

Ionic copper carbonyls were characterized in argon and neon matrices by Andrews and coworkers using the laser-ablation technique.[15] Anionic analogues for the three mono-copper carbonyls, $CuCO^-$, $Cu(CO)_2^-$, and $Cu(CO)_3^-$, were observed to be red-shifted from the neutral species. In neon matrices, three cationic analogues were observed, but interestingly, in an argon matrix, only $CuCO^+$ was observed. This result was explained by the difference in polarizability between neon and argon. Due to argon's increased polarizability, it has stronger interaction with the positively charged copper cation, with the electron cloud of the argon atoms limiting the ability for the neutral CO molecules to complex with $Cu^+$.

Andrews observed anionic, cationic, and neutral copper carbonyls upon deposition of the matrix. Use of the counter ion co-deposition technique resulted in a simplified spectrum containing only copper carbonyl anions upon deposition. Photolysis of the matrix using a visible light source resulted in the photodetachment of the anionic electron, forming the neutral copper carbonyl analogues. This gentle process preserved the ratio of the mono-, di-, and tricarbonyls. This example provides an illustration of the importance of the improved ion delivery technique. The low energy and mass-selection results in a simplified spectrum, and allows experiments directed at greater understanding of a specific set of species in the matrix.

## 1.4 Dissertation Outline

Chapter 2 discusses the design and operation of the custom ion co-deposition and matrix-isolation system, as well as the procedure for data collection and analysis. It includes a discussion of my significant modification to the instrument provided the ability to deposit two simultaneously mass-selected beams of anions and cations. Chapters 3 and 4 focus on results of experiments performed on $CO_2$-doped matrices. Chapter 3 includes a discussion of the behavior of ionic $CO_2$ clusters dependent upon ion deposition conditions, as well as interesting new spectroscopic features observed following deposition at high temperature. Chapter 4 presents an analysis of a thermodynamic equilibrium of two anionic $CO_2$ dimers, $(CO_2)(CO_2^-)$ and $C_2O_4^-$. It was known previously that annealing a matrix containing the separated dimer species resulting in the formation of the oxalate-like $C_2O_4^-$ species, but our experiments revealed that cooling the matrix caused the oxalate-like species to convert back to the separated dimer. A full thermodynamic and kinetic analysis, as well as comparison with existing gas phase $(CO_2)_n^-$ cluster data, is included. Chapters 5 and 6 present results on CO doped matrices using the counter ion co-deposition technique. Chapter 5 is a case study showing the relationship between deposition temperature and the formation of matrix isolated copper carbonyl anions, $Cu(CO)_x^-$ ($x = 1 - 3$). Chapter 6 discusses the first results obtained following the instrument modification allowing for simultaneous deposition of mass selected anions and cations. Low and high energy mass selected $SF_5^+$ or $SF_3^+$ is co-deposited with $Cu^-$ into a CO doped argon matrix. I believe this is the first instance of multiple mass selected ions being successfully deposited into a matrix. The results of the

initial test systems are presented, and the broader implications of having the ability to deposit multiple mass selected ions is discussed.

# Chapter 2

# Experimental Methods

## 2.1 Introduction

This chapter explains the methods used for operation of the counter ion co-deposition and matrix-isolation instrument. The design and assembly of the original instrument was carried out by Dr. David Moore and a previous graduate student, Alex Hunter. Modifications to the magnetron sputtering source, as well as the generation of the first mass spectral data from the instrument were also carried out by Alex Hunter. Ryan Ludwig was responsible for obtaining the first matrix-isolation data, including FTIR as well as UV-Vis spectra, creating the general format for experiments carried out using the instrument, and the general method for data analysis. My contributions include the installation of an additional chamber to the instrument, which contains components allowing the deposition of two simultaneously mass-selected beams of ions. Simultaneous deposition of mass selected ions is discussed in Chapter 6.

This chapter begins a general overview of the operation of the instrument. This includes both the original configuration as well as highlighting the functions of the new chamber. The operating principles of the three ion sources in the system are discussed, as are the procedures for creating gas mixes for matrix isolation experiments using our gas rack mixing station. Finally, the chapter concludes with an explanation of the procedure for data analysis and treatment of spectra using the Origin Lab software.

## 2.2 Counter Ion Co-Deposition and Matrix-Isolation Instrument Overview

The matrix isolation instrument was developed with the specific purpose of allowing highly controlled ion deposition into a cryogenic matrix. Two configurations of the instrument were used for experiments described in this dissertation. The original instrument allowed for mass selection of a single beam of anions, which was balanced by a cationic beam generated in an electron-impact ionization source. A diagram of the original instrumental design is shown in Figure 2.1. A significant modification to the instrument provided the means for simultaneous mass selection of both anions and cations through the installation of an additional chamber containing a mass resolving quadrupole and two additional ion sources, and is discussed later in this chapter.

The original matrix isolation instrument consisted of four differentially pumped chambers and two ion sources. Specific details of the pumps and pressure measurement for each chamber are provided in the Appendix (Table 2.1). The instrument maintained an ultrahigh vacuum (UHV) with typical base pressures on the order of $2x10^{-9}$ Torr in order to minimize contamination from water and $CO_2$ during matrix deposition. A magnetron sputtering source (Oxford Applied Research NC200U-B, heavily customized) was used to generate a beam of metal ions. Anions or cations were extracted by applying a positive or negative voltage to a 6.25 mm nozzle attached to the end of the aggregation region of the magnetron. From the sputtering source, the beam passed through a series of ion optics which were designed by Randy Pedder at Ardara Technologies. The quadrupoles and ion optics were controlled using the Tempus Data system. The beam of metal ions was collimated in an RF-only 22-mm quadrupole ion guide. The desired metal ion cluster size was selected in a 9-mm RF/DC mass resolving quadrupole. The mass-

selected metal ion beam was then directed into a quadrupole bender, where the metal ion beam was combined with a beam of counter ions. The bender also prevented the deposition of neutral metal clusters by removing a direct path from the magnetron to the deposition window.

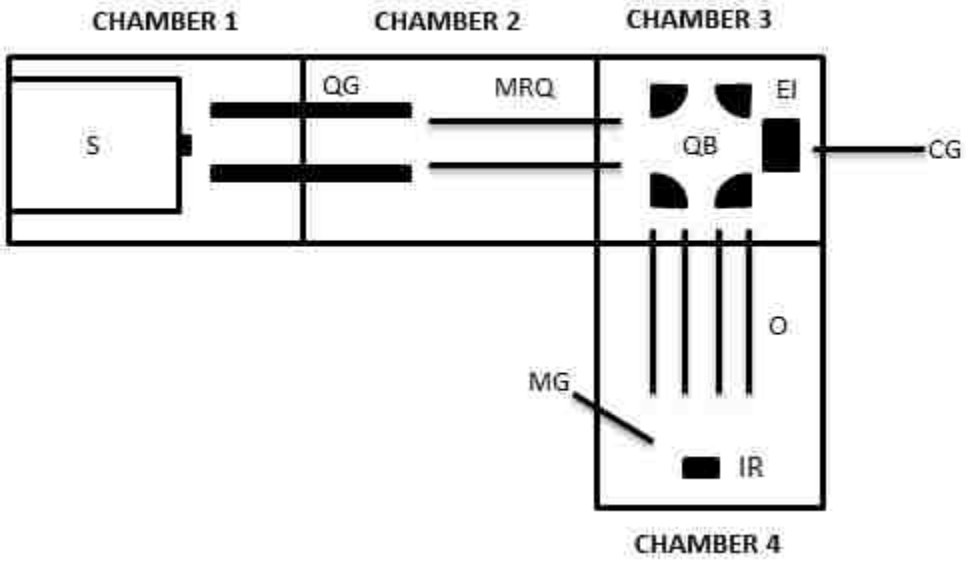


**Figure 2.1:** Original design of the counter ion co-deposition and matrix isolation system: Magnetron sputtering source (S) generates metal species, guided by a quadrupole ion guide (QG) to a mass resolving quadrupole (MRQ). The counter ion gas (CG) is flowed into an electron impact ionizer (EI). Mass resolved anion beam and cations enter opposite sides of a quadrupole bender (QB) and are turned into octupole ion guide (O), or an electron multiplier (not shown) for detection. Ions are deposited on an IR window (KBr or CsI) cooled by a closed cycle helium cryostat coupled to a rotatable, translatable flange. The matrix gas (MG) is introduced into the system and directed onto the IR window. Figure adapted from Reference 40.

In the original instrumental design, counter ions were generated in an electron impact ionization source (EI, Figure 2.1). Cations generated in the source were fed directly into the quadrupole bender. The counter ion gas was delivered directly into the ion region of the source by a 1/16” stainless steel line. The counter ion gas flow was controlled by an Alicat Scientific MC series mass flow controller with a range of 0.01 to

1 standard cubic centimeters per minute (SCCM). A counter ion gas flow rate of 0.2 to 0.3 SCCM was used for operation of the EI source to achieve the desired beam current.

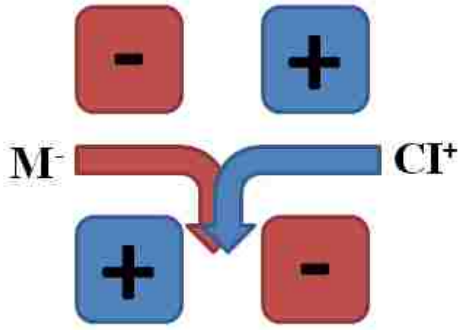


**Figure 2.2:** Schematic illustration of a quadrupole ion bender. The positively and negatively biased poles allow oppositely charged ion beams entering opposite sides of the bender to be combined and exit as a single beam. Note that the positive and negative voltages are not necessarily equal.

The metal-ion beam and counter-ion beam entered opposite sides of a quadrupole bender. The operating principle of quadrupole ion benders dictate that if a beam of anions and a beam of cations enter the bender on opposite sides, the two beams will exit the bender as a coincident beam, given the appropriate voltages are applied to the poles of the bender. Externally combining the oppositely charged ion beams is the key principle of the counter ion co-deposition technique. It allows ions with arbitrary energies to be deposited for matrix isolation experiments. From the bender, the combined ion beams can be directed into an electron multiplier for detection, or into an octupole ion guide.

The output of the octupole directs the beam into the deposition chamber. The deposition window is coupled to a 4K closed-cycle helium cryostat (Advanced Research Systems: Expander model DE-202, Compressor model ARS-4HW), mounted on a rotatable, vertically translatable vacuum flange (McAllister Technical Services). The

temperature of the cryostat was controlled by a PID controller (Lakeshore 331). The temperature was monitored with a silicon diode sensor mounted on the sample holder and a 50-W heating band coiled around the second stage of the cryostat was used to warm the sample holder. The matrix and ions were deposited on either a KBr or CsI window (Koch Crystal Finishing) with a $0.5^{o}$ wedge, which served to minimize etaloning observed in collected spectra. Early experiments were performed on KBr windows, which were subject to cracking after repeated heating and cooling cycles, and therefore required periodic replacement. Later experiments were performed on a wedged CsI window, which was more robust. The matrix gas was delivered through 1/16" stainless steel line directed at the window, with approximately a two inch gap between the window and the output. The matrix gas flow was controlled by an Alicat Scientific MC Series mass flow controller with a variable rate of 1-10 sccm. The matrix gas was delivered at either 3 or 10 SCCM for most experiments described in this dissertation, and the matrix was generally deposited for a period of four or six hours. More details of the deposition chamber are provided in section 2.2.2.

Species present in the matrix were detected *via* FTIR using a Thermo Nicolet 6700 spectrometer with an external liquid nitrogen cooled MCT-A detector. The spectrometer has a maximum resolution of 0.125 $cm^{-1}$. Most spectra presented in this dissertation were taken at 0.5 $cm^{-1}$ resolution, with high resolution scans being taken at 0.125 $cm^{-1}$. To improve signal-to-noise ratios, most 0.5 $cm^{-1}$ resolution spectra are averages of 500 or 1000 scans, which required 15 or 30 minutes to collect. High-resolution scans have more noise, so high-resolution spectra were the result of a minimum of 1000 averaged scans, and were typically 1500 or 2000 scans, requiring a

minimum of two hours for collection. Data processing was performed using the Origin 8 software. Baseline correction was performed by fitting a polynomial to the original spectrum, and the residuals were plotted as the baselined spectrum. This correction did not alter appearance of spectral features.

Following deposition of the matrix, standard matrix-processing steps were performed, including photolysis experiments and annealing. Emission spectra of the light sources used for photolysis experiments are shown in the appendix Figures 2.10 and 2.11. A spectrum was collected following each annealing or irradiation step, so changes in the matrix induced by the processing could be tracked. Most spectra presented were collected at 10K to minimize thermal fluctuations in absorbance. Experiments were performed under darkened conditions (lab lights, ion gauges, and RGA turned off) as ambient light could trigger the photodetachment of matrix-isolated anionic species.

### 2.2.1 Instrument Modifications to Allow for Simultaneous Mass Selection of Ions

A block diagram of the upgraded matrix-isolation instrument is shown in Figure 2.3, with the changes to the instrument being contained in a new differentially pumped chamber, labelled Chamber 5. In the updated instrument, counter ions were generated in either a second EI source (EI Figure 2.3) or chemical ionization (CI) source. As with the original design, the counter-ion sources were situated on the opposite side of the original quadrupole bender from the magnetron sputtering source. The update provided the means for mass selection of the counter ion beam, as well as the ability to generate additional classes of counter ions, including anionic counter ions in the CI source. The new EI source and the CI source were mounted on opposite sides of a new quadrupole bender.

The ion beam generated in either source was bent into a new mass resolving quadrupole. From the quadrupole, the beam of mass selected ions entered the original EI source (not depicted in Figure 2.3), which simply acted as an ion lens, focusing the beam into the original quadrupole bender, where the counter ion beam was combined with the metal ion beam. The new chamber and CI source was designed and constructed by Randy Pedder at Ardara technologies. The quadrupole (model 150 QC) and electron impact ionization source were built by Extrel. The quadrupole, ion sources, and ion optics were controlled using the Merlin data system software and power supply, constructed by Extrel.

A new counter ion gas line was constructed for the EI source. The CI source had a separate gas line which was directly attached to the high pressure region of the source. The gas delivery was still regulated by the AliCat flow controller, and the flow rate required for the operation of the new EI source was approximately 0.03 SCCM. Due to complications with the operation of the CI source, it was not used in any experiments presented in this dissertation.

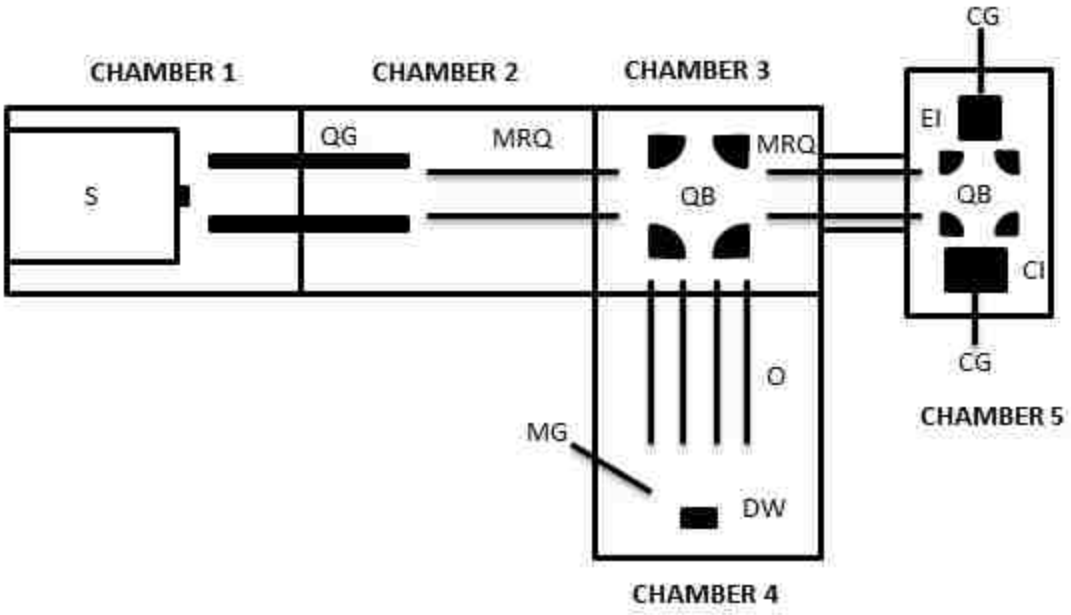


**Figure 2.3:** Block diagram of the updated instrument showing the fifth differentially pumped chamber. The four original chambers remained unchanged. Counter ions are now generated in the electron impact (EI) or chemical ionization (CI) sources in chamber 5. The output of the two ion sources direct the counter ion beams into a bender, where they are directed into a new mass resolving quadrupole (MRQ), where the beam can be mass selected for a specific counter ion. The original electron impact ionization source (EI, Figure 2.1) is still present and acts as an ion guide between the new mass resolving quadrupole and the original bender, but is not shown in the figure. As with the original system, the two ion beams are combined in the bender and directed into the octupole ion guide and onto the deposition window.

### 2.2.2 Matrix-Deposition Chamber

An image of the matrix deposition chamber taken from the perspective of where the IR beam enters the chamber is shown in Figure 2.4. The IR window was coupled to a closed-cycle helium cryostat (Advanced Research Systems CS204SF-X20B), which was mounted on a rotatable and translatable vacuum flange. This arrangement allowed the location of the window to be adjusted as necessary throughout the experiment. In Figure 2.4, the window is shown perpendicular to and in the line of site of the output of the octupole, the configuration it would be in for deposition of the matrix and ions. For

perspective, the matrix gas delivery line, which is just visible in the top of the image, was located approximately two inches from the IR window. Before deposition, the matrix window was translated vertically upwards, out of the line of site of the octupole exit, so the ion beams could impinge upon a Faraday plate directly behind the window. The Faraday plate is connected to a pre-amplifier (Advanced Research Instruments, PMT-5R), which could then be connected to either the Tempus or Merlin data system for detection of current and mass spectral data. During photolysis experiments, light was introduced through the view port which is visible just behind the Faraday plate.

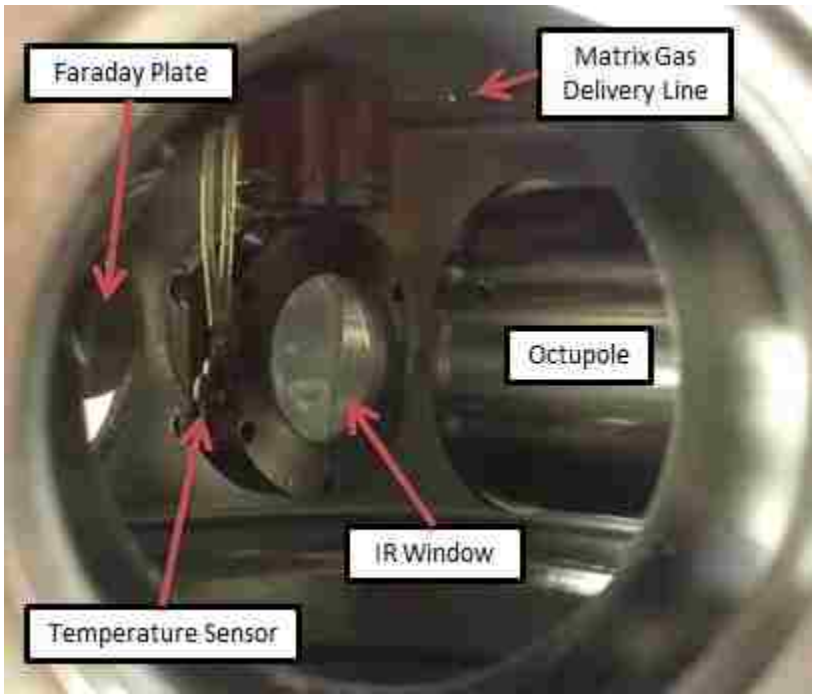


**Figure 2.4:** Image of the deposition chamber taken from the perspective of the flange where the external IR beam enters the chamber, showing the orientation of the IR window relative to the octupole output, matrix gas line, and Faraday plate.

For collection of spectra, the cryostat was rotated 45$^{o}$, such that the IR window was perpendicular to the incoming IR beam. The window was then perpendicular to the perspective from which the image in Figure 2.4 was taken. The IR beam entered and exited the chamber through KBr windows in differentially pumped flanges. A series of

optical mirrors guided the IR beam from the spectrometer through the deposition chamber, and into an external liquid nitrogen cooled MCT-A detector, which has a detection range of 650 – 4000 $cm^{-1}$. The spectrometer and entire beam path was kept under constant purge by a continuous flow of dried compressed air which has passed through a FT-IR purge gas generator (Parker Balston 75-62) to remove $H_2O$ and $CO_2$. The beam path through the deposition chamber is illustrated in Figure 2.5

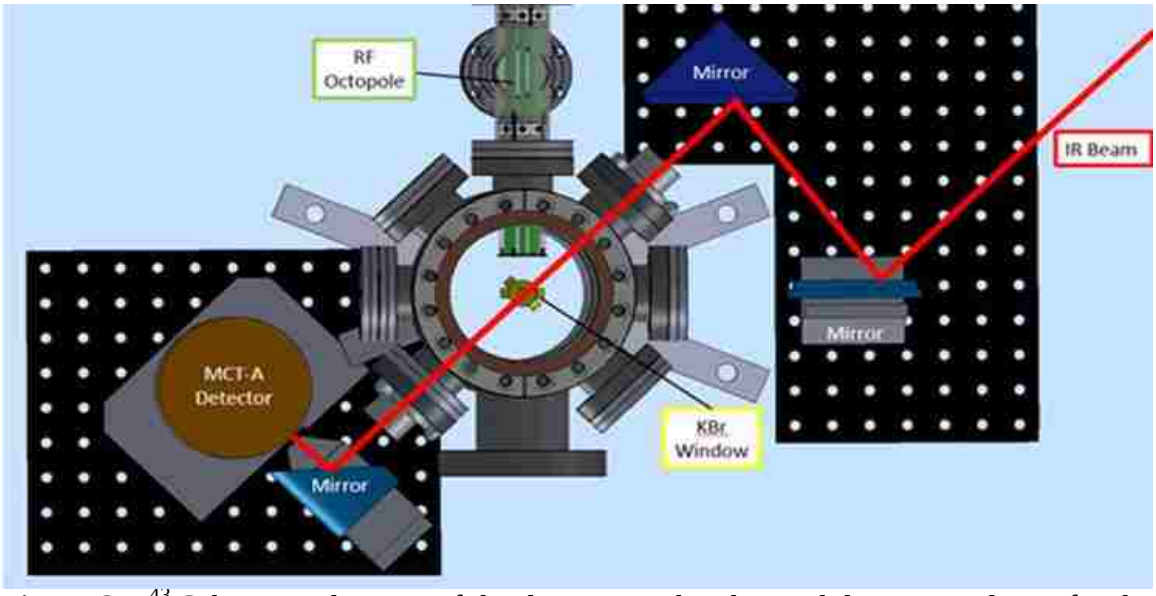


**Figure 2.5**:[43] Schematic diagram of the deposition chamber and detection scheme for the matrix isolation instrument which shows the direction of the IR beam path through the deposition chamber and into the external MCT-A detector. SolidWorks file created by Alex Hunter. Figure taken from Reference 43.

## 2.3 Ion Generation and Delivery

### 2.3.1 Metal-Ion Generation

The metal-ion source was a modified OAR magnetron sputtering source, a commercially available version of the source developed by Haberland.[44, 45] A schematic diagram of the OAR magnetron sputtering nanocluster source is shown in Figure 2.6. A metal sputtering target was situated upon a permanent magnet, which also acted as the

cathode. Argon was flowed continuously into a small ~0.3 mm gap between the anode and cathode, and a high-voltage controller is used to spark an argon plasma. Ionized $Ar^+$ was accelerated into the negatively biased cathode with enough force to eject metal atoms from the sputtering target.[46] The magnet holds a high density of electrons in close proximity to the sputtering target, and sputtered metal atoms can by ionized as they pass through the argon plasma, resulting in the generation of both metal anions and cations. When using a copper target, 20-50% of sputtered atoms will be ionized.[47]

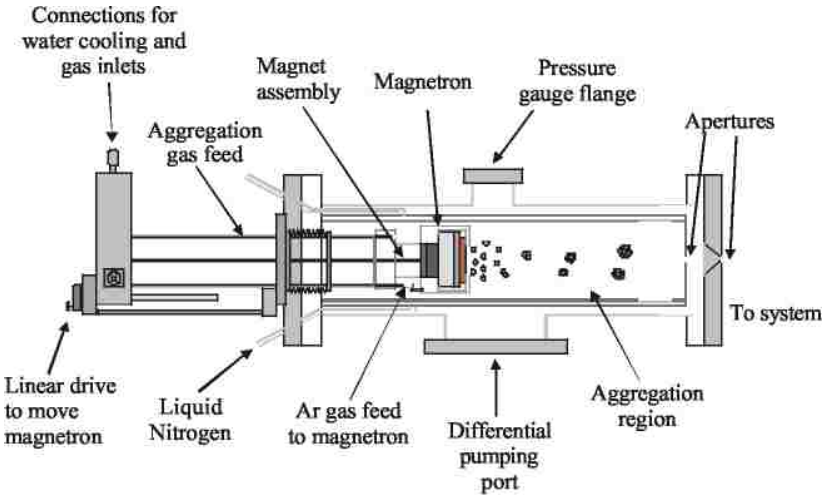


**Figure 2.6:**[48] Schematic diagram of unmodified OAR magnetron sputtering source taken from Reference 44. The aggregation region was water cooled, rather than liquid nitrogen cooled, as shown in the figure. The length of the aggregation chamber could be modified using the linear drive. The custom nozzle (not shown) to improve ion extraction was installed at the left aperture, as labeled in the figure.

Metal atoms and ions should aggregate into larger clusters, and the size of the clusters can theoretically be controlled by adjusting the length of the aggregation region. Additionally, changing the pressure in the aggregation region by introducing an inert gas, either helium or argon, should yield further control over cluster size, but unfortunately, production of size selected larger clusters has proven difficult, and only a high enough current of copper monomers and dimers has been produced for experiments. A 6.25 mm

nozzle, to which a voltage of up to +/- 400V can be applied, was added to the source to assist with extraction of metal anions or cations. In a typical matrix isolation experiment, a 4-5 nA beam of copper monomer anions was generated. In initial tests selecting copper monomer cations, beam currents of 15 nA were detected at the Faraday plate. The current generated could be varied by adjusting source parameters including sputter gas flow, aggregation chamber length, and voltage applied to the nozzle. As the metal ion beam was the limiting reagent in co-deposition experiments, ion optics were adjusted to maximize the metal current detected at the Faraday plate. Standard 2" metal sputtering targets were purchased from Kurt J. Lesker. In the experiments presented in this dissertation, either 99.9% or 99.99% Cu targets were used, though the purity was found to not affect experimental results.

### 2.3.2 Counter Cation Generation and Charge Balance

All of the experiments involving ions in this dissertation used one of the two electron-impact ionization (EI) sources in the instrument. Electron-impact ionization sources generate cations through collisions between gas-phase atoms and molecules with energetic electrons. A hot filament generates electrons, which then strike neutral gas molecules. The electrons have sufficient energy to ionize the target atom or molecule, which for most experiments described in this dissertation was argon. Upon ionization the gas-phase ions are accelerated out of the source. Due to the charge balance requirement of the matrix, the current of the metal anion and counter cation beams were balanced at the Faraday plate prior to initiating deposition. Since the current of the metal anions was limiting, the shared beam optics from the bender through the octupole were optimized to ensure maximum transmission of the metal anion beam. Therefore, to balance the current

of the beams, conditions of the EI source were modified to balance the current, including counter ion gas flow rate, filament emission current, and the voltage applied to the ion extraction plate.

### 2.3.3 Ion Energy

As discussed in the Introduction, an advantage of the counter ion co-deposition technique is the ability to deposit ions at low energy, minimizing the energy available for secondary ionization processes to occur upon deposition of ions. The energy of an ion is dictated by the energy of the electric field that it feels upon ionization, also known as the birth potential. The EI sources used in the matrix isolation instrument have a metal cage surrounding the filament, which is referred to as the ion region. The voltage applied to the cage sets the energy of the ion beam generated by the ionizer.

The energy of the ion beam was tested by performing a stopping-potential experiment. The current of the ion beam was measured as a function of the voltage applied to the octupole exit lens, which was the final optic before the deposition chamber. The first derivative of this curve produced a peak showing the distribution of the energy of the ion beam, where the peak was taken to be the energy of the beam. Figure 2.9 in the Appendix shows the energy of $Ar^+$ counter ion beams measured using stopping potential experiments as a function of the voltage applied to the ion region of the EI source.

A typical counter ion co-deposition experiment used low energy cations, in the range of 20 – 50 eV. Some experiments made use of high energy $Ar^+$ to induce secondary ionization events to balance the charge of the matrix, rather than through the co-deposition of a specific beam of anions. This technique achieved charge balance in a manner similar to the work performed by Maier and others who deposited high-energy,

mass-selected cations.[49] These experiments were performed by generating high energy $Ar^+$ or $Kr^+$ ions in the EI source by setting the ion region to between 350 – 400V. Stopping potential experiments found that setting the voltage of the ion region to 350V resulted in an ion beam with an approximate energy of 300 eV, and applying a 400 V potential to the ion region resulted in the generation of ions with energy of approximately 350 eV. Examples of stopping potential curves are provided in Chapter 6, Figures 6.7 – 6.8.

Although the voltage of the ion region provided fairly accurate control over the energy of the cation beam, no method existed for altering the energy of the metal anion beam. Increasing the voltage applied to the nozzle of the magnetron sputtering source as high as +400V was found to have no effect on the stopping potential of the anion beam. Regardless of source conditions, the energy of the $Cu^-$ beam was found to be approximately 10 eV. It was hypothesized that a layer of gas-phase ions near the nozzle shielded a central beam of ions from the bias applied to the nozzle, such that only the inner layer of ions that had not been influenced by the nozzle survived to be detected.[43]

### 2.3.4 Chemical Ionization Source

The final ion source in the instrument is a chemical ionization (CI) source, which can be used to generate either positive or negative ions. Although none of the experiments described in this dissertation utilized the CI source, the installation process and initial optimization of the source was a large part of the work I performed during my time in the Moore group. I will describe the operation principle in this section, as the CI source has the potential for use in potentially exciting future experiments. An image of the CI source with labelled components is shown in Figure 2.7. Chemical ionization

sources require relatively high gas pressure, on the order of $10^{-2}$ Torr up to ~1 Torr, for successful operation. As such, the CI source is contained in its own differentially pumped chamber within chamber 5, as denoted in Figure 2.3. The plate on which the CI source is mounted contains a hole with an approximate diameter of 5 mm, through which the ion beam can exit the source chamber and enter the quadrupole ion bender in chamber 2 of Figure 2.3.

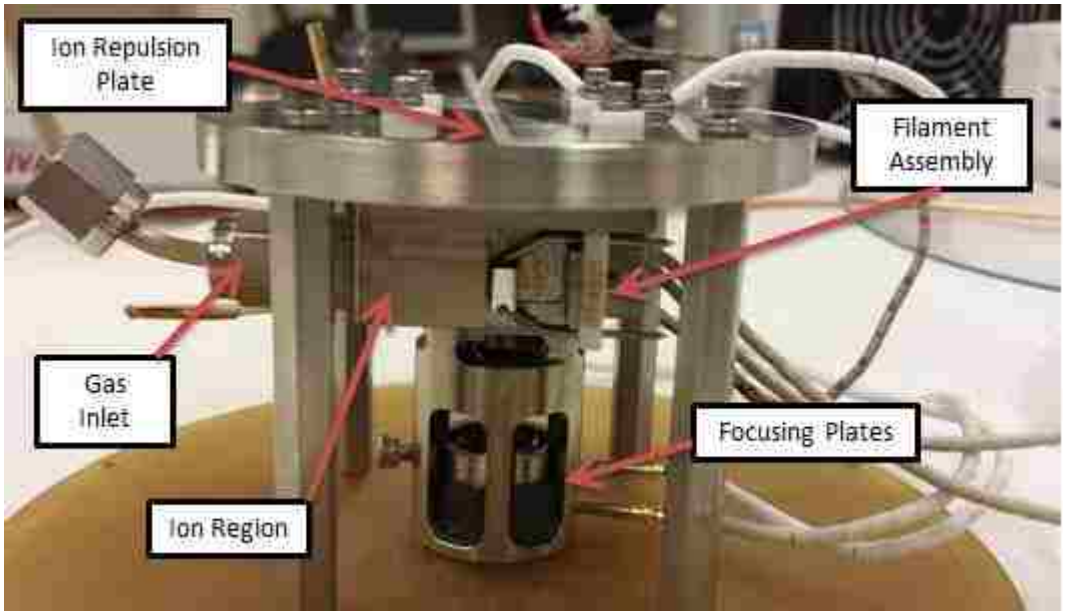


**Figure 2.7:** Picture of chemical ionization source mounted to differential pumping plate. The ion region contains a hollowed out space which is designed to operate at pressures up to 1 Torr, while maintaining significantly lower pressure outside of the source. The high pressure facilitates the formation of thermal electrons which can generate anions or undergo gas phase reactions to form cations impossible to generate in an electron impact ionization source.

As previously noted, CI sources can generate both positive and negative ions. To generate negative ions, a buffer gas doped with approximately 1% of the desired product molecule is flowed into the source. For example, if $SF_6^-$ was the desired product, a gas mix of 1% $SF_6$ and 99% argon would be introduced into the ionization source. For negative ion generation, target molecule must have a positive electron affinity so the

capture of an electron will be an energetically favorable process. This method precludes a number of potential gases of interest, including $CO_2$, from being used in negative ion chemical ionization. Similar to electron impact ionization, a hot filament is used to generate electrons to induce ionization events, and collisions with the buffer gas result in the generation of thermal electrons. The comparatively high pressure in the ionization region ensures a sufficient number of collisions can occur to generate the thermal electrons. Negative ions can be generated when an electron with sufficiently low energy, below the ionization energy of the target molecule, undergoes a collision with the target molecule. Negative ions are extracted from the ionization region upon formation by applying a positive voltage to ion-repulsion plate.

The mechanism for positive-ion generation in a chemical ionization source is different from electron impact ionization, because rather than ionization occurring directly from collisions with an electron, the ion is formed from a reaction with ions in a reagent gas. Field and coworkers developed the chemical ionization technique in 1966, and generally used methane as their reagent gas.[50] At low (sub $10^{-2}$ Torr) pressures in the ionization source, typical ionization products of methane, including $CH_4^+$, $CH_3^+$, $CH_2^+$, and $CH^+$, were observed in their resulting mass spectrum. Increasing the pressure inside the source above the $10^{-2}$ Torr threshold, to as high as 0.5 Torr, produced interesting changes in the mass spectrum. Products of neutral methane reacting with methane ions were observed, including $C_3H_5^+$, $C_2H_5^+$, and $CH_5^+$. Upon formation, these ions do not undergo further reaction with neutral methane, but additional types of ions can be created by doping the reagent gas with approximately 1% of a sample gas that will react further with those ions. Future experiments involving the chemical ionization source could

include the formation of negative counter ions, so positive metal ions which are generated in the magnetron sputter source could be deposited, or the source could be used in positive ion mode, and unstable cationic molecular ions could be stabilized in the matrix for spectroscopic study.

### 2.4 Matrix-Gas Mixing and Delivery

Matrix gases were created *via* dilution of stock gases using standard mixing procedures in a custom gas-mixing rack built by a previous student in the Moore group. An Edwards XDS 10 scroll pump was used to keep the gas rack and matrix delivery lines at a constant pressure on the order of 10s of millitorr while not in use to minimize the amount of atmospheric contaminants in the lines during gas mix generation and matrix gas delivery. A Pirani gauge (Kurt J. Lesker-6000) was used to measure the pressure in the gas rack from 0-1000 millitorr, as a monitor of the base pressure while the gas rack was not in use. A Kurt J Lesker Series 902 Piezo gauge is used to measure the pressure from 1-1000 Torr to measure the pressure of dopant gases while generating matrix gas mixtures, and a -0.1-0.6 Mpa Bourdon gauge (Swagelok EN-837-1) was used to measure the pressures during dopant gas dilution, and to monitor the pressure of the gas rack during matrix gas delivery. Aluminum mixing bottles were used to house matrix gas mixes, and most of the gas rack was made of ¼" copper line, as CO can react with the nickel and iron present in stainless steel, generating contaminants which could be observed during matrix experiments. Matrix gases were generated using standard gas dilution techniques, and dopant gas concentrations were typically on the order of 0.02% to 2% of the matrix gas mixture.

A number of high-pressure stock gases (Praxair or GTS Welco) were kept for use as matrix gases, dopants, or counter ion sources. Argon and krypton were used for either a matrix gas or counter-ion gases. A separate argon tank was kept for use as the sputter gas for the magnetron sputtering source, and ultrahigh purity He (99.9999%) was used to purge the cryostat during operation. Carbon dioxide (99.999%), CO (10.5% in He), $O_2$ (99.99% or 10% in Ar) were utilized as dopant gases. Sulfur hexafluoride, NO, and the CO in He mix were sometimes used as counter ion gases, and could be connected as needed to a manifold controlling counter ion gas delivery.

The flow of matrix gas was controlled by an Alicat Scientific MC Series mass flow controller with a gas delivery rate range of 1-10 sccm. A coil of copper line was placed in the matrix-delivery line between the flow controller and the output to the deposition chamber. The coil was submerged in a liquid nitrogen-ethanol bath with an approximate temperature of 157K during deposition to trap contaminants in the matrix gas mix including $CO_2$, water, and undesired metal carbonyls formed from reactions between CO and the gas lines. The bath was used in all experiments using CO-doped matrix gases, but was not in place while performing experiments with $CO_2$, as the sublimation point of $CO_2$ is approximately 195K, well above the temperature of the bath. Halfway through the deposition period, deposition was stopped and the bath was removed and remade. While the bath was remade, the matrix-gas-delivery line was closed to the deposition chamber, and the trap was pumped out to remove any contaminants that had been frozen in the trap, ensuring they were not deposited when deposition resumed.

## 2.5 Data Collection and Processing

A Thermo-Fisher Nicolet 6700 spectrometer with an external liquid nitrogen cooled MCT-A detector was used for collection of FTIR spectra during matrix experiments. Background spectra were collected periodically, rather than before each experiment, with the IR deposition window in the beam path. Because of temperature dependent impurities such as background water, the window was cold during collection of background spectra. The backgrounds collected for most spectra presented were collected with the window cooled to 10K. In Chapter 4, spectra collected at higher temperatures, ranging from 18K to 30K, are presented, and the background spectrum for these spectra was taken with the window cooled to 20K. The background spectrum is a 2500-scan-averaged, single beam spectrum collected for both 0.5 $cm^{-1}$ and 0.125 $cm^{-1}$ resolutions. Because background spectra were not collected before all experiments, atmospheric suppression, a built-in feature of the Omnic program used for data collection, was used to account for daily variations in atmospheric water levels.

Spectra were collected using Omnic, a Thermo Fisher Scientific software, and post-collection processing was carried out using the Origin 8.0 software suite. Baseline correction of the spectra was required due to a steep positive slope in the spectra, which likely arises from frequency-dependent scattering due to the polycrystallinity of the matrix. Baseline correction was performed by applying a $9^{th}$ order polynomial fit to the spectrum. A representative as-collected spectrum, the polynomial fit, and resulting baseline corrected spectrum are shown in Figure 2.8. The fitting procedure leveled the baseline without affecting the matrix peaks. Etaloning was another spectral feature which sometimes required correction. The etalon was a result of the IR beam reflecting from the

matrix and IR window, causing interference in the beam which generated a standing wave pattern in the spectrum. The etalon frequency depends on the thickness of the matrix, and a thicker matrix resulted in a higher frequency etalon with lower amplitude. This result was favorable to a low frequency, high amplitude etalon, so long deposition times of four to six hours were utilized to build up a sufficiently thick matrix. If necessary, the etalon could be removed using baseline subtraction by fitting either a sine wave to the data, or using Origin's polynomial fitting function on a truncated section of the data. In theory, the etalon frequency could be removed by masking it in the interferogram, but this was found to affect the appearance of other features in the spectrum.

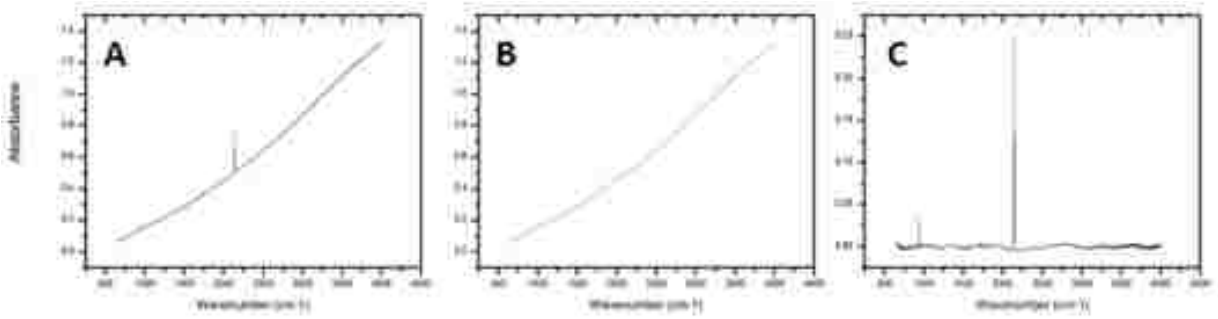


**Figure 2.8:** Appearance of an infrared spectra as collected (A), the 9$^{th}$ order polynomial fit applied by Origin (B), and the resulting baseline corrected spectrum (C).

## 2.6 Appendix

**Table 2.1 System Gauge and Vacuum Pump Overview**

| Chamber | Pressure Gauge | Primary Pump | Backing Pump |
|---|---|---|---|
| **Magnetron (Chamber 1)** | Balzers Compact Full Range | Osaka TG900/1300M | Adixen ACP28 Rotary Vane |
| **Quadrupole (CH 2)** | Kurt J. Lesker G100K Ion Gauge | Osaka TG900/1300M | Edwards XDS35i Scroll |
| **Bender (CH 3)** | KJL Ion Gauge | Edwards SCU 750 | Edwards XDS35i |
| **Deposition (CH 4)** | KJL Ion Gauge and Residual Gas Analyzer | Osaka TG390/420M | Edwards XDS35i |
| **Ion Source (CH 5)** | N/A | Osaka TC164 | Osaka DSP250 Rotary Vane |
| **Chemical Ionization** | Lesker KJL-6000 Pirani | Pfeiffer TMU 071P | Osaka DSP250 |

The system and turbo pumps were protected by pneumatic gate valves placed in the foreline between the turbo and backing pumps. The gate valves were held open by compressed air, so in the event of a power failure in the building, the compressed air would shut off and close the gate valves. This precaution would prevent air from rushing backwards through the backing pumps and into the UHV system. The turbo pumps in chambers 1 and 3 were water-cooled. A Neslab System II heat exchanger was used to cool those pumps. The other turbo pumps were air-cooled.

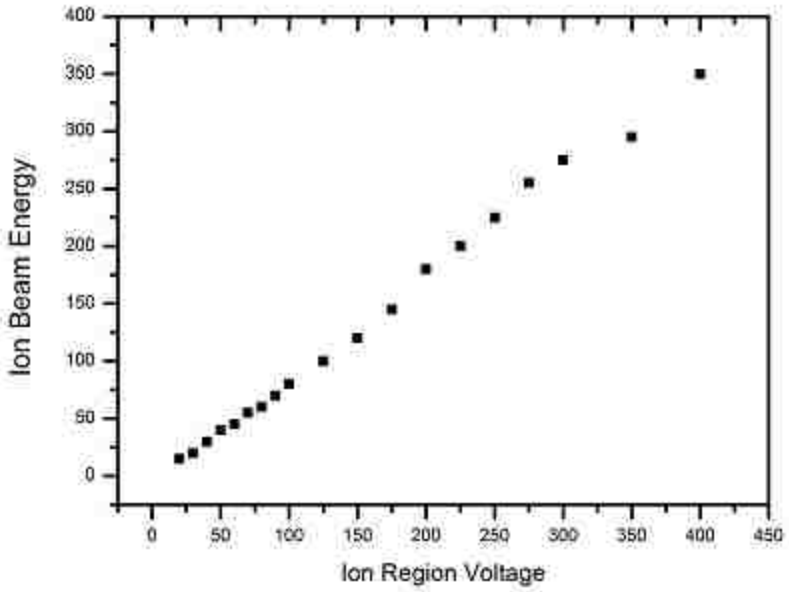


**Figure 2.9:** $Ar^+$ beam energy results from stopping potential experiments taken as a function of the voltage applied to the Jumbo EI source ion region.

**Table 2.2 Representative Ion Optics Settings for High Energy $Ar^+$ Deposition**

| **Optic** | **Bias (V unless noted)** |
|---:|:---:|
| Ion Entrance | 40 |
| Inner Pole | 195 |
| Outer Pole | -375 |
| Bender Exit Plate | 0 |
| Bender Top/Bottom | 50 |
| Octupole Entrance Lens | 0 |
| Octupole RF | 90 |
| Octupole DC Bias | 30 |
| Octupole Exit Lens | 0 |
| **EI Source** | |
| eV Command | -82 |
| em Command | 0.70 mA |
| Filament Limit | 7.00 A |
| Ion Region | 350 |
| Extractor | 20 |

**Table 2.3 Representative Ion Optics Settings for Generation 1 Deposition**

| Optic | Bias (V unless noted) |
|---|---|
| Nozzle | 240 |
| 22 mm Quad RF | 70 |
| 22 mm Quad DC Bias | 4 |
| 22 mm Exit Lens | 6 |
| 9 mm Entrance Lens | 250 |
| 9 mm Quad Prefilter | 12 |
| 9 mm Quad DC Bias | 10 |
| Bender Entrance Lens | 5 |
| Ion Entrance | -10 |
| Inner Pole | 56 |
| Outer Pole | -3 |
| Bender Exit Plate | 0 |
| Bender Top/Bottom | 48 |
| Octupole Entrance Lens | 0 |
| Octupole RF | 54 |
| Octupole DC Bias | 15 |
| Octupole Exit Lens | 25 |
| **EI Source** | |
| eV Command | -70 |
| em Command | 0.2 mA |
| Filament Limit | 7 A |
| Ion Region | 70 |

**Table 2.4 Representative Ion Optics Settings for New Simultaneous Mass Selection System***

| Optic | Bias (V unless noted) | Bias (V unless noted) | Bias (V unless noted) | Bias (V unless noted) |
|---|---|---|---|---|
| | $SF_5^+$ / $SF_3^+$ (Low E) | $SF_5^+$ (High E) | $Ar^{2+}$ | $Ar^+$ |
| **New Ion Optics** | | | | |
| Deflector Entrance Lens | 16 | 53 | 14 | 16 |
| Inner Poles (New Bender) | 25 | 70 | 27 | 26 |
| Outer Poles (New Bender) | -400 | -400 | -400 | -400 |
| Quad Entrance Lens | -20 | -10 | -24 | -20 |
| Prefilter | 10 | 53 | 10 | 12 |
| Quad Exit | 13 | 50 | 5 | 13 |
| Focus Lens | -9 | 0 | -17 | -9 |
| Jumbo Filament Shield | -80 | -280 | -70 | -80 |
| Jumbo Ion Region | -30 | -100 | -30 | -30 |
| Jumbo Extractor | -55 | -236 | -45 | -55 |
| **Shared Optics** | | | | |
| Ionizer Entrance | 4 | 6 | 5 | 4 |
| Inner Poles (Original Bender) | 18 | 53 | 18 | 18 |
| Outer Poles (Original Bender) | -12 | -5 | -13 | -10 |
| Bender Exit Plate | 3 | 0 | 4 | 0 |
| Bender Top/Bottom | -9 | 21 | -9 | 0 |
| Octupole Entrance Lens | 0 | 0 | 3 | 3 |
| Octupole RF | 54 | 54 | 54 | 54 |
| Octupole DC Bias | 12 | 15 | 9 | 14 |
| Octupole Exit Lens | 9 | 40 | 12 | 15 |
| **EI Source (new)** | | | | |
| eV Command | -70 | -61 | -100 | -70 |
| em Command | 3.4 mA | 3 mA | 3 mA | 3 mA |
| Filament Limit | 7 A | 7 A | 7 A | 7 A |
| Ion Region | 23 | 64 | 23 | 23 |
| Extractor | -14 | -6 | -12 | -12 |

***Metal anion specific optics (Nozzle – Bender entrance) consistent with Table 2.3

**Emission Spectra of Photolysis Sources**

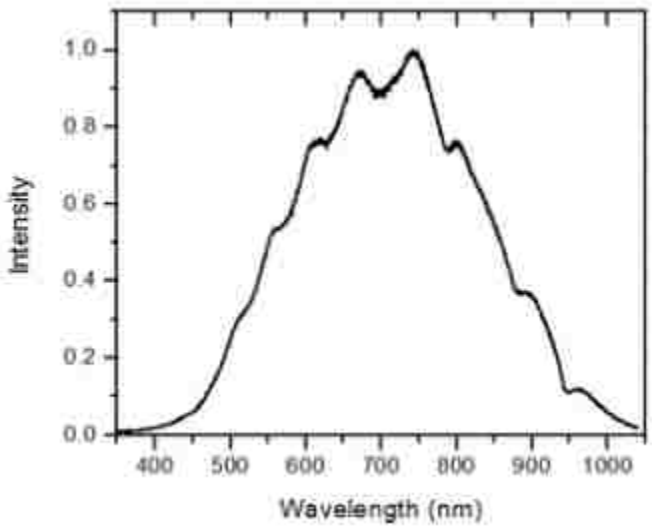


**Figure 2.10:** Emission spectrum of broadband tungsten filament-bulb, used for broadband photolysis studies of $CO_2$ containing matrices presented in Chapter 3. Spectrum was collected and figure generated by Ryan Ludwig.[41]

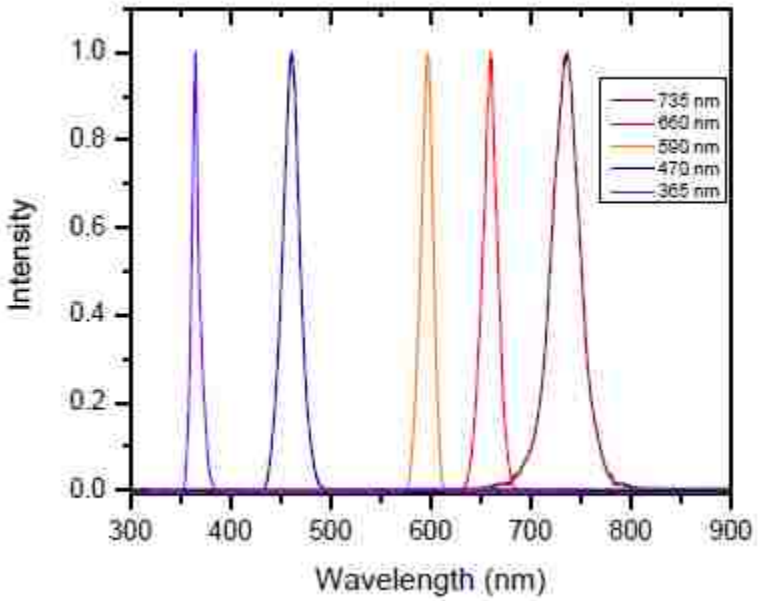


**Figure 2.11:** Emission spectrum of narrow band LED sources used for wavelength dependent photolysis studies which will be presented throughout this dissertation. Spectra were collected and figure was created by Ryan Ludwig.[43]

# Chapter 3

## Characterization of Ionic $CO_2$ Complexes

## Using the Counter Ion Co-Deposition Technique

### 3.1 Abstract

An anionic copper carbon dioxide complex, $CuCO_2^-$, and other ionic $CO_2$ complexes were observed and characterized in cryogenic $CO_2$ doped matrices using the counter ion co-deposition technique. Several species that have been previously identified in argon and neon matrices were observed in krypton and nitrogen for the first time. The formation of these species and their behavior following annealing and irradiation steps were dependent on initial deposition conditions, including counter ion identity and energy. Deposition of high energy $Ar^+$ yielded both anionic and cationic $CO_2$ complexes upon deposition, though such species are only observed after photolysis of the matrix following co-deposition of low energy $Ar^+$ and $Cu^-$. In addition, deposition of $SF_6$ cation derivatives with $Cu^-$ shut down the formation of these ionic $CO_2$ complexes. The dependence on concentration and deposition-temperature are also discussed, including an apparent increased complexity of ionic $CO_2$ complexes in matrices deposited at high temperature.

### 3.2 Introduction

An original research goal of the Moore group was to use matrix-isolation spectroscopy as a means to study the catalytic mechanism of CO-oxidation on metals. Experiments involving the deposition of $Cu^-$ into matrices containing $CO_2$ were performed to characterize potential products of the catalytic reaction. In addition to the observation of a copper carbon dioxide anion complex, other interesting discoveries

involving the behavior of ionic $CO_2$ species were made. In this chapter, results of experiments involving $CO_2$-doped matrices under varying experimental conditions are discussed. A number of experimental studies have been reported on the structure and behavior of neutral $CO_2$ monomers and dimers in cryogenic matrices.[51-56] Andrews and Jacox have identified a variety of ionic $CO_2$ complexes in both argon and neon matrices.[57-61] Andrews identified a number of cationic[62, 63] and anionic[64] metal $CO_2$ complexes, including the $CuCO_2^-$ complex, though we discovered his assignment of one of the bands is incorrect, as will be discussed later in this chapter.

We have identified several ionic $CO_2$ species in krypton and nitrogen matrices for the first time, and have also identified a number of new bands attributed to ionic $CO_2$ species that are only observed following high temperature deposition of an argon matrix. Due to the increased control over ion delivery provided by the counter ion co-deposition method, we were able to observe interesting trends and behaviors of the ionic $CO_2$ species that are dependent on counter ion choice and deposition energy. Also, we identified and characterized a previously unknown thermodynamic equilibrium of two conformations of anionic $CO_2$ dimers, which are mentioned here but discussed at length in the next chapter. Neutral $CO_2$ species exhibited behavior consistent with previously reported results.

**3.3 Experimental Methods**

Experiments were performed using argon, krypton, and nitrogen matrices which were doped with 0.02% to 0.5% $CO_2$. Deposition was carried out at 10K or 20K at a rate of 3-10 SCCM, corresponding to a pressure on the order of $10^{-5}$ Torr in the deposition chamber. Deposition times ranged from two to six hours, and all experiments were

carried out under darkened conditions. A beam of mass-selected $Cu^-$ was co-deposited with a cationic counter ion beam, either $Ar^+$ or a mixture of cations from a parent $SF_6$ molecule. Most experiments were performed before the deposition system was upgraded to allow mass resolution of the counter ion beam, so no specific counter ion could be selected when using $SF_6$ as the counter ion gas. For brevity, throughout this chapter $SF_5^+$ will be referred to as the counter cation deposited when using $SF_6$ as the counter ion gas, though in actuality there was a mixture of $SF_x^+$ ($x \leq 5$) deposited, with $SF_5^+$ being the major product formed upon ionization. This was confirmed by mass spectroscopy data taken following the installation of the second mass resolving quadrupole. Additionally, a significant amount of neutral $SF_6$ was deposited in the matrix during these experiments due to the proximity of the deposition chamber to where the counter ion gas was introduced. In some experiments presented in this chapter, the counter ion co-deposition technique was not used, and instead high energy $Ar^+$ (300+ eV) was used as the sole ion source. Following deposition, the matrix was subjected to a series of processing steps including irradiation with visible light sources and annealing at as high as 30K. A spectrum was collected following each processing step.

## 3.4 Results and Discussion

### 3.4.1 Characterization of $CuCO_2^-$

Peaks assigned to the anionic copper carbon dioxide complex $CuCO_2^-$ were observed following deposition of a 0.5% $CO_2$ doped argon matrix co-deposited with $Cu^-$ and both $Ar^+$ or $SF_5^+$. The three peaks were still observed following deposition of a 0.1% $CO_2$ doped matrix, though with diminished intensity, and the peaks were not observed when the concentration of $CO_2$ in the matrix is reduced to 0.02%. Under identical

experimental conditions, deposition of $Cu^-/SF_5^+$ resulted in an approximately 50% reduction in $CuCO_2^-$ peak intensity as compared to deposition of $Cu^-/Ar^+$. The three peaks which are assigned to $CuCO_2^-$ are shown in Figure 3.1.

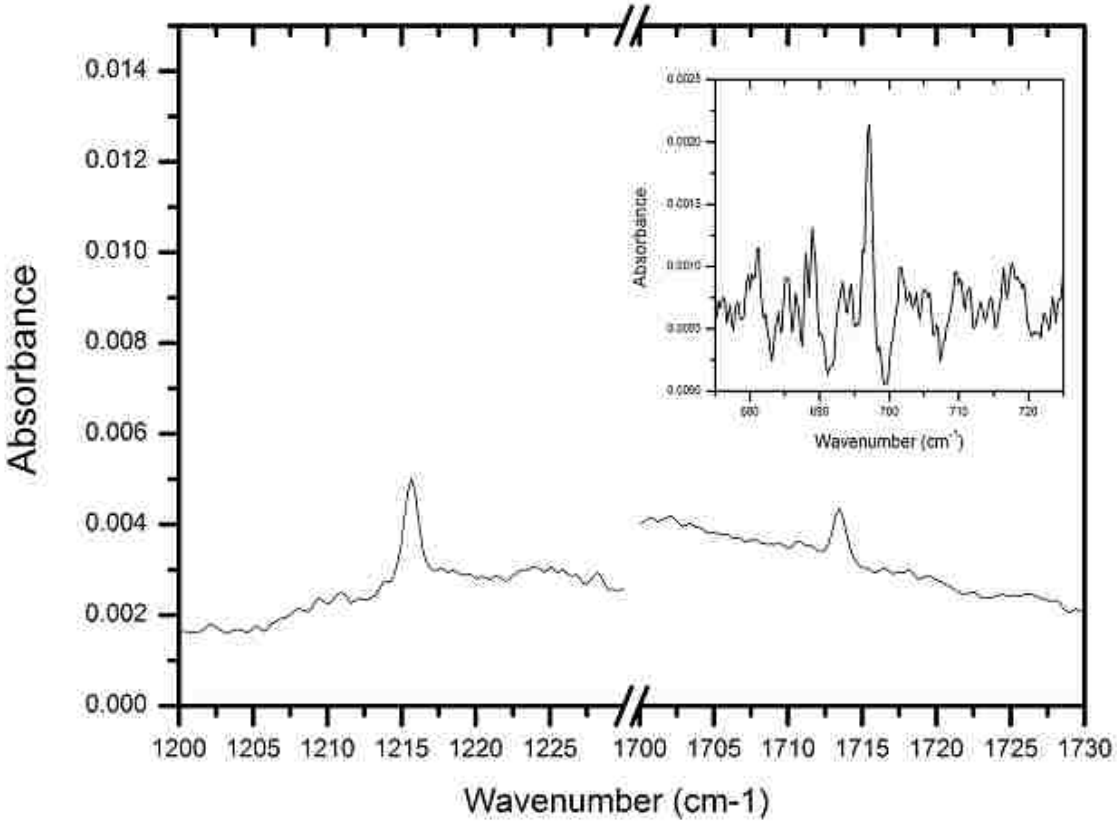


**Figure 3.1:** Infrared spectrum collected following deposition showing three peaks assigned to $CuCO_2^-$ located at 1215.6 $cm^{-1}$ (left of break), 1713.5 $cm^{-1}$ (right of break), and 697.1 $cm^{-1}$ (inset), which occur in a 0.5% $CO_2$ doped argon matrix deposited at 10K with $Cu^-$ and $Ar^+$.

Andrews previously assigned three peaks to $CuCO_2^-$ in an argon matrix using his laser ablation matrix isolation technique.[64] Three peaks were identified at 1713.4 $cm^{-1}$, 1234.2 $cm^{-1}$, and 697.0 $cm^{-1}$, and were assigned to the antisymmetric stretch, symmetric stretch, and bending modes of $CO_2$ in the $CuCO_2^-$ complex. Based upon our experiments, we agree with the assignment of the peaks located at 1713.5 and 697.1 $cm^{-1}$, but we

observed the peak corresponding to the symmetric stretch at 1215.6 $cm^{-1}$. We are confident in this assignment, as the peak was only observed in conjunction with the peaks assigned to the other two modes, and it tracked in intensity with the other two. Additionally, no peak is observed in proximity to 1230 $cm^{-1}$. In his copper $CO_2$ experiments, Andrews also observed a peak at 1943.4 $cm^{-1}$, which he assigned to the CO stretching mode of $OcuCO^-$. He noted that the insertion products were formed by reaction with highly energetic laser ablated atoms. We did not observe a peak in this region of the spectrum, as the energy required to form such products may not be available in our lower-energy deposition system.

### 3.4.2 Counter Ion Effects on Formation of $CO_2^-$ and $(CO_2)(CO_2^-)$

The formation of non-metal containing ionic $CO_2$ species was dependent on the choice of matrix gas, deposition temperature, and the conditions under which ions are deposited in the matrix. As shown in Figure 3.2, upon co-deposition of $Cu^-$ and $Ar^+$ with a 0.5% $CO_2$ in Ar matrix deposited at 10K, the only anionic signal in the matrix was due to $CuCO_2^-$, with the peak at 1713.5 $cm^{-1}$ assigned to the antisymmetric stretch appearing in the displayed region of the spectrum. Upon annealing the matrix with a broadband visible light source (spectrum provided in Experimental Methods Chapter, Figure 2.10), two peaks appeared at 1652.7 $cm^{-1}$ and 1657.0 $cm^{-1}$. These were assigned by Andrews to $(CO_2^-)(CO_2)_x$ and $CO_2^-$, respectively.[59] As is discussed later, we reassign the peak at 1652.7 $cm^{-1}$ from $(CO_2^-)(CO_2)_x$ to the dimeric species $(CO_2)(CO_2^-)$.

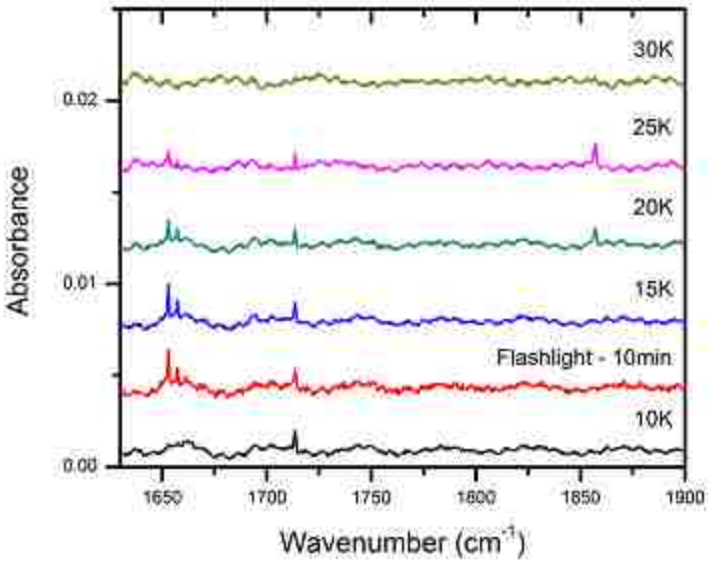


**Figure 3.2:** Spectral region showing peaks assigned to antisymmetric stretching modes of various anionic $CO_2$ containing species following deposition of 0.5% $CO_2$ in argon matrix with $Cu^-$ co-deposited with $Ar^+$. The temperature refers to the temperature the matrix was annealed to before collecting each spectrum at 10K.

Following annealing to 15K, species present in the matrix underwent no changes in this spectral region of 1625 $cm^{-1}$ to 1900 $cm^{-1}$. Annealing at 20K and 25K produced new peaks at 1856.9 $cm^{-1}$ and 1185.3 $cm^{-1}$, which were assigned by Andrews to the antisymmetric and symmetric stretching modes of $C_2O_4^-$, respectively.[59] There is also a reduction in the size of the peaks at 1652.7 $cm^{-1}$ and 1657.0 $cm^{-1}$. As will be discussed in detail Chapter 4, $C_2O_4^-$ actually exists in thermodynamic equilibrium with $(CO_2)(CO_2^-)$. Upon annealing to 30K, all the anionic peaks in this region were lost, including the $CuCO_2^-$ peak.

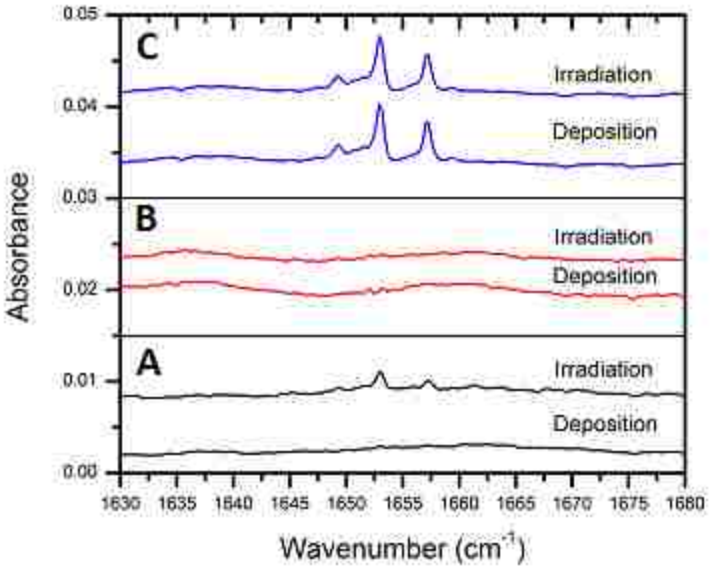


**Figure 3.3:** Infrared spectra comparing the behavior of $CO_2$ anions as a function of ion deposition conditions immediately following deposition, and then following broadband irradiation of the matrix performed directly after the collection of the deposition spectrum. Each spectrum shows a 0.5% $CO_2$-doped argon matrix at 10K under otherwise identical experimental conditions except for different counter ion deposition method. The counter ion conditions are: (A) $Cu^-/Ar^+$; (B) $Cu^-/SF_5^+$ cations; (C) high energy $Ar^+$ only.

Significant differences are observed in the behavior of the ionic $CO_2$ clusters depending upon the conditions under which ions were deposited in the matrix. The effects of counter ion deposition conditions on anionic $CO_2$ species are shown in Figure 3.3. The only anion formed upon co-deposition of $Cu^-$ and low-energy $Ar^+$ was $CuCO_2^-$. As shown in Figure 3.3 A, other anionic $CO_2$ clusters only formed following irradiation. When $Ar^+$ was replaced with $SF_5^+$, as shown in Figure 3.3 B, only metal containing anionic $CO_2$ complexes were observed upon deposition, and no additional species appeared following irradiation. When high energy $Ar^+$ was the used as the counter ion (Fig. 3.3 C), anionic $CO_2$ complexes were observed immediately upon deposition, and no changes to the species were observed after irradiation.

The formation of anionic $CO_2$ clusters upon irradiation of the matrix in the $Cu^-/Ar^+$ system means that irradiation of the matrix must have resulted in a photodetachment event, releasing electrons into the matrix. The source of electrons is likely isolated $Cu^-$ which did not complex with $CO_2$ upon deposition, because the intensity of the $CuCO_2^-$ bands were not diminished upon irradiation. While linear $CO_2$, as it occurs in the gas phase, has a negative electron affinity, bent $CO_2$ can form a stable anion.[65] Free electrons released from anionic centers in the matrix upon irradiation could migrate to and be captured $CO_2$ species, resulting in the appearance of the anionic $CO_2$ complexes. In the $Cu^-/SF_5^+$ system, anionic $CO_2$ complexes did not form following irradiation of the matrix. Due to high background pressuring in the ionization source, neutral $SF_6$ is deposited during matrix deposition. Sulfur hexafluoride has a more positive electron affinity than bent $CO_2$,[65, 66] so upon irradiation, it is more energetically favorable for photodetached electrons to attach to an $SF_6$ molecule. Although this is the simplest explanation for why anionic $CO_2$ complexes are not observed, the peak that has been assigned to $SF_6^-$ appears outside the detection range of our instrument, so we cannot confirm its formation.

Deposition of high energy $Ar^+$ without a counter ion results in the observation of anionic $CO_2$ complexes immediately upon deposition. The intensity of the peaks assigned to these species increased significantly compared to the intensity observed following irradiation of the $Cu^-/Ar^+$ system. Maier suggested when he introduced his method of high energy deposition of molecular ions,[32] and confirmed in a later experiment by the Leroi group,[33] that this source of electrons was grounded metal surrounding the matrix window. The beam of cations apparently strikes the metal, be it the sample holder or

radiation shield, with enough energy to eject electrons, which can then be captured by $CO_2$. They suggested in these studies that the anionic species form prior to deposition and are then trapped in the growing matrix. In our studies, the ions appear to be formed directly in the matrix, rather than externally, as anionic $CO_2$ complexes only form in the matrix following irradiation in the $Cu^-/Ar^+$ system. Furthermore, the ionic species observed upon deposition exhibit a temperature dependence which is difficult to rationalize if the electron attachment was occurring external to the matrix.

### 3.4.3 Counter Ion Effects on Formation of Cationic $CO_2$ Species

As with the $CO_2$ anions, the manner in which ions are delivered to the matrix also affects the formation of cationic $CO_2$ species. Figure 3.4 contains spectra collected following deposition of a 0.5% $CO_2$-doped argon matrix using the three previously discussed methods for ion delivery, highlighting the region of the spectrum containing peaks assigned to cationic $CO_2$ species. Cationic $CO_2$ clusters are observed in the $Cu^-/Ar^+$ and high-energy $Ar^+$ spectra, but not in the spectrum containing $SF_6$. Three ionic peaks are observed, including a large peak at 1274.0 $cm^{-1}$, and two smaller peaks at 1270.1 $cm^{-1}$ and 1272.2 $cm^{-1}$. Andrews assigned the 1274.0 $cm^{-1}$ to the dimeric cation $(CO_2)_2^+$,[59] but the other two peaks have not been observed previously. We assign the peaks at 1270.1 $cm^{-1}$ and 1272.2 $cm^{-1}$ to other $CO_2$ cluster cations due to their proximity to the dimeric cation, noting also that, unlike the anionic compounds, they are present immediately upon deposition of the $Cu^-/Ar^+$ system. We have not performed the necessary isotopic substitution experiments and theoretical calculations to make a more definitive assignment of the structure of the cations giving rise to the two new pekas. The cation peaks are not affected by broadband irradiation, and do not change following

annealing of the matrix as high as 30K. The peak at 1279.3 $cm^{-1}$ has been assigned to the symmetric stretching mode of a neutral $CO_2$ dimer.[52]

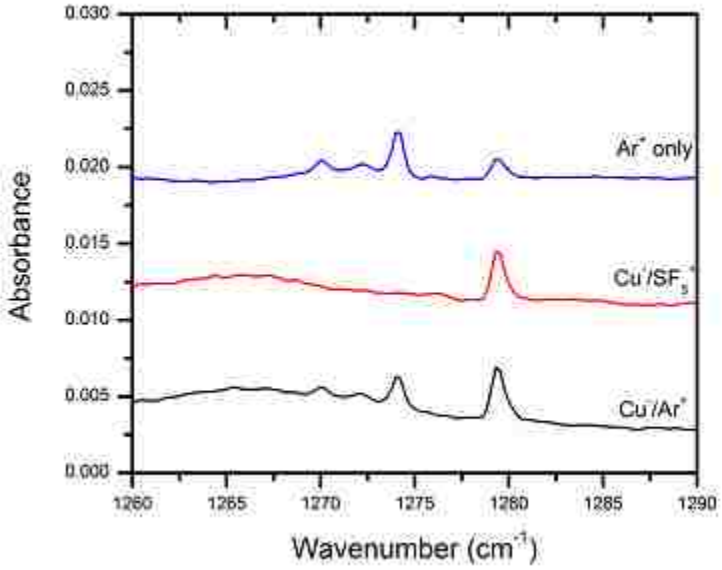


**Figure 3.4:** Region of the infrared spectrum showing peaks containing cationic $CO_2$ species. Three spectra highlight effects of counter-ion choice on species present following deposition in a 0.5% $CO_2$ doped argon matrix at 10K. The peak at 1279.3 $cm^{-1}$ has been assigned to a neutral $CO_2$ dimer.

The appearance of the $CO_2$ cations upon deposition only when $Ar^+$ is the counter ion can be explained based on the ionization energies of the ions. The ionization potential of gaseous argon is 15.75 eV,[67] and that of solid argon and $CO_2$ are nearly identical, 13.8 eV[68] and 13.78 eV,[69] respectively. Therefore, upon deposition, it is energetically favorable for the $Ar^+$ counter ion to transfer its charge to the matrix. This also means the charge can be transferred from the matrix to $CO_2$ monomers and clusters to generate cationic $CO_2$ clusters during deposition. On the other hand, $SF_6$ and its smaller molecular fragments have ionization potentials less than 10 eV,[70] so the charge likely remains localized on the externally generated cations. The charge-transfer pathway is thus eliminated, so $CO_2$ complexes are not observed.

### 3.4.4 High-Temperature Deposition

In addition to the 10K experiments, a high-energy $Ar^+$ deposition experiment was performed at 20K under otherwise identical deposition conditions to the 10K depositions. The resulting 20K deposition spectrum not only contained an increased intensity of ionic $CO_2$ peaks compared to 10K deposition, but the spectrum was also more complex. A number of previously unreported bands appeared in the region of the spectrum near the previously assigned anionic $CO_2$ clusters.

Figure 3.5 (A) shows a spectrum collected at 20K following the high temperature deposition of a 0.5% $CO_2$ doped argon matrix with high energy $Ar^+$. Following deposition at 10K, only three peaks are observed in the 1640 $cm^{-1}$-to-1660 $cm^{-1}$ region of the spectrum, and following annealing to 20K, the peak at 1652.7 $cm^{-1}$ converted to a peak at 1856.9 $cm^{-1}$. This region of the spectrum is much more complex following 20K deposition compared to 10K deposition. An additional four peaks were observed in the cluster of peaks near 1650 $cm^{-1}$. In addition, four clear new peaks and an additional two shoulder bands that are not baseline resolved, were observed in higher wavenumber spectral region from 1850 $cm^{-1}$-to-1875 $cm^{-1}$. With the exception of the small peak located at 1645.2 $cm^{-1}$, all peaks shown in Figure 3.5 have temperature-dependent intensities. All peaks are believed to be ionic as they are all irreversibly depleted completely or nearly completely following irradiation with a 365 nm narrow band UV diode (Fig 3.5 C). The only change to the cationic peaks following 20K deposition compared to 10K deposition is increased intensity.

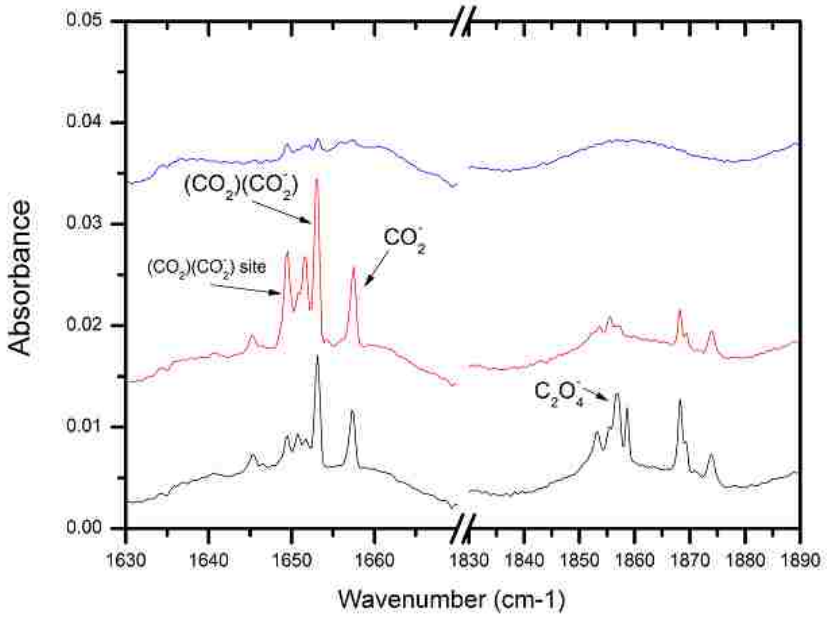


**Figure 3.5:** Infrared spectra showing increased number of peaks corresponding to anionic $CO_2$ compounds following deposition of a 0.5% $CO_2$ doped matrix at 20K with high energy $Ar^+$. For reference, the four peaks observed in the analogous 10K experiment are labeled. (A) spectrum collected following deposition at 20K. (B) spectrum collected at 10K after 25 minutes of equilibration. (C) spectrum taken at 10K following five minutes of irradiation with 365 nm narrow band UV diode (emission spectra provided in Chapter 2 Figure 2.11).

The temperature-dependence of the previously identified $(CO_2)(CO_2^-)$, $CO_2^-$, and $C_2O_4^-$ species are discussed in detail in Chapter 4. Briefly, the intensities of the $(CO_2)(CO_2^-)$ and $CO_2^-$ peaks remain constant from 10K up to 19K, and they lose intensity between 19K 23K, at which point the $(CO_2)(CO_2^-)$ peak is no longer visible. The $C_2O_4^-$ peak increases in intensity over this same range. The previously unreported peaks which appeared following deposition at 20K show distinctly different temperature dependent trends occurring over the range of 13K to 20K. The 10K spectrum (Fig 3.5 B) was collected 25 minutes after cooling from 20K. Additional experiments that cooled the matrix from 20K to 10K over the period of several hours showed all peaks in the 1850 $cm^{-1}$ to 1875 $cm^{-1}$ spectral region lost intensity, until only two small peaks remained

at 1855.4 $cm^{-1}$ and 1873.9 $cm^{-1}$. The slow-cooling experiment revealed that the previously identified $(CO_2)(CO_2^-)$ site peak appeared to convert with temperature to the new peak observed at 1868.2 $cm^{-1}$. New peaks are also observed in the vicinity of the peak assigned to the symmetric stretching mode of $C_2O_4^-$, and show the same temperature dependence as the new peaks in the antisymmetric stretching region. Further work to characterize this conversion needs to be performed, as well as determining if other high temperature peaks can be directly correlated with new peaks increasing at low temperatures.

### 3.4.5 Ionic $CO_2$ Species in Krypton and Nitrogen Matrices

Experiments were performed on 0.5% $CO_2$-doped nitrogen and krypton matrices to attempt to identify ionic $CO_2$ species in these matrix materials. Experiments presented in this section were performed using high energy deposition of $Ar^+$. In a nitrogen matrix deposited at 10K, a single sharp peak was observed at 1652.4 $cm^{-1}$ in the region where $CO_2$ anions are observed in argon and neon matrices. No peaks were observed in the region where cationic $CO_2$ clusters are observed, and no peaks in the region of 1850 $cm^{-1}$-to-1875 $cm^{-1}$ grew upon annealing. The intensity of peak at 1652.4 $cm^{-1}$ decreased with increased temperature, but no new peaks grew in conjunction with the loss of intensity of the band. The intensity was recovered reversibly upon cooling the matrix. This is similar to the behavior of the $CO_2^-$ peak in argon which appears at 1657.0 $cm^{-1}$. Previous studies have been hesitant to assign peaks to neutral $CO_2$ dimers in nitrogen.[52] If the nitrogen matrix limits the formation of $CO_2$ dimers, it is likely that the peak at 1652.4 $cm^{-1}$ is $CO_2^-$, though isotopic studies would need to be performed to confirm the assignment.

I did not observe peaks that could be assigned to cationic $CO_2$ compounds in either nitrogen or krypton matrices. Solid krypton has an ionization potential of 11.6 eV,[68] which is approximately 2 eV lower than $CO_2$. As a result it is energetically favorable for the argon cations to transfer their charge to the matrix rather than localize on $CO_2$. It is currently unclear why $CO_2$ cations are not observed in nitrogen, as the ionization potential of solid nitrogen[71] would favor charge transfer to $CO_2$. One possible explanation is that $CO_2$ dimers must form before accepting a positive charge. The only definitive matrix isolated $CO_2$ cation assignments in the literature are dimers, and previous studies in nitrogen matrices seem to show that the nitrogen matrix limits the formation of $CO_2$ dimers.[56, 72]

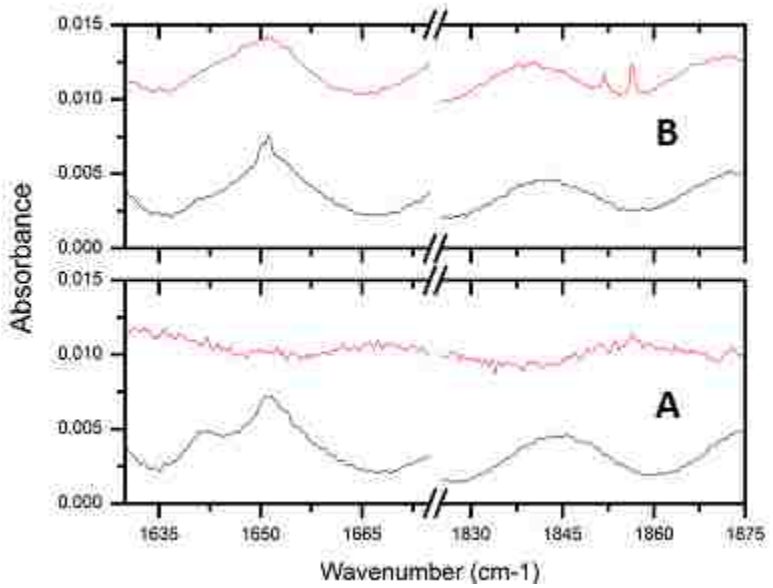


**Figure 3.6:** Anionic $CO_2$-cluster region of the infrared spectrum comparing deposition temperature of $CO_2$ doped krypton matrix experiments. (A) 10K deposition and (B) 20K deposition. The bottom black spectra in A and B were taken at the deposition temperature (10K/20K) and the top red spectra were taken at 35K and 32K in A and B, respectively.

Deposition of a 0.5% $CO_2$ doped krypton matrix at 10K with 300 eV $Ar^+$ yielded no clear ionic $CO_2$ clusters. The spectrum contained only a broad feature at 1650 $cm^{-1}$

which disappeared irreversibly upon annealing (Fig. 4.6A). Diffusion of $CO_2$ at 10K appears to be quenched more quickly in krypton than argon, minimizing the clustering required for anionic complex formation. This result is expected because krypton has a higher melting point than argon. However, deposition of a 0.5% $CO_2$-doped krypton matrix at 20K produces a peak at 1651.2 $cm^{-1}$, which we assign to the $(CO_2)(CO_2^-)$ species observed at 1652.7 $cm^{-1}$ in argon. The peak in krypton exhibits similar temperature-dependent behavior as is observed in argon, reversibly converting to a doublet of peaks at 1851.8 $cm^{-1}$ and 1856.4 $cm^{-1}$ at higher temperature. However, unlike argon, the high temperature species appears as a doublet. Results presented in the next chapter appear to confirm that the two peaks arise from the same species, which we assign as $C_2O_4^-$.

There are interesting differences in the appearance of the anionic peaks between argon and krypton. In argon, four distinct peaks are present in the 1650 $cm^{-1}$-to-1660 $cm^{-1}$ region, with three assigned to different structures of separated dimeric $CO_2$ anions, $(CO_2)(CO_2^-)$, and one assigned to $CO_2^-$. In krypton, only a single peak is observed in this region. In argon, a single peak at 1856.9 $cm^{-1}$ is assigned to $C_2O_4^-$, but in krypton a doublet is observed in this region. It appears that $C_2O_4^-$ can be trapped in one of two distinct matrix environments in krypton, but only one in argon. Computational work performed by Fleischman and Jordan found the lowest energy structure of oxalate-like $C_2O_4^-$ to have $D_{2d}$ symmetry, but a structure with $D_{2h}$ symmetry was found to only be slightly more energetic.[73] Tt is possible that in krypton, slightly different matrix cages can result in the stabilization of both of these structures. Likewise, the $(CO_2)(CO_2^-)$ dimer

appears to be trapped in a single matrix environment in krypton, but multiple in argon. This interpretation may explain the lack of a $CO_2^-$ peak in krypton.

### 3.5 Conclusions

The control provided over the energy and identity of deposited ions using the counter ion co-deposition technique provides new information about the formation mechanism of ionic $CO_2$ containing complexes in matrix-isolation experiments. Properties of deposited ions and of the matrix itself have an effect on the observed species. High-temperature deposition resulted in additional peaks in the spectra of anionic $CO_2$ complexes, and a number of species have correlated temperature-dependent behavior.

### 3.6 Appendix

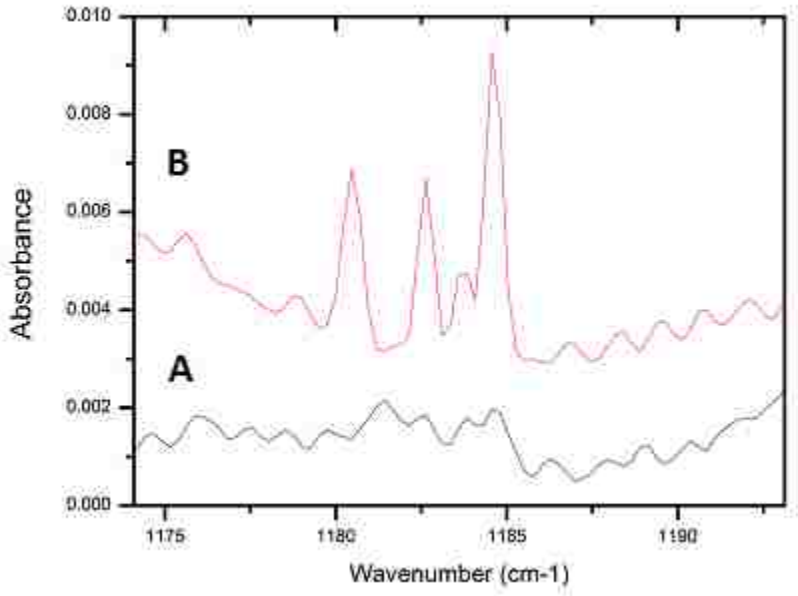


**Figure 3.7:** Infrared spectra showing symmetric stretching modes of $C_2O_4^-$ following deposition at (A) 10K and (B) 20K. Both spectra were collected at 23K. As can be clearly noted, 20K deposition produces new peaks and also results in significantly increased intensity of the previously assigned bands. The peaks in this region exhibit the same temperature-dependent behavior as the antisymmetric stretching modes of the dimeric $CO_2$ anions.

**Table 3.1 Vibrational Band Assignments for Matrix Isolated Ionic $CO_2$ – Containing Compounds**

| Species | Matrix Material | | |
|---|---|---|---|
| | Argon ($cm^{-1}$) | Krypton ($cm^{-1}$) | Nitrogen ($cm^{-1}$) |
| **$CuCO_2^-$** | 1713.5[a] | | |
| | 1215.6 | | |
| | 697.1[a] | | |
| **$C_2O_4^-$*** | 1856.8[b] | 1856.4 | |
| | | 1851.8 | |
| | 1184.6[b] | 1180.7 | |
| **$C_2O_4^-$ site peaks*** | 1873.9 | | |
| | 1869.4 | | |
| | 1868.2 | | |
| | 1858.6 | | |
| | 1855.4 | | |
| | 1853.2 | | |
| | 1183.8 | | |
| | 1182.6 | | |
| | 1180.4 | | |
| **$CO_2^-$** | 1657.5[b] | | 1652.4 |
| **$(CO_2)(CO_2)^-$** | 1653.1[b] | 1651.2 | |
| **$(CO_2)(CO_2^-)$ site peaks** | 1651.7 | 1650.3 (?) | |
| | 1650.7 | | |
| | 1649.5[b] | | |
| | 1645.5 | | |
| **$(CO_2)_2^+$** | 1274.2[b] | | |
| **$(CO_2)_2^+$ site peaks** | 1271.1 | | |
| | 1270.1 | | |

[a] Denotes assignment from reference 59

[b] Denotes assignment from reference 54

* Indicates peak only visible following annealing or high temperature deposition

# Chapter 4

## Identification of a Low Temperature Thermodynamic Equilibrium Involving Isomers of $CO_2$ Dimer Anions in Cryogenic Argon and Krypton Matrices

### 4.1 Abstract

A thermodynamic equilibrium of two dimeric $CO_2$ anions was characterized in cryogenic matrices. Reversible conversion between $(CO_2)(CO_2^-)$ and $C_2O_4^-$ has been observed spectroscopically over the temperature ranges 19-23K and 26-31K in argon and krypton, respectively. A van't Hoff analysis showed that the reaction is endothermic and is driven by a large increase in entropy. Interestingly, the reaction has approximately the same large, positive standard entropy change of ~170 J $mol^{-1}$ $K^{-1}$ in both media, meaning the enthalpy change is proportionally larger in krypton, to match the higher temperature range over which the equilibrium is observed. The entropic driving force must be due to interactions between the ionic complexes and matrix, but the exact nature has yet to be determined. A kinetic analysis of the reaction in argon was also performed to determine temperature-dependent rate constants for the reaction. The reaction path was modeled as a single barrier process using the Eyring. Standard enthalpy ($\Delta H^{\ddagger}$) and entropy ($\Delta S^{\ddagger}$) changes for the forward and reverse reactions relative to the transition state were determined based on the temperature-dependent rate constants. These results show that the endothermic enthalpic surface is barrierless. On the other hand, the transition state is ~80 J $mol^{-1}$ $K^{-1}$ below the reactants, and ~250 J $mol^{-1}$ $K^{-1}$ below the products These values are in good agreement with the ~170 J $mol^{-1}$ $K^{-1}$ change found using the van't Hoff analysis of the reaction. The agreement of the two methods increases the confidence

in the results, as the values from the van't Hoff and kinetic analysis are determined independently of one another.

## 4.2 Introduction

Carbon dioxide cluster anions, $(CO_2)_n^-$, have been the subject of a number of computational[65, 73-78] and experimental studies.[57-60, 79-86] Of particular interest has been how the excess charge is delocalized through the cluster. Early computational studies performed by Fleischman and Jordan[73] found three potential structures for the dimeric anion. They proposed two isomers of $C_2O_4^-$, with $D_{2d}$ or $D_{2h}$ symmetry, and a third ion-solvent structure of $CO_2 \cdot CO_2^-$ with $C_s$ symmetry. Further computational studies performed by Saeki and coworkers reexamined the dimer anion structures.[75] Use of a larger basis set and considering the effects of electron correlation found that the $C_s$ form had a slightly different geometry, with $C_{2v}$ symmetry. Coupled cluster calculations on the system performed by Sommerfeld and Posset confirmed the $C_{2v}$ and $D_{2d}$ structures to be the lowest energy of the dimers.[77] These structures are shown in Figure 4.1.

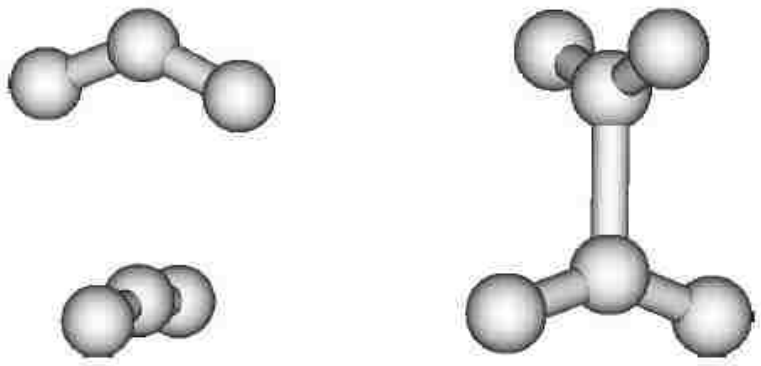

**Figure 4.1:**[77] Geometric structures of dimeric $CO_2$ anions. $C_{2v}$ structure of $(CO_2)(CO_2^-)$ and $D_{2d}$ structure of $C_2O_4^-$. Figure adapted from reference 77.

Experimental studies using photoelectron spectroscopy performed by Nagata and coworkers, and vibrational spectroscopy performed by Johnson, Weber, and coworkers,[80] revealed that the charge distribution is dependent upon the size of the cluster.[79] Cluster anions $(CO_2)_n^-$ where $2 \leq n \leq 5$ contain a core dimeric anion, $C_2O_4^-$. Monomeric cores, $CO_2^-$, are found in clusters where $7 \leq n \leq 13$, and dimeric cores are again found in clusters where $14 \leq n \leq 15$. Both anions were observed in clusters where $n = 6$. A computational study was performed by Nagata and coworkers to understand the isomerization of the dimer anion between $C_2O_4^-$ and $CO_2 \cdot CO_2^-$.[75] They found that motion of the solvating neutral $CO_2$ about $CO_2^-$ was correlated with a change in the electronic structure of the dimer which drove the charge to be contained on a single $CO_2$ molecule or delocalized across both molecules in the dimer.[75] Multiple computational studies have found the $D_{2d}$ structure of $C_2O_4^-$ to be the most stable isomer.[73, 75, 78]

The two isomers of the dimeric $CO_2$ anion have been observed in matrix isolation studies performed by Jacox and Andrews.[57-60, 82] Andrews reported that the monomeric anion, $CO_2^-$, and the separated dimeric anion cluster, $(CO_2)(CO_2^-)$ are present upon deposition. The dimeric anion $C_2O_4^-$, which is not present following deposition, is formed upon annealing of the matrix by the reaction of $CO_2^-$ with neutral $CO_2$ monomers.[59] In this chapter, a reexamination of the formation of $C_2O_4^-$ is discussed. These results indicate that $C_2O_4^-$ is in thermodynamic equilibrium with $(CO_2)(CO_2^-)$. They also appear to show that $(CO_2)(CO_2^-)$ is the more stable isomer in the matrices, in contrast to the previous computational results. It is possible that the interaction between the matrix and the dimeric anion results in the stabilization of the separated species.

### 4.2.1 Thermodynamic Equilibria in Matrix Isolation

An attractive aspect of the matrix-isolation technique is the fast energy dissipation of trapped species by the matrix. This property can lead to kinetic trapping of non-equilibrium distributions of molecules through deposition of hot molecular beams.[87-89] The energy difference between conformers can be determined by varying the temperature of the deposited gas. The relationship between the temperature of the gas and concentration of isomers can be used to generate a van't Hoff plot. This method has been used to calculate the enthalpy difference between conformers of halogenated hydrocarbons,[87] and has shown good agreement with gas-phase experiments. These pseudo-equilibrium processes are only dependent upon the temperature of the deposited gas, and not the temperature of the matrix, and upon annealing the unstable conformer can undergo a rearrangement to the stable isomer.

Thermally induced changes are limited to low-barrier processes due the inherent low temperature of matrix-isolation experiments. This requirement generally limits the observed thermally induced processes to simple conformational changes of trapped species.[20] If the barrier is very low, it is possible for both conformational isomers to be thermally accessible at experimental temperatures, and the two conformers can exist in equilibrium. Several examples exist of reversible interconversion between isomers in matrix-isolations studies, including the configuration of partially deuterated methanol,[90] internal rotation of the OH group in ethanol,[91] and the conversion between the trans- and gauche- forms of fluorinated alkanols.[92] The enthalpic barriers to these rearrangements have all been found to be under 0.5 kJ $mol^{-1}$, and the observation of these reversible

processes can be explained solely by the increase in temperature of the matrix providing enough thermal energy to overcome the barrier to rearrangement.[93]

To my knowledge, only two examples exist of reversible, temperature dependent processes that have higher enthalpy barriers than can be explained by thermally induced changes in the matrix. These processes require some entropic driving force. In 1999, Wight and coworkers discovered that the van der Waals complex F-FNO and the radical species $F_2NO$ existed in thermodynamic equilibrium as

$$F - FNO \underset{k_r}{\overset{k_f}{\rightleftharpoons}} F_2NO \tag{4.2}$$

with the van der Waals complex being favored at low temperature, and the radical being favored at high temperature.[94] Additionally, previous work in the Moore group found a thermodynamic equilibrium between two conformers of the oxygen dimer cation, *trans*-$O_4^+$ and cyclic-$O_4^+$, with the *trans* isomer being favored at low temperatures.[43]

It would be expected that each of these reactions would result in a lowering of the electronic energy of the system due to the formation of an F-N bond and an O-O bond, respectively. Additionally, due to this bond formation, the number of degrees of freedom of the system should be reduced, resulting in lower entropy for the final state compared to the initial state. On the basis of this rudimentary analysis, one would expect that the van der Waals complex, F-FNO, and the *trans*-$O_4^+$ species would be favored at high temperature, but the opposite is true in each case.

A van't Hoff plot for each system was generated using relative concentrations of the high and low temperature species as a function of inverse temperature. These plots were found to be linear for both systems, indicating thermodynamic equilibration, and

allowing determination of the standard enthalpy and entropy changes for each reaction. For each case, the enthalpy change was positive, indicating an endothermic reaction, and the driving force of the reaction was a large increase in entropy. The changes in enthalpy and entropy of the $F_2NO$ system were 1.24 kJ $mol^{-1}$ and 62 J $mol^{-1}$ $K^{-1}$, respectively, and the thermodynamic values for the $O_4^+$ system were 2.33 kJ $mol^{-1}$ and 171 J $mol^{-1}$ $K^{-1}$.[43, 94] Wight and coworkers rationalized the large increase in entropy by an increase in frustrated rotations of the $F_2NO$ species at high temperature. The larger entropy increase in the $O_4^+$ system represents a ~$10^9$ increase in the number of available microstates in the products compared to the reactants. This factor cannot be rationalized by simply considering an increase in the rotation of the component $O_2$ fragments, so the surrounding matrix must somehow be involved in the large entropy increase stabilizing the cyclic product.

In this chapter, the thermodynamic equilibrium of two dimeric $CO_2$ anion species, $(CO_2)(CO_2^-)$ and the oxalate-like $C_2O_4^-$, are discussed. Unlike previous equilibria observed in matrix isolation, the process occurs sufficiently that a full, temperature-dependent kinetic analysis of the system can be performed in addition to the thermodynamic van't Hoff analysis. Complete characterization of the reaction in both the forward and reverse direction, as well as two independent methods of analysis, kinetic and thermodynamic, yielded identical consistent results.

**4.3 Experimental Methods**

A 0.5% $CO_2$-doped argon matrix was deposited on a CsI IR window at a static backing pressure of ~$1x10^{-5}$ Torr for a period of six hours at either 10 or 20K, depending on desired experimental conditions. An 18 nA beam of high energy, 300 eV, $Ar^+$ was co-

deposited with the matrix. Both anionic and cationic $CO_2$ complexes were observed following deposition. Secondary ionization processes due to the high energy $Ar^+$ were presumably responsible for the formation of ions in the matrix. As discussed, a thermodynamic equilibrium of two dimeric $CO_2$ anions was observed. Matrix experiments with krypton were carried out using identical experimental conditions, except the minimum deposition temperature was 20K, and the matrix was annealed to temperatures as high as 35K. Thermodynamic and kinetic information was determined from analysis of FTIR spectra collected using a Nicolet 6700 FTIR spectrometer with an external, liquid-nitrogen-cooled MCT-A detector.

Matrix gas mixtures were generated by standard dilution techniques of $CO_2$ (99.999%, Air Gas) and argon (99.999%, Praxair). The matrix gas was delivered through a 1/8" stainless steel line directed toward the cold IR window at a rate of 3 SCCM set by an Alicat flow controller. The argon counter ion beam was generated by flowing argon (99.999%, Praxair) into an electron impact ionization source, which was guided toward the matrix through a series of optics and an octupole ion guide. The energy of the ion beam was confirmed via stopping-potential experiments.

The two species were observed to be in thermodynamic equilibrium between approximately 19K and 23K in argon and 26K and 32K in krypton. To obtain spectra for use in the thermodynamic analysis of the equilibrium, the two peaks fully equilibrated at a given temperature, as determined by continuously collecting spectra until no change in peak intensity was observed. A long average (500-1000 scans) spectrum was then collected for analysis of the equilibrated system at that temperature. This process was repeated at temperature intervals as small as 0.25K depending on the experiment. The

matrix was warmed and cooled repeatedly, and scans were taken in both the heating and cooling direction, to both ensure the equilibrium remained reversible after a series of temperature ramps and to check for any hysteresis affects. It is important to note that this procedure differs slightly from the standard procedure for collecting spectra in other experiments presented in this dissertation. Rather than collecting all spectra at a single temperature, such as 10K, throughout the entire experiment, the spectra were collected at the equilibrium temperatures.

Kinetic information was generated using the following procedure. First, the matrix was warmed to 25K or cooled to 10K to ensure only the corresponding high- or low-temperature conformer was present. Once the reaction had equilibrated at the chosen temperature, the temperature of the matrix was set within the equilibrium range. Data points were taken by continually obtaining short (50-100 scans averaged) spectra with the matrix held at the given temperature until the two species reached equilibrium. The time at which each spectrum was taken was recorded so that time-dependent growth and decay curves could be generated at a range of temperatures. Data taken at each temperature were then used to calculate values of temperature dependent rate constants. Rate constants for the forward reaction were determined by warming the matrix from 10K, and rate constants for the reverse reaction were obtained by cooling the matrix from 25K. The process for determining concentration from integrated peak areas, as well as fitting the data for kinetic studies is explained in detail in the Appendix.

## 4.4 Results

### 4.4.1 Argon Matrices

Following co-deposition at 10K of a 0.5% $CO_2$-doped argon matrix and an ~18 nA beam of high energy (300+ eV) $Ar^+$, various anionic and cationic $CO_2$ clusters were observed via infrared spectroscopy. The nature of these species was discussed in Chapter 3. Of note, a peak at 1652.7 $cm^{-1}$ has been assigned to $(CO_2)(CO_2)_x$ and a peak at 1657.0 $cm^{-1}$ has been assigned to $CO_2^-$ by Andrews.[59] He observed that after annealing the matrix to 25K, the two peaks at 1652.7 $cm^{-1}$ and 1657.0 $cm^{-1}$ were diminished, and two new peaks at 1856.9 $cm^{-1}$ and 1183.8 $cm^{-1}$ had grown in, which he assigned to the antisymmetric and symmetric stretching modes of $C_2O_4^-$, respectively. This behavior is highlighted in Figure 4.2. Andrews hypothesized that the growth of the $C_2O_4^-$ species is correlated with the loss of $CO_2^-$, suggesting it dimerized with free $CO_2$ in the matrix, but our results indicate that $C_2O_4^-$ in fact grows at the expense of the $(CO_2)(CO_2^-)$ species, not $CO_2^-$.

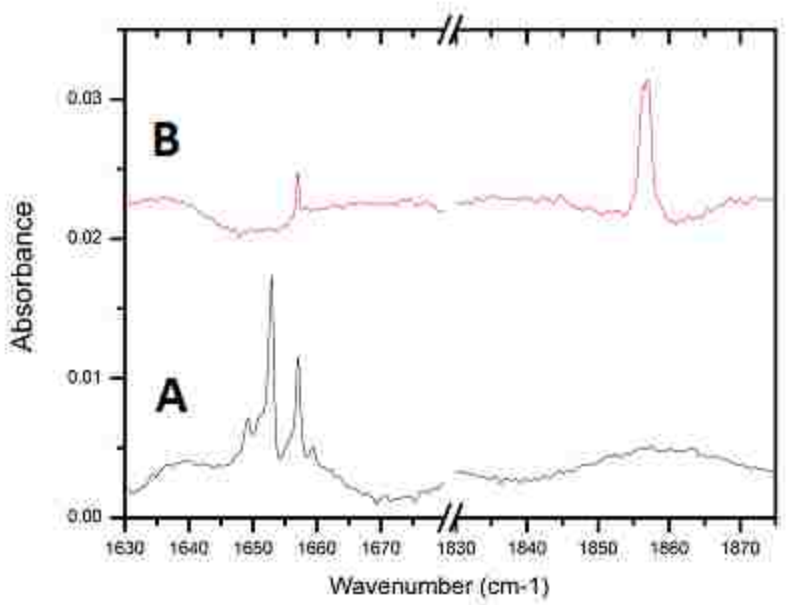


**Figure 4.2:** Infrared spectra taken at 10K (A) and 25K (B) showing the conversion of $(CO_2)(CO_2^-)$ to $C_2O_4^-$. The largest peak in spectrum A at 1652.7 $cm^{-1}$ is assigned to $(CO_2)(CO_2^-)$. The peak at 1657.0 $cm^{-1}$ is assigned to $CO_2^-$, and the two smaller satellite peaks at 1649.5 $cm^{-1}$ and 1659.4 $cm^{-1}$ are site peaks of the separated dimeric anion. In spectrum B, the peak at 1856.9 $cm^{-1}$ is assigned to $C_2O_4^-$. The peaks assigned to $(CO_2)(CO_2^-)$ are not present at 25K. The peak at 1657.0 $cm^{-1}$ is observed to respond reversibly with temperature but does not take part in the equilibrium. The two site peaks are irreversibly lost following the first conversion from $(CO_2)(CO_2^-)$ to $C_2O_4^-$.

We observed that following annealing, if the matrix was held at low temperature for an extended period of time, the peak located at 1652.7 $cm^{-1}$ began to regrow at the expense of the peak at 1856.9 $cm^{-1}$. Full conversion back to the low-temperature species occurred over a period of approximately 1.5 hours. The time-dependent conversion of the peak at 1856.9 $cm^{-1}$ converting back to 1652.7 $cm^{-1}$ at 14K following cooling from 25K is shown in Figure 4.3.

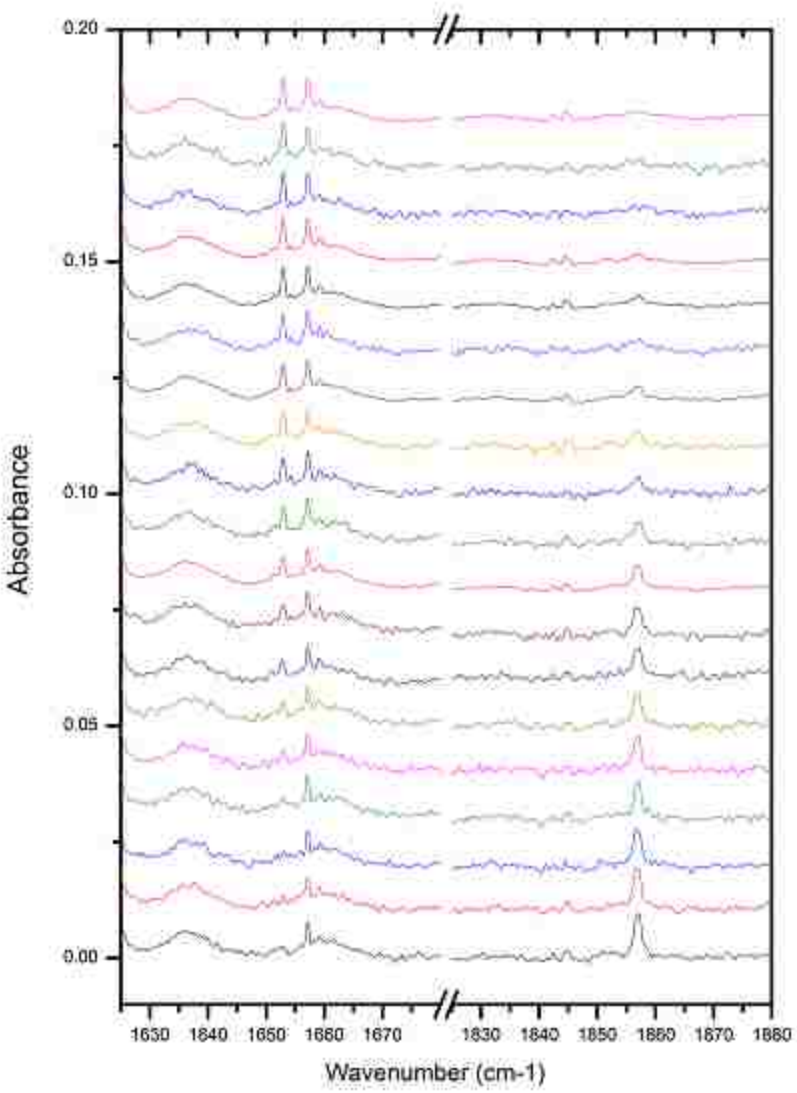


**Figure 4.3:** Time-dependent conversion of $C_2O_4^-$ to $(CO_2)(CO_2^-)$. All spectra were taken at 14K following cooling from 25K. The time required to cool the matrix from 25K to 14K was 2.5 minutes. The bottom spectrum was collected immediately upon reaching 14K and the spectra are shown sequentially in time from bottom to top, with the final spectrum being taken 110 minutes after the first.

Reversible conversion of $C_2O_4^-$ to $(CO_2)(CO_2^-)$ was an unexpected observation, so I sought to find a temperature range where the two species existed in equilibrium. The peak located at 1652.7 $cm^{-1}$, $(CO_2)(CO_2^-)$, began to lose intensity between 18-19K, and was fully depleted at approximately 23K. This loss of signal corresponded to a growth in intensity of the peak at 1856.9 $cm^{-1}$, $C_2O_4^-$, over the same temperature range. A peak at

1183.8 $cm^{-1}$, assigned to the symmetric stretching mode of $C_2O_4^-$, also exhibited temperature-dependent intensity correlated with the higher intensity 1856.9 $cm^{-1}$ peak. The peak located at 1856.9 $cm^{-1}$ was used for further analysis. The peak at 1657.0 $cm^{-1}$, $CO_2^-$, which is visible in Figures 4.2 – 4.4, also responded reversibly with temperature, but is not part of the equilibrium process. This result is also verified in the Appendix.

### 4.4.2 Thermodynamic van't Hoff Analysis

For the reversible conversion of the dimeric $CO_2$ anions at temperatures between 19K and 23K, and for the process of obtaining kinetic data, the matrix was cycled through the equilibrium temperature range more than ten times without a loss of reversibility. This result is in contrast to some earlier examples of matrix-isolated equilibration processes, which showed a dependence on the history of the matrix.[90] Figure 4.4 shows a series of spectra to illustrate the reversible conversion with temperature, taken sequentially as the matrix was cooled and then warmed through the equilibrium temperature range.

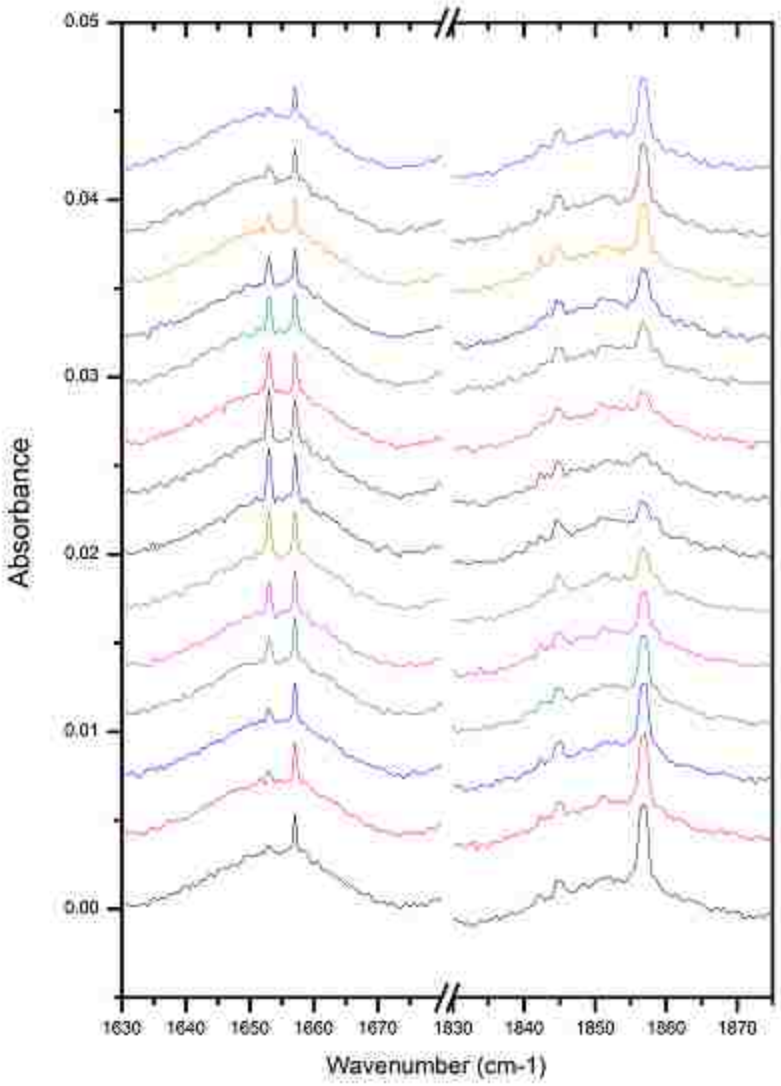


**Figure 4.4:** A series of infrared spectra taken through the range of equilibrium temperatures, taken sequentially from bottom to top. The bottom spectrum is taken at 22.5K, and the six subsequent spectra are taken as the matrix is cooled in 0.5K intervals to 19.5K. The eighth spectrum (brown) is taken at 19.25K, and the remaining spectra are taken at 0.5K intervals back up to 22.25K.

To obtain thermodynamic information through a van't Hoff analysis of the system, the two species were brought to come to equilibrium at a desired temperature. The system was deemed to have reached equilibrium by tracking the intensity of the two peaks with time, determined by continuously obtaining short (50-100 scans averaged)

spectra until the intensity of the two peaks was observed to stop changing. Since the two species were participating in a thermodynamic equilibrium, the total population of the two species must remain constant at all temperatures. As explained fully in the peak fitting section in the Appendix, plotting the equilibrated, integrated areas of the two peaks against each other should show a linear relationship between the peak areas. This result is shown in Figure 4.13. Coefficients relating the peak area to relative concentration of the two peaks can be determined from the slope and intercept of the line fit to these data.

The relative equilibrium concentrations of $C_2O_4^-$ and $(CO_2)(CO_2^-)$ were determined at each temperature. The values for changes in standard enthalpy and entropy were calculated according to the linear van't Hoff equation

$$\ln K = \frac{-\Delta H^o}{R}\left(\frac{1}{T}\right) + \frac{\Delta S^o}{R} \tag{4.3}$$

If the values for changes in standard enthalpy and entropy for the reaction remain constant over the entire temperature range, a plot of the natural log of the equilibrium constant, K, against 1/T should form a straight line, as shown in Figure 4.5. The equilibrium constant, K, is defined as $\frac{[C_2O_4^-]}{[(CO_2)(CO_2^-]}$. Using the van't Hoff equation, the slope of the line of best fit is defined as $\frac{-\Delta H^0}{R}$ and the intercept is defined as $\frac{\Delta S^0}{R}$. The negative slope observed in Figure 4.5 is consistent with an endothermic reaction. The values for changes in standard enthalpy and entropy calculated from the plot in Figure 4.5 are $3.67 \pm 0.11$ kJ mol$^{-1}$ and $177 \pm 5$ J mol$^{-1}$ K$^{-1}$, respectively.

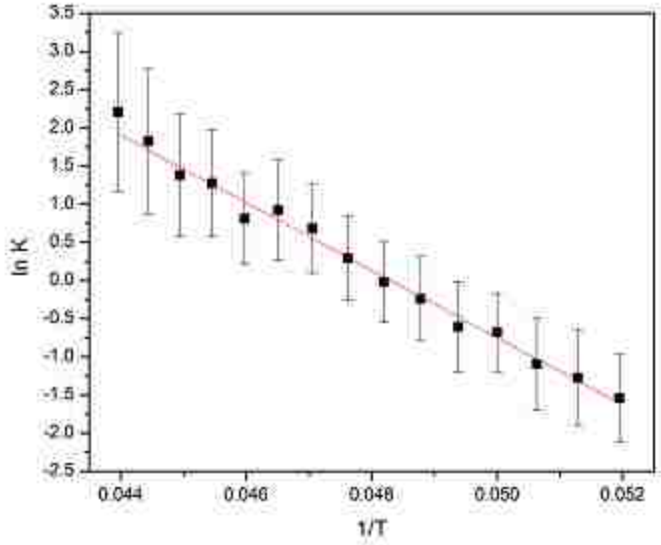


**Figure 4.5:** Natural log of ratio of equilibrium concentrations of $C_2O_4^-$ to $(CO_2)(CO_2^-)$ plotted against inverse temperature. The data points were taken in the temperature range of 19.25K to 22.75K in 0.25K intervals. The slope of the line of best fit is -441 ± 13 K and the intercept is 21.3 ± 0.7. The linear fit is very good, with an $r^2$ value of 0.987.

### 4.4.3 Kinetic Analysis

The procedure for obtaining spectra for a kinetic characterization of the equilibrium process is explained in the Experimental section. Kinetic curves were generated in the temperature range of 19K to 23K. If the equilibrium reaction is taken to be

$$(CO_2)(CO_2^-) \rightleftharpoons C_2O_4^- \tag{4.3}$$

then warming from 10K provides a kinetic growth curve for $C_2O_4^-$ and a kinetic decay curve for $(CO_2)(CO_2^-)$, while cooling from 25K will yield a decay curve fore $C_2O_4^-$ and a growth curve for $(CO_2)(CO_2^-)$. In theory, a growth curve and decay curve for each species could be collected for each temperature by starting the matrix at 10K and warming to the equilibrium temperature, or starting the matrix at 25K and cooling to the equilibrium

temperature. In practice, however, data for some temperatures in the equilibrium range could either not be obtained, or only obtained for one direction. There were two potential reasons data could not be obtained at a specific temperature: small changes to integrated peak intensity with time, which is apparent when warming from 10K to a low temperature in the equilibrium (i.e. 19K), or cooling from 25K to a high temperature in the equilibrium (i.e. 23K); and the species reaching equilibrium too quickly, preventing an adequate number of data points to be collected, which was a problem when warming from 10K to the higher end of the temperature range. Curves for the reaction in both directions were generated at 0.5K intervals between 19K and 23K for as many temperatures as possible that were not disqualified for one of the two reasons above.

The kinetic curves were fit to one of three equations that were derived from the rate law for a reversible, unimolecular reaction. The full derivation is shown in the Appendix. The first of these equations

$$\frac{[B]}{[A]_0} = \left(\frac{k_f}{k_r + k_f}\right)\left(1 - e^{-(k_f + k_r)(t - t_0)}\right) \tag{4.4}$$

was used to fit the kinetic growth curves. The variables $[A]_0$, [B], $k_r$, and $k_f$ are dependent upon the initial conditions of the equilibrium. In this equation, [B] refers to the species gaining concentration with time, and [A] refers to the species losing concentration with time, so when warming from 10K, [B] is the concentration of $C_2O_4^-$. Therefore, $[A]_0$ represents the concentration of the species initially present at low or high temperature. Since the relative concentrations of the species are being used, $[A]_0$ is defined as unity, as the kinetic experiment begins with a single conformer present. The forward rate constant is defined with respect to the species initially present, so if warming from 10K, $k_f$ is the

rate at which $(CO_2)(CO_2^-)$ converts to $C_2O_4^-$. The equation is fit to data using the Origin software's built in nonlinear fitting function. The variables in Equation 4.4 which are fit are $k_r$, $t_0$, and sum ($k_r + k_f$). Figure 4.6 shows characteristic kinetic curves which have been fit by Equation 4.4. Figure 4.6 (A) shows the growth in concentration of the high temperature species, $C_2O_4^-$, with time. The matrix, initially at 10K, was warmed and held at 20K to generate this curve. Figure 4.6 (B) shows the growth of the low temperature species, $(CO_2)(CO_2^-)$, with time. To generate this curve, the matrix was initially held at 25K and then cooled to and held at 20K.

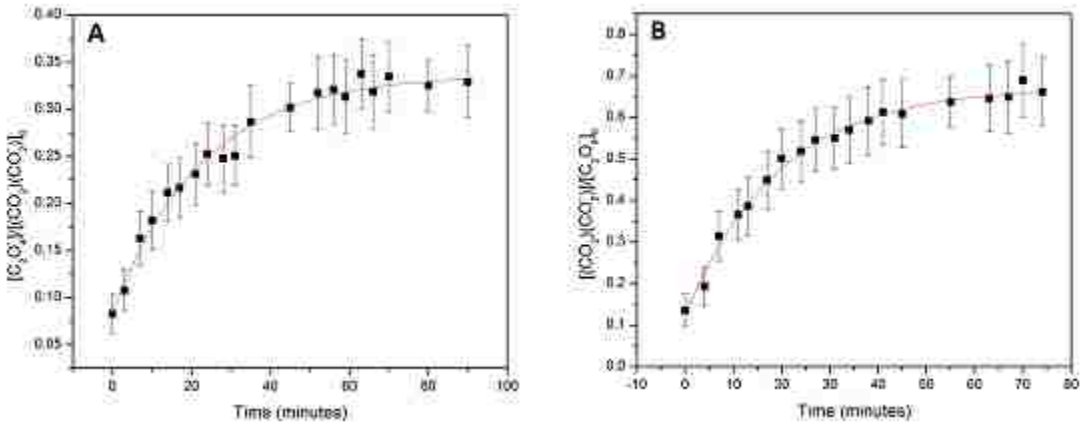


**Figure 4.6:** Kinetic growth curves for (A) $C_2O_4^-$ at 20K following warming from the an equilibrium state at 10K, and (B) $(CO_2)(CO_2^-)$ at 20K following cooling from an equilibrium state at 25K. The data were fit using equation 4.4. The following were the fit parameters: (A) sum: 0.044 ± 0.003 $min^{-1}$, $k_r$: 0.029 ± 0.002 $min^{-1}$, $t_0$: -6.5 ± 0.7 min (B) sum: 0.051 ± 0.003 $min^{-1}$, $k_r$: 0.017 ± 0.002 $min^{-1}$, $t_0$: -4.0 ± 0.5 min. Note that $k_r$ and $k_f$ are relative to the starting point of the reaction as described in the body of the text.

A second equation was derived to be used for fitting the decay curves. In the equation

$$\frac{[A]}{[A]_0} = \left(\frac{k_f}{k_r + k_f}\right) e^{-(k_r+k_f)(t-t_0)} \tag{4.5}$$

where [A] is defined as the concentration of the decaying species, so [A] represents the concentration of $(CO_2)(CO_2^-)$ when the matrix is initially at 10K and warmed to an

equilibrium temperature, and to the concentration of $C_2O_4^-$ when the matrix begins at 25K and is cooled. In the same manner as equation 4.4, $[A]_0$ is defined as unity, and the rate constants are defined in the same manner based on the initial condition of the equilibrium. Figure 4.7 shows examples of kinetic curves fit by equation 4.5. Figure 4.7 (A) shows the decay of $(CO_2)(CO_2^-)$ with time, after the matrix initially held at 10K was warmed to 20K, and (B) shows the decay of $C_2O_4^-$ after cooling the matrix from 25K to 20K.

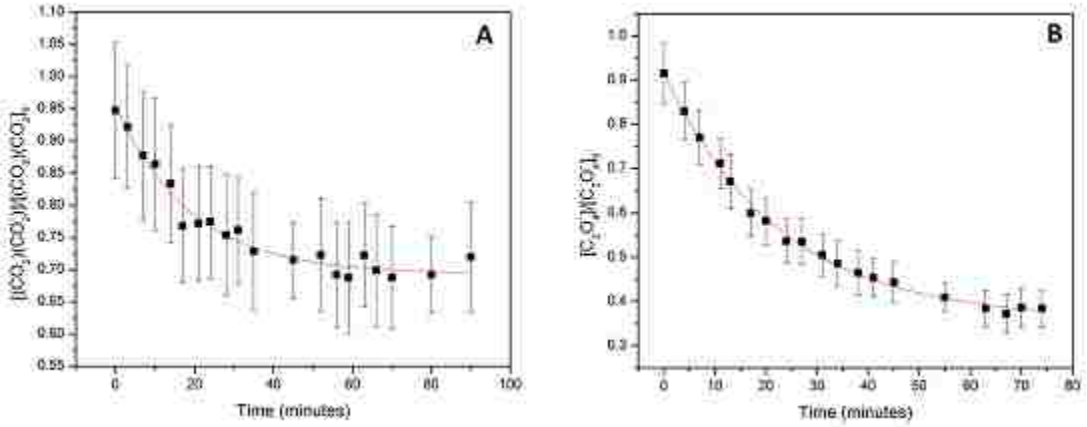


**Figure 4.7:** Kinetic decay curves for (A) $(CO_2)(CO_2^-)$ at 20K following warming of the matrix from an equilibrium state at 10K, and (B) $C_2O_4^-$ at 20K following cooling of the matrix from an equilibrium state at 25K. The data were fit using equation 4.5. The following are the fit parameters: (A) sum: 0.053 ± 0.006 $min^{-1}$, $k_r$: 0.037 ± 0.004 $min^{-1}$, $t_0$: -2.8 ± 1.1 min (B) sum: 0.044 ± 0.002 $min^{-1}$, $k_r$: 0.0159 ± 0.0008 $min^{-1}$, $t_0$: -3.1 ± 0.4 min. Note that $k_r$ is dependent upon initial state of equilibrium.

The two previous equations rely only on data from one of the two species in the equilibrium, so two fits could be carried out at each temperature for each direction of the reaction, which leads to multiple independently calculated values for $k_f$ and $k_r$ at a given temperature. A third equation

$$\frac{[A]}{[B]} = \frac{k_f(1 - e^{-(k_f+k_r)(t-t_0)})}{k_r + k_f e^{-(k_f+k_r)(t-t_0)}} \tag{4.6}$$

was developed in an effort to allow the calculation of $k_f$ and $k_r$ using both species simultaneously. For this equation, [A] corresponds to the species growing in concentration, and [B] corresponds to the species whose concentration is decaying. Again, $k_f$ and $k_r$ are dependent on the starting conditions of the equilibrium. Figure 4.8 shows two characteristic fits using equation 4.6. Figure 4.8 (A) shows the ratio of concentration of $C_2O_4^-/(CO_2)(CO_2^-)$ at 20K with time following warming the matrix from 10K, and (B) shows the ratio of concentration of $(CO_2)(CO_2^-)/C_2O_4^-$ with time at 20K following cooling the matrix from 25K.

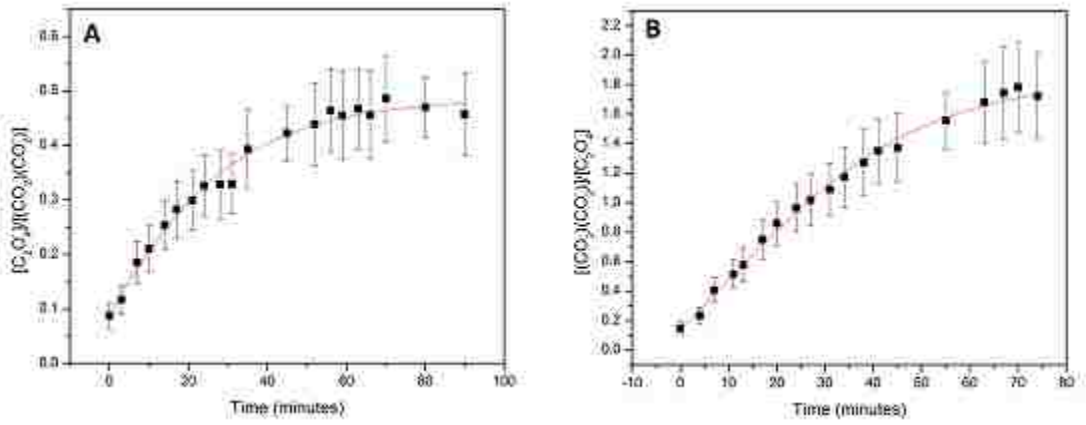


**Figure 4.8:** Ratio of the relative concentration of (A) $C_2O_4^-/(CO_2)(CO_2^-)$ with time at 20K following warming from an equilibrated state at 10K, and (B) $(CO_2)(CO_2^-)/C_2O_4^-$ with time at 20K following cooling from an equilibrated state at 25K. Both sets of data were fit using equation 4.6. The fit parameters were as follows: (A) sum: 0.046 ± 0.003 $min^{-1}$, $k_r$: 0.0150 ± 0.0007 $min^{-1}$, $t_0$: -6.1 ± 0.6 min (B) sum: 0.048 ± 0.002 $min^{-1}$, $k_r$: 0.031 ± 0.001 $min^{-1}$, $t_0$: -4.3 ± 0.4 min. Note that $k_r$ is dependent upon initial state of equilibrium.

Values for the kinetic rate constants calculated from each fitting equation show good consistency, especially for $k_r$. Comparing values of the kinetic rate constants for the experiment which began at 10K, with the equilibrium fully on the side of $(CO_2)(CO_2^-)$, and then warming to 20K, the values of $k_r$ calculated using equations 4.4, 4.5, and 4.6 are 0.029, 0.037, and 0.031 $min^{-1}$, respectively. The calculated values for $k_f$, found by

subtracting the $k_r$ value from the "sum" variable, were 0.015, 0.016, and 0.017 $min^{-1}$. As has been discussed, when fitting curves which were generated *via* cooling from 25K, the physical meanings of the rate constants $k_f$ and $k_r$ are reversed. The $k_f$ values from the fit for the three methods are 0.017, 0.016, and 0.015 $min^{-1}$. The $k_r$ values calculated from subtracting the values of $k_f$ from the sum variable are 0.034, 0.028, and 0.031 $min^{-1}$. In addition to showing good agreement between the three fitting equations, the rate constants are consistent whether they are calculated from either starting point of the equilibrium. Tables 4.1 to 4.6 in the appendix show a characteristic set of $k_f$ and $k_r$ values calculated using each method from a full set of temperatures.

### 4.4.4 Transition State Theory: The Eyring Equation

Transition state theory was developed by Eyring[95] and by Evans and Polanyi[96] in an attempt to calculate the absolute rate constant of a reaction. In brief, the theory states that during a chemical reaction, reactants form an activated complex, or transition state, before forming products. An elementary, unimolecular reaction could be represented as

$$A \rightarrow X^{\ddagger} \rightarrow B \tag{4.7}$$

where A is the reactant, $X^{\ddagger}$ is the transition state, and B is the product. The two fundamental assumptions of transition state theory are that once a reactant molecule has crossed into the transition state, it must go on to form a product molecule, and that in the transition state, motion along the reaction coordinate can be separated from all other molecular motions (vibration, rotation, etc.) and treated as classical translation. In an equilibrium process, there are two types of transition states: those originating from the reactant side and those originating from the product side. At equilibrium, the

concentration of transition states originating from each side of the reaction will be equal. These assumptions allow the derivation of the Eyring equation, which takes the form

$$k = \frac{k_B T}{h} e^{-\frac{\Delta G^{\ddagger}}{RT}} \tag{4.8}$$

where $\Delta G^{\ddagger}$ is the Gibbs energy of activation, $k_B$ is the Boltzmann constant, and h is Planck's constant. The equation can be rewritten by substituting $\Delta G^{\ddagger}$ with $\Delta S^{\ddagger}$ and $\Delta H^{\ddagger}$. If the equation is linearized, it takes the form

$$ln\frac{k}{T} = \frac{-\Delta H^{\ddagger}}{R}\frac{1}{T} + ln\frac{k_B}{h} + \frac{\Delta S^{\ddagger}}{R} \tag{4.9}$$

The Eyring equation can be used to determine enthalpic and entropic reaction barriers. A plot of $\ln(\frac{k}{T})$ vs $\frac{1}{T}$ should yield a straight line with a slope of $\frac{-\Delta H^{\ddagger}}{R}$, from which the enthalpic barrier can be found, and an intercept of $ln\frac{k_B}{h} + \frac{\Delta S^{\ddagger}}{R}$, from which the entropic barrier can be found.

If the rate constants for the dimeric $CO_2$ anion equilibrium reaction are defined as

$$(CO_2)(CO_2^-) \underset{k_r}{\overset{k_f}{\rightleftharpoons}} C_2O_4^- \tag{4.10}$$

then temperature dependent values of $k_f$ and $k_r$ can be calculated and plotted in accordance with the linear form of the Eyring equation, as shown in Figure 4.9, to determine the enthalpic and entropic reaction barriers in both the forward and reverse direction. The enthalpic and entropic activation barriers in the forward direction, calculated from the slope and intercept of the best fit line shown in Figure 4.9 (A), are 3.5 ± 0.3 kJ $mol^{-1}$ and -81 ± 12 J $mol^{-1}$ $K^{-1}$, respectively. The near-zero slope of the trendline in Figure 4.9 (B) indicates a nearly barrierless enthalpic transition for the reverse

reaction. The calculated values for the enthalpic and entropic activation barriers for the reverse reaction are 0.04 ± 0.1 kJ $mol^{-1}$ and -250 ± 30 J $mol^{-1}$ $K^{-1}$, respectively. These values are in excellent agreement with the standard enthalpy and entropy changes calculated from the van't Hoff analysis.

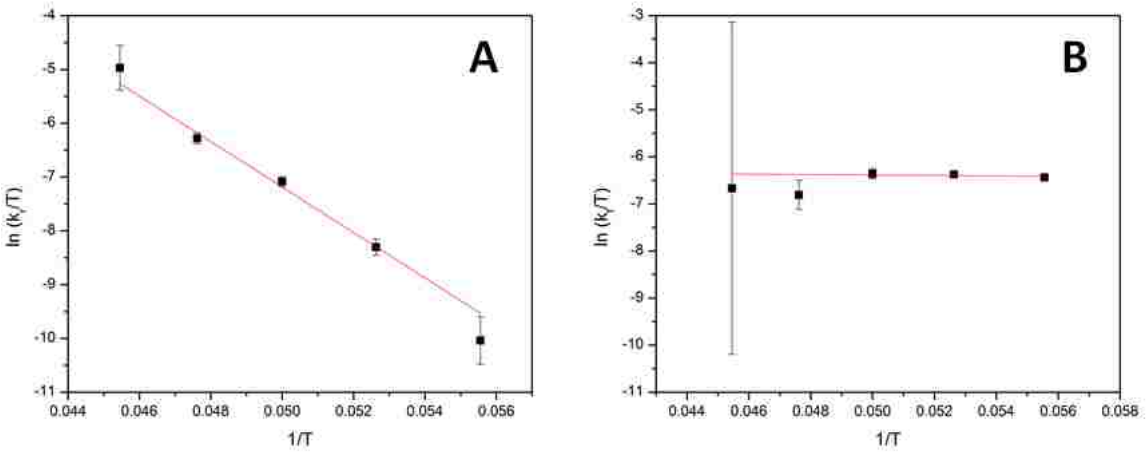


**Figure 4.9:** Eyring equation plots for the forward reaction (A) and the reverse reaction (B). (A) has a slope of -422 ± 35 K and an intercept of 13 ± 1.7 K. (B) has a slope of -4.8 ± 17 K and an intercept of -6.1 ± 0.9 K.

### 4.4.5 Nitrogen and Krypton Matrices

In an attempt to develop a greater understanding of the role of the matrix in the observed equilibrium process, other matrix materials were tested in addition to argon. A nitrogen matrix doped with 0.5% $CO_2$ was deposited at 10K under otherwise identical conditions to the argon experiments previously described. A single sharp peak was observed at 1652.4 $cm^{-1}$ in the $CO_2$ anion antisymmetric stretching region. As discussed in the previous chapter, future experiments using isotopic substitution will be required to determine if this peak corresponds to the dimer anion $(CO_2)(CO_2^-)$, or the monomer $CO_2^-$. Annealing to 25K resulted in significant matrix loss, but no peak which could be attributed to $C_2O_4^-$ was observed. The matrix was annealed at as high as 35K without any

conversion of the peak at 1652.4 $cm^{-1}$. In addition, annealing to 35K resulted in almost complete loss of the peak at 1652.4 $cm^{-1}$, likely as a result of matrix loss, so it was impossible to anneal the matrix to a higher temperature to determine if conversion would occur at any temperature.

Experiments in krypton matrices yielded more successful results than the studies using nitrogen. Under otherwise identical experimental conditions, with a krypton matrix doped with 0.5% $CO_2$ and 10K deposition, only very small peaks were observed in the spectral region of interest. The krypton matrix may be more efficient at trapping the $CO_2$ molecules at 10K than argon, which could prevent the formation of a significant concentration of dimer species. When the deposition temperature was increased to 20K, and a single peak was observed at 1651.2 $cm^{-1}$, which we identified as the $(CO_2)(CO_2^-)$ species. Upon annealing to 35K, the peak at 1651.2 $cm^{-1}$ was fully diminished, and two peaks were observed to have grown in at 1851.8 $cm^{-1}$ and 1856.4 $cm^{-1}$. The two sets of peaks underwent reversible conversion between 26K and 32K. Spectra showing the temperature dependence of the peaks are provided in Figure 4.10. The two peaks that appeared at high temperature arose from a single matrix isolated species, verified by the ensuing thermodynamic analysis.

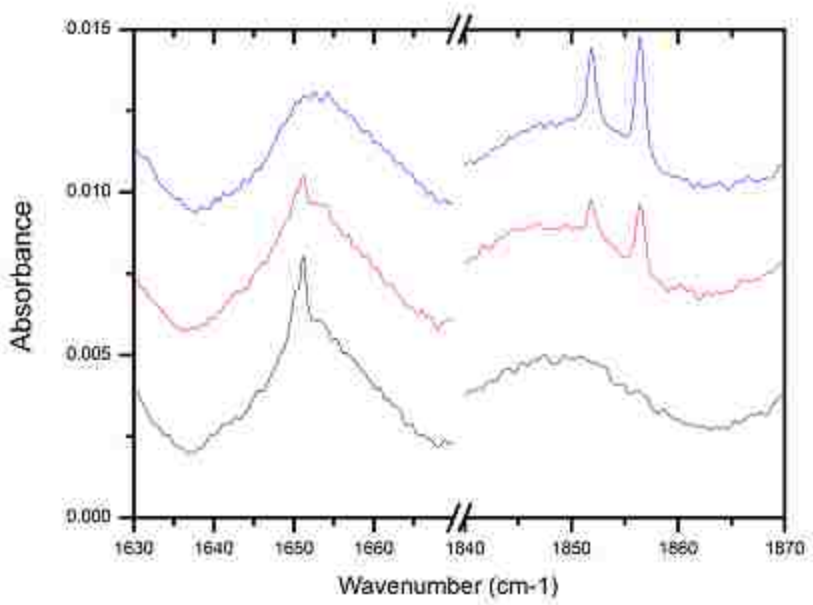


**Figure 4.10:** Infrared spectra of the equilibrium system taken in a krypton matrix at 26K (black), 29K (red), and 32K (blue) following deposition of a 0.5% $CO_2$-doped Kr matrix deposited at 20K with an 18 nA beam of $Ar^+$. The peak at 1651 $cm^{-1}$ has been assigned to $(CO_2)(CO_2^-)$. The peaks at 1851 and 1856.4 $cm^{-1}$ are assigned to $C_2O_4^-$.

A van't Hoff analysis of the system was carried out using the same method described for the argon matrix. The single peak at 1651.2 $cm^{-1}$ was treated the same as the 1652.7 $cm^{-1}$ peak in argon. The two peaks at 1851.8 and 1856.4 $cm^{-1}$ were treated similarly to the 1856.9 $cm^{-1}$ peak in argon, but to ensure that the two peaks arose from the same species, the van't Hoff analysis was carried out three times. The analysis was performed treating each of the two peaks individually, and then a third time by taking the sum of the integrated area of the two peaks and using that to determine the relative concentration of the high temperature species. All three methods produced identical van't Hoff plots, within error. The plot generated by taking the sum of the areas of the two peaks is shown in Figure 4.11. The thermodynamic values determined for the changes in standard enthalpy and entropy of the reaction were 4.91 ± 0.19 kJ $mol^{-1}$ and

$170 \pm 7$ J $mol^{-1}$ $K^{-1}$. The reaction is more endothermic in krypton compared to argon, but interestingly has the same associated change in entropy. Unfortunately, the kinetic analysis performed in the argon system could not be replicated in krypton. The two species fully equilibrated within approximately five minutes at all temperatures within the equilibrium temperature range, which is faster than a sufficient number of spectra could be collected to generate growth and decay curves.

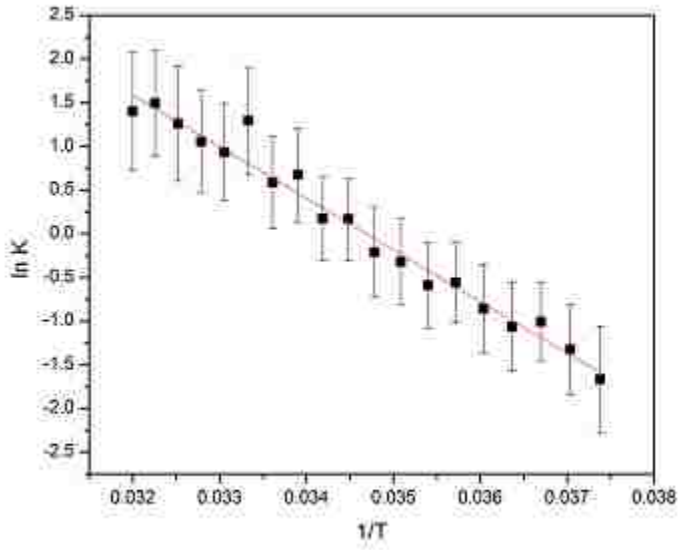


**Figure 4.11:** A van't Hoff plot generated from the krypton equilibrium system using the sum of the integrated areas of the two high temperature peaks. Data points are taken over the temperature range of 26.75K to 31.25K in 0.25K intervals. The slope of the trend line is $-590 \pm 23$ K and the intercept is $20.5 \pm 0.8$ with an $r^2$ value of 0.973. This corresponds to $\Delta H^o = 4.91 \pm 0.19$ kJ $mol^{-1}$ and $\Delta S^o = 170 \pm 7$ J $mol^{-1}$ $K^{-1}$.

### 4.5 Discussion

Considering the results of the thermodynamic and kinetic analysis in the context of one another provide some exciting conclusions. The kinetic analysis reveals that the reverse reaction, $C_2O_4^-$ converting back to $(CO_2)(CO_2^-)$, has no enthalpic barrier, as evidenced by the lack of temperature dependence of the reverse rate constant, suggesting

that the high-temperature isomer exists purely due to entropic stabilization. The enthalpic barrier to the forward reaction is found to be 3.5 ± 0.3 kJ $mol^{-1}$, which is equivalent within error to the 3.67 ± 0.11 kJ $mol^{-1}$ change in standard enthalpy of the reaction found using the van't Hoff analysis. The kinetic analysis provides a value for the activation entropy with respect to the reactant and product of the reaction. The transition state is found to be 81 J $mol^{-1}$ $K^{-1}$ below the reactant, $(CO_2)(CO_2^-)$, and 250 J $mol^{-1}$ $K^{-1}$ below the product, $C_2O_4^-$. Therefore, the entropy difference between $(CO_2)(CO_2^-)$ and $C_2O_4^-$ is approximately 170 ± 30 J $mol^{-1}$ $K^{-1}$, which is very close to the change in standard entropy of 177 ± 5 J $mol^{-1}$ $K^{-1}$ found *via* the thermodynamic analysis. The strong agreement between the two methods strengthens the confidence in each, as the two methods produced the thermodynamic values independently of the other. These results are visualized in a schematic diagram of the reaction pathway, shown in Figure 4.12.

A visualization of a possible free energy surfaces at low and high temperature are shown in Figure 4.12 C and D. Due to the temperature dependence of the entropic contribution, arising from the definition of free energy,

$$\Delta G = \Delta H - T\Delta S \tag{4.41}$$

at low temperature the enthalpy difference will drive the reaction to favor the separated dimeric anion species. The contribution of entropic stabilization becomes more pronounced at higher temperature, and will eventually overtake the enthalpy difference as the driving force for the reaction. At this point, formation of the oxalate-like dimer will become favored.

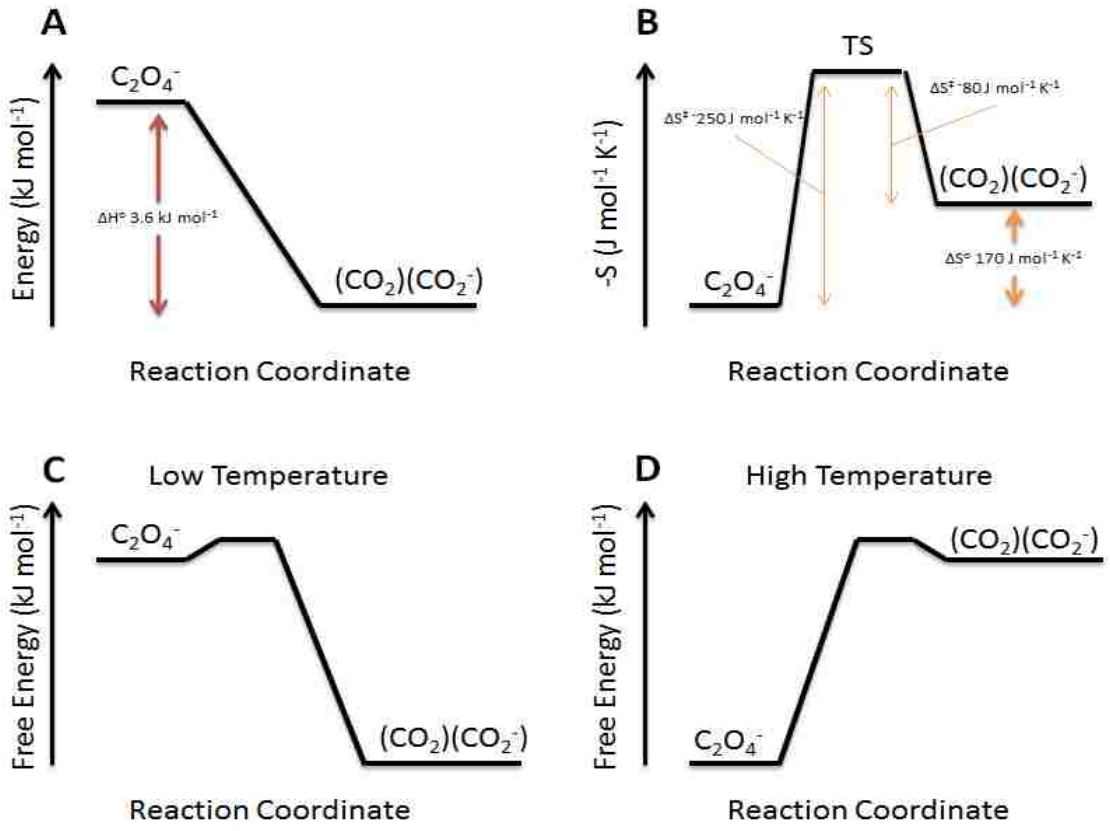


**Figure 4.12:** Visualizations of the (A) enthalpic, (B) entropic, and free energy surfaces at (C) low and (D) high temperature for the isomerization of dimeric $CO_2$ anions.

It is interesting to consider the large entropy change induced by this reaction. The formation of $C_2O_4^-$ from $(CO_2)(CO_2^-)$ requires the formation of a carbon-carbon bond which would convert the translational degrees of freedom of one of the two monomer units into vibrational degrees of freedom, which should result in entropic destabilization. This first principles argument leads to the wrong conclusion in this system. In an earlier example of a matrix-isolated thermodynamic equilibrium, described briefly in the introduction, the Wight group found that the van der Waals complex F—FNO underwent a similar process of entropic stabilization when it converted to $F_2NO$ at higher temperatures.[94] This gain was justified by an increase in the ability of the radical to

undergo frustrated rotations in the matrix, compared to that of the separated van der Waals complex. The entropy of the $F_2NO$ system was 62 J $mol^{-1}$ $K^{-1}$, which when considering the statistical Boltzmann definition for entropy $S^o = k_B \ln(W)$, where W is the number of available microstates, corresponds to a ~1.7 x $10^3$ increase in the number of available microstates. In the present case, the entropy of 171 J $mol^{-1}$ $K^{-1}$ corresponds to an ~8 x $10^8$ increase in the number of available microstates, which cannot be explained simply through the increased availability of rotational states to the $C_2O_4^-$ product. In the matrix-isolated thermodynamic equilibrium of *trans*-$O_4^+$ converting to cyclic-$O_4^+$, which has been characterized by Ryan Ludwig,[43] a former member of the Moore group, the change in entropy associated with the conformational change is also very close to 170 J $mol^{-1}$ $K^{-1}$.

Examining the behavior of the equilibrium in other matrix materials may also help provide insight into the driving force behind the reaction. The equilibrium occurs between 26K and 32K in krypton, higher than the temperature required for argon, and that is illustrated in the increased enthalpy change determined by the van't Hoff analysis of that system. Surprisingly, the entropy changes associated with the reaction in both argon and krypton were found to be the same within error. If the long range ordering of the matrix, or the interaction between the trapped molecules and the matrix cage provide the entropy required to drive the reaction, it is possible that the differences in these interactions are small enough between the two matrix materials to not have a direct effect on the entropy change of the reaction. The identical change in entropy between the matrix materials argues against this explanation, as one would expect significant differences in the guest-cage interactions of argon and krypton matrices. The difference in the shape of

the cage created by the molecular $N_2$ matrix, compared to the atomic Kr and Ar matrices, or the change in the band structure due to nitrogen containing covalent bonds, may be why the conversion is not observed in $N_2$ matrix experiments.

It is necessary to consider these findings in the broader context of other studies performed on anionic $CO_2$ clusters. The consensus among previously published results is that the minimum energy structure of the $CO_2$ dimer anion is $C_2O_4^-$ with $D_{2d}$ symmetry, but both the kinetic and thermodynamic analysis performed on the equilibrium process in the matrix indicate that the separated dimer, $(CO_2)(CO_2^-)$, is more stable at low temperature. Experimental studies on anionic $CO_2$ clusters have shown a dependence on the size of the cluster and the nature of the anion within the cluster.[79, 84, 86] This behavior is referred to as "core-ion switching." For smaller $(CO_2)_n^-$ clusters, where $n < 6$, the charge delocalizes over two $CO_2$ monomer units, forming a $C_2O_4^-$ species solvated by (n–2) neutral $CO_2$ molecules. However, for clusters with size $6 < n < 14$, the extra electron will be localized on a single $CO_2$ with (n – 1) neutral solvating molecules. The charge localization appears to be a function of the geometry of the solvating neutral molecules in the cluster.[79, 80] The symmetry of the solvating $CO_2$ molecules appears to be the driving force behind the core-ion switching. The solvating molecules tend to bind to one another and the ion, which leads to an asymmetric arrangement of solvating $CO_2$ molecules about the $C_2O_4^-$ core, stabilizing one of the $CO_2$ molecules in the dimer anion pair.[80, 85] At $n = 7$, the stabilization is sufficient to switch the core-ion to $CO_2^-$ fully. It has been noted that $n = 6$, where both ion cores are observed, corresponds to a half filled solvation shell about the dimer anion. The core ion switches back at larger cluster sizes due to a full solvation shell stabilizing the two central $CO_2$ units equally.[80]

In my experiments, the matrix must have a role in the observation that the separated dimer $(CO_2)(CO_2^-)$ is the thermodynamically stable structure. Considering the role of solvating $CO_2$ molecules on the nature of the core ion in anionic $CO_2$ clusters, it would seem that at low temperature the matrix cage preferentially stabilizes one of the two $CO_2$ monomer units, localizating the charge on a monomeric unit. The role of the matrix in the formation of the $C_2O_4^-$ species is less clear, and possible explanations are speculative at best. The charge is symmetrically distributed over the oxalate-like dimer,. Therefore, presumably, the charge can be delocalized over a greater volume of matrix states in the oxalate-like conformation, which could contribute to the observed entropic stabilization. The cage could become less rigid at higher temperatures, allowing the necessary structural rearrangement to occur to form $C_2O_4^-$, or the barrier to rearrangement could be low enough that the thermal energy provided by annealing the matrix could be enough to overcome the barrier. It is also possible that the matrix undergoes a structural change, forming a cage which solvates the dimer anion more symmetrically, resulting in equal stabilization of the two $CO_2$ units such that it becomes more stable for the charge to be shared. This explanation seems unlikely as annealing it is thought to irreversibly alter the crystal structure of the matrix,[3] which would hinder conversion back to $(CO_2)(CO_2^-)$.

An astonishing factor of these results, that is yet to be fully understood, is the huge disparity reflected in the configurational entropies (W) of the products, reactants and transition state. The $\Delta S^{\ddagger}$ increase of 250 J $mol^{-1}$ $K^{-1}$ between the transition state and the products reflects a ~$1x10^{13}$-fold increase in W, which is somehow being effected at the low temperatures where the reaction is characterized. This is difficult to rationalize given standard models of molecules trapped in solid rare gases, and points to an

additional reservoir of closely spaced states that can be accessed by the products, and to a lesser extent by the reactants, but which is closed off from the transition state. We speculate that the only possible candidate for such a reservoir involves the delocalization of the charge off of the ionic-complex into conduction band-like states of the matrix in the vicinity of the site where it is trapped.

### 4.6 Conclusions and Future Work

The identification and characterization of a thermodynamic equilibrium between different conformers of $CO_2$ dimer anions has been performed in both krypton and argon matrices. While thermodynamic and kinetic analysis of the systems has yielded consistent values for the change in standard entropy and enthalpy of the reactions, the physical reason for the large entropic driving force has yet to be determined. Experiments in neon may provide more information regarding the interaction between the equilibrium system and the surrounding matrix, and it would likely be illuminating regardless of whether the calculated entropy of the neon system was the same or different than what was observed in argon and krypton. Unfortunately, such experiments cannot be performed using our matrix-isolation system, as the cryostat cannot be cooled to a sufficiently low temperature to freeze a neon matrix. Additional work must be performed to understand the stabilization of the separated dimer as the thermodynamically favorable structure. Computational studies modelling the interaction between the $CO_2$ dimer anion and the matrix may provide insight into the stabilization and mechanism for formation of the $C_2O_4^-$ species. As discussed in Chapter 3, following deposition at 20K, additional peaks slightly shifted from the dimeric anion peaks at 1652.7 $cm^{-1}$ and 1856.9 $cm^{-1}$ peaks were observed and showed reversible temperature dependence in the range of 14K to 20K.

Only preliminary attempts to characterize these species have been carried out, and it may become clear with further work and analysis that additional equilibrium processes are occurring. These peaks may represent larger $(CO_2)_n^-$ clusters, which may provide additional insight regarding the connection between the gas phase and matrix isolated experiments.

## 4.7 Appendix

### 4.7.1 Peak Fitting

Obtaining the necessary qualitative data from the spectroscopic information available requires relating the intensity of the peaks corresponding to the species of interest with their concentration present in the matrix. This relations was achieved by relating the integrated area of the peaks with relative concentration. Because of conservation of mass, the population, and therefore the relative concentration, of two molecules in reversible unimolecular equilibrium, must sum to one:

$$\chi_1 + \chi_2 = 1 \tag{4.52}$$

The population is directly dependent on the integrated area of the peak intensity, $I_1$ or $I_2$. Population can be related to concentration by a scaling factor, $\sigma_1$ or $\sigma_2$, such that

$$\chi_1 = \frac{I_1}{\sigma_1} \tag{4.63}$$

as well as the corresponding equation for $A_2$. Substituting $\frac{I_1}{\sigma_1}$ for $\chi_1$ and $\frac{I_2}{\sigma_2}$ for $\chi_2$ in equation 4.12 and solving for $I_2$ gives the linear equation

$$I_2 = -\frac{\sigma_2}{\sigma_1} I_1 + \sigma_2 \tag{4.14}$$

At any given time or temperature, the intensities of the two peaks should follow this linear relationship. A plot of the integrated area of the 1652.7 $cm^{-1}$ peak, $I_1$, *versus* the integrated area of the 1856.9 $cm^{-1}$ peak, $I_2$, is made and shown in Figure 4.13, below. A line is fit to the data, and the scaling factors, $\sigma_1$ and $\sigma_2$, are calculated based upon equation 4.14, then using the relation between intensity and concentration, equation 4.13, the relative populations of the two species are calculated from the integrated intensity and the scaling factor.

When generating a linear fit, the Origin software only considers the error in the y-value, and not the error in the x-value, to produce the line of best fit. To find the scaling factors, two plots were generated to ensure that the error in both the x-value and y-value were properly considered. One plot was the integrated area of the 1657.0 $cm^{-1}$ as a function of the integrated area of the 1856.9 $cm^{-1}$, and the second plot was the 1856.9 $cm^{-1}$ peak as a function of the 1657.0 $cm^{-1}$ peak. The two sets of scaling factors generated from each plot were averaged, and the error associated with each was propagated using standard methods.

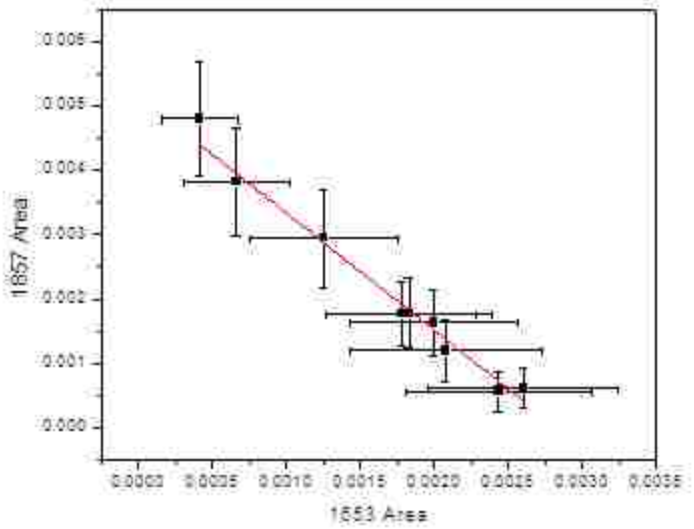


**Figure 4.13:** Plot of peak 1, $(CO_2)(CO_2^-)$ integrated area (1652.7 Area), *versus* peak 2, $C_2O_4^-$ integrated area (1857 Area), across various temperatures in the equilibrium temperature range. The relation shows a high linear dependence, with an $r^2$ value of 0.968.

The error in integrated peak area is determined based upon the noise in the spectrum. A region of the spectrum where the baseline remains flat for at least 150 points is isolated. The region is analyzed using the Statistics function, which is built into the Origin 8 software suite. The standard deviation of the flat region of the baseline is used as the noise (N). The error of the peak is determined by the equation

$$Error = S\sqrt{\frac{N}{S}} \tag{4.75}$$

where S is the signal, corresponding to the calculated integrated area of the peak.

### 4.7.2 Derivation and Explanation of Kinetic Fitting Equations

The derivation of the equations to fit the kinetic data is adapted from the derivation found in Chemical Kinetics and Dynamics by Steinfeld, Francisco, and Hase.[97]

The three equations used to fit the kinetic data were derived from the rate equations for a reversible, unimolecular reaction

$$A_1 \underset{k_r}{\overset{k_f}{\rightleftharpoons}} A_2 \tag{4.86}$$

Conservation of mass assumes that at a given time, the total concentration of the reactants and products must equal the initial concentration at time zero such that

$$[A_1]_0 + [A_2]_0 = [A_1] + [A_2] \tag{4.97}$$

and for this system, since the true concentration of the reactants and products in the matrix is unknown, these concentrations are taken to be relative concentrations, as described in the previous section. The differential equations from the reversible unimolecular reaction are

$$-\frac{d[A_1]}{dt} = k_f[A_1] - k_r[A_2] \tag{4.108}$$

and

$$-\frac{d[A_2]}{dt} = k_r[A_2] - k_f[A_1] \tag{4.119}$$

Solving the conservation of mass equation for $[A_2]$ yields the equation

$$[A_2] = [A_1]_0 + [A_2]_0 - [A_1] \tag{4.20}$$

and it can be inserted into the differential equation for the change in $[A_1]$ with respect to time to produce the equation

$$-\frac{d[A_1]}{dt} = k_f[A_1] - k_r([A_1]_0 + [A_2]_0 - [A_1]) \tag{4.121}$$

which can be rearranged to yield

$$-\frac{d[A_1]}{dt} = (k_r + k_f)\{\frac{-k_r([A_1]_0 + [A_2]_0)}{k_r + k_f} + [A_1]\} \tag{4.132}$$

A solution to this equation can be found by introducing a variable *m*, which is defined as

$$-m = \frac{-k_r([A_1]_0 + [A_2]_0)}{k_r + k_f} \tag{4.143}$$

so the equation can be rearranged and integrated

$$\int \frac{d[A_1]}{m - [A_1]} = (k_r + k_f) \int dt \tag{4.154}$$

and the solution to this integral yields the equation

$$\ln\left(\frac{k_f[A_1] - k_r[A_2]}{k_f[A_1]_0 - k_r[A_2]_0}\right) = -(k_r + k_f)(t - t_0) \tag{4.165}$$

If only $A_1$ is present at time zero, this equation simplifies to

$$\ln\left(\frac{k_f[A_1] - k_r[A_2]}{k_f[A_1]_0}\right) = -(k_r + k_f)t \tag{4.176}$$

which can be rearranged to

$$[A_1] = \frac{[A_1]_0}{k_r + k_f}[k_r - k_f e^{-(k_r + k_f)t}] \tag{4.187}$$

Finally, using conservation of mass, the above equation can be solved for $A_2$

$$[A_2] = \frac{k_f[A_1]_0}{k_r + k_f}[1 - e^{-(k_r + k_f)t}] \tag{4.198}$$

In this system, only one component is present at $t_0$ if the temperature of the matrix is initially held outside of the equilibrium temperature range, at which only one of $(CO_2)(CO_2^-)$ or $C_2O_4^-$ will be present. We assign $A_1$ to be the compound which is initially

present. Therefore, if the matrix is warmed from low temperature, so the initial form is $(CO_2)(CO_2^-)$, the equation for the reaction is defined as

$$(CO_2)(CO_2^-) \underset{k_r}{\overset{k_f}{\rightleftharpoons}} C_2O_4^- \tag{4.209}$$

and if the matrix is cooled from high temperature where $C_2O_4^-$ is the initial form, the equation for the reaction is defined as

$$C_2O_4^- \underset{k_r}{\overset{k_f}{\rightleftharpoons}} (CO_2)(CO_2^-) \tag{4.30}$$

so in both cases, only $A_1$ is present at $t_0$, allowing us to fit the simplified equations, which are only dependent on $k_r$, $k_f$, and t.

Due to experimental constraints, we introduced two modifications to equations 4.27 and 4.28. As the goal was to determine the temperature dependence of the rate constants, $k_r$ and $k_f$, the matrix would be warmed or cooled to an equilibrium temperature of interest from an initial temperature outside of the equilibrium range. Therefore, the assumption that only $A_1$ is present at time zero is not true, because there is a short time during which the matrix is warming or cooling to the specified equilibrium temperature that the second species will begin to grow in concentration. Additionally, there is a delay inherent with the time required to collect the first spectrum. Therefore we reintroduced $t_0$ as a variable to account for the time between the acquisition of the first data point and the true final time at which only $A_1$ is present in the system.

The second modification was replacing $[A_1]$ and $[A_2]$ in the original equations with ratios, $\frac{[A_1]}{[A_1]_0}$ and $\frac{[A_2]}{[A_1]_0}$. This ensured matrix loss did not contribute to a systematic error in our calculations and is consistent with our convention of using relative

concentrations as a means to relate integrated peak intensity from spectral data. Prior to warming or cooling to an equilibrium temperature, a spectrum of the matrix was collected with the equilibrium pushed entirely to the low or high temperature isomer. The relative concentration of the initial species, determined based on the method described in the Peak Fitting section, was always very close to one, but it accounted for small variations in signal strength throughout the day, and ensured each trial was internally consistent. The modified equations used to fit the data are

$$\frac{[A_1]}{[A_1]_0} = (\frac{k_f}{k_r + k_f})e^{-(k_r+k_f)(t-t_0)} \tag{4.211}$$

and

$$\frac{[A_2]}{[A_1]_0} = (\frac{k_f}{k_r + k_f})(1 - e^{-(k_f+k_r)(t-t_0)}) \tag{4.222}$$

The ratio, $\frac{[A_1]}{[A_1]_0}$ or $\frac{[A_2]}{[A_1]_0}$, is plotted on the y-axis against time on the x-axis, and the corresponding equation is used to fit the approximate exponential growth or decay. Three variables, $k_f$, sum, and $t_0$, are fit using the nonlinear fitting function built into the Origin software. Sum represents $k_f + k_r$, and $k_r$ is determined by subtracting the fit value for $k_f$. This method provided better results than attempting to fit four independent variables.

Individually, these equations each only make use of half of the available data, as they are dependent only on the concentration of one of the two peaks. A third equation was generated by dividing the other two fitting equations:

$$\frac{[A_2]}{[A_1]} = \frac{k_f(1 - e^{-(k_f+k_r)(t-t_0)})}{k_r + k_f e^{-(k_f+k_r)(t-t_0)}} \tag{4.233}$$

The ratio of the concentration is plotted as a function of time, allowing the relative concentrations of both species to be simultaneously used to calculate the rate constants of the system.

At equilibrium, the concentrations of the two species stop changing such that

$$\frac{d[A_1]}{dt} = \frac{-d[A_2]}{dt} = 0 \tag{4.244}$$

$$-k_f[A_1]_e + k_r[A_2]_e = 0 \tag{4.255}$$

so the forward and reverse rate constants at a given temperature can be used to calculated the equilibrium constant $K_{eq}$ at that temperature, as shown by the definition of the equilibrium constant

$$K_{eq} = \frac{[A_2]_e}{[A_1]_e} = \frac{k_r}{k_f} \tag{4.266}$$

The equilibrium constant, $K_{eq}$, is calculated at each temperature when finding a van't Hoff plot for the equilibrium system, so a fully independent method is available to check which of the three equations yield the most accurate ratio of $k_r$ and $k_f$ for each experiment performed, as well as a temperature independent method for testing the accuracy of the van't Hoff analysis.

### 4.7.3 Temperature Dependent Rate Constants

Tables 4.1 – 4.6 show an example of the fit values and temperature dependent rate constants calculated using three kinetic rate equations described in the body of the text, and in the previous section. "Up" refers to warming the matrix from 10K to the stated temperature, and "Down" refers to cooling the matrix from 25K to the stated temperature. Not all temperature are shown for each direction due to equilibration either occurring too

fast, or there not being a significant enough change in the peak size to obtain meaningful data.

**Table 4.1 Kinetic Data for Equation $\frac{[A_2]}{[A_1]} = \frac{k_f(1-e^{-(k_f+k_r)(t-t_0)})}{k_r+k_f e^{-(k_f+k_r)(t-t_0)}}$ cooling from 25K**

| $[A_2]/[A_1]$ DOWN | $\frac{[(CO_2)(CO_2^-)]}{[C_2O_4^-]}$ | | | | | | |
|---|---|---|---|---|---|---|---|
| **Temp** | **$T_0$** | **SUM** | **SUM error** | **$K_r$** | **$K_r$ error** | **$K_f$** | **$K_f$ error** |
| **12** | -4.86719 | 0.0265 | 0.00109 | 0.00183 | 0.001961787 | 0.02467 | 0.000707 |
| **14** | -9.74704 | 0.0269 | 0.00124 | 0.00236 | 0.002504226 | 0.02454 | 0.000838 |
| **18** | -5.31264 | 0.0307 | 0.000844 | 0.0031 | 0.003154807 | 0.0276 | 0.000586 |
| **19** | -4.63719 | 0.03598 | 0.00124 | 0.00636 | 0.006407478 | 0.02962 | 0.000779 |
| **20** | -4.31582 | 0.04822 | 0.00215 | 0.01693 | 0.016965698 | 0.03129 | 0.0011 |
| **21** | -6.35719 | 0.06277 | 0.00471 | 0.03936 | 0.039389339 | 0.02341 | 0.00152 |
| **22** | -4.4871 | 0.17581 | 0.06009 | 0.14812 | 0.148386544 | 0.02769 | 0.00889 |

**Table 4.2 Kinetic Data for Equation $\frac{[A_1]}{[A_1]_0} = (\frac{k_f}{k_r+k_f})e^{-(k_r+k_f)(t-t_0)}$ cooling from 25K**

| $[A_1]/[A_1]_0$ DOWN | $\frac{[C_2O_4^-]}{[C_2O_4^-]_0}$ | | | | | | |
|---|---|---|---|---|---|---|---|
| **Temp** | **$T_0$** | **SUM** | **SUM error** | **$K_r$** | **$K_r$ error** | **$K_f$** | **$K_f$ error** |
| **12** | -5.40074 | 0.02913 | 0.00101 | 0.00222 | 0.00030212 | 0.02691 | 0.001054 |
| **14** | -9.58104 | 0.03004 | 0.00137 | 0.00296 | 0.000376 | 0.02708 | 0.001421 |
| **18** | -3.33168 | 0.03071 | 0.000986 | 0.00333 | 0.000285493 | 0.02738 | 0.001027 |
| **19** | -3.5824 | 0.03415 | 0.00127 | 0.00621 | 0.000469835 | 0.02794 | 0.001354 |
| **20** | -3.1347 | 0.04443 | 0.00176 | 0.01593 | 0.000873326 | 0.0285 | 0.001965 |
| **21** | -6.13317 | 0.06515 | 0.00532 | 0.04072 | 0.00354 | 0.02443 | 0.00639 |
| **22** | -3.73754 | 0.17584 | 0.06497 | 0.14575 | 0.05427 | 0.03009 | 0.084654 |

**Table 4.3 Kinetic Data for Equation $\frac{[A_2]}{[A_1]_0} = (\frac{k_f}{k_r+k_f})(1 - e^{-(k_f+k_r)(t-t_0)})$ cooling from 25K**

| $[A_2]/[A_1]_0$ DOWN | $\frac{[(CO_2)(CO_2^-)]}{[C_2O_4^-]_0}$ | | | | | | |
|---|---|---|---|---|---|---|---|
| **Temp** | **$T_0$** | **SUM** | **SUM error** | **$K_r$** | **$K_r$ error** | **$K_f$** | **$K_f$ error** |
| **12** | -5.37384 | 0.02648 | 0.00162 | 0.0038 | 0.00077679 | 0.02268 | 0.001797 |
| **14** | -11.4492 | 0.02403 | 0.00155 | 0.00274 | 0.000623233 | 0.02129 | 0.001671 |
| **18** | -5.40449 | 0.02954 | 0.00194 | 0.000787 | 0.000347 | 0.028753 | 0.001971 |
| **19** | -4.23759 | 0.03715 | 0.00176 | 0.0047 | 0.0006924 | 0.03245 | 0.001891 |
| **20** | -3.9977 | 0.05139 | 0.00329 | 0.01674 | 0.0016 | 0.03465 | 0.003658 |
| **21** | -6.439 | 0.06243 | 0.00592 | 0.03924 | 0.00402 | 0.02319 | 0.007156 |
| **22** | -4.49922 | 0.18074 | 0.07526 | 0.15276 | 0.06396 | 0.02798 | 0.098767 |

**Table 4.4 Kinetic Data for Equation $\frac{[A_2]}{[A_1]} = \frac{k_f(1-e^{-(k_f+k_r)(t-t_0)})}{k_r+k_f e^{-(k_f+k_r)(t-t_0)}}$ warming from 10K**

| $[A_2]/[A_1]$ UP | $\frac{[C_2O_4^-]}{[(CO_2)(CO_2^-)]}$ | | | | | | |
|---|---|---|---|---|---|---|---|
| **Temp** | **$T_0$** | **SUM** | **SUM error** | **$K_f$** | **$K_f$ error** | **$K_r$** | **$K_r$ error** |
| **20** | -6.09313 | 0.04574 | 0.00276 | 0.03078 | 0.002856276 | 0.01496 | 0.000735 |
| **20.5** | -10.0508 | 0.06482 | 0.00368 | 0.03336 | 0.003993107 | 0.03146 | 0.00155 |
| **21** | -3.05993 | 0.09407 | 0.00349 | 0.03552 | 0.003950013 | 0.05855 | 0.00185 |
| **21.5** | -3.2359 | 0.1616 | 0.01004 | 0.03984 | 0.012227919 | 0.12176 | 0.00698 |

**Table 4.5 Kinetic Data for Equation $\frac{[A_1]}{[A_1]_0} = (\frac{k_f}{k_r+k_f})e^{-(k_r+k_f)(t-t_0)}$ warming from 10K**

| $[A_1]/[A_1]_0$ UP | $\frac{[(CO_2)(CO_2^-)]}{[(CO_2)(CO_2^-)]_0}$ | | | | | | |
|---|---|---|---|---|---|---|---|
| **Temp** | **$T_0$** | **SUM** | **SUM error** | **$K_f$** | **$K_f$ error** | **$K_r$** | **$K_r$ error** |
| **20** | -2.84664 | 0.5323 | 0.00591 | 0.49538 | 0.007344229 | 0.03692 | 0.00436 |
| **20.5** | -12.1155 | 0.05493 | 0.00504 | 0.02804 | 0.005760703 | 0.02689 | 0.00279 |
| **21** | -2.84396 | 0.09942 | 0.00561 | 0.06266 | 0.006129682 | 0.03676 | 0.00247 |
| **21.5** | -3.80491 | 0.15441 | 0.01679 | 0.11774 | 0.017395591 | 0.03667 | 0.00455 |

**Table 4.6 Kinetic Data for Equation $\frac{[A_2]}{[A_1]_0} = (\frac{k_f}{k_r+k_f})(1 - e^{-(k_f+k_r)(t-t_0)})$ warming from 10K**

| $[A_2]/[A_1]_0$ UP | $\frac{[C_2O_4^-]}{[(CO_2)(CO_2^-)]_0}$ | | | | | | |
|---|---|---|---|---|---|---|---|
| **Temp** | **$T_0$** | **SUM** | **SUM error** | **$K_f$** | **$K_f$ error** | **$K_r$** | **$K_r$ error** |
| **20** | -6.507 | 0.04385 | 0.00321 | 0.01478 | 0.003972367 | 0.02907 | 0.00234 |
| **20.5** | -9.09469 | 0.07324 | 0.00547 | 0.03413 | 0.006337263 | 0.03911 | 0.0032 |
| **21** | -3.26821 | 0.09136 | 0.0042 | 0.05567 | 0.004682403 | 0.03569 | 0.00207 |
| **21.5** | -3.16617 | 0.15985 | 0.00671 | 0.11814 | 0.007030939 | 0.04171 | 0.0021 |

With the calculation of $k_r$ and $k_f$, a van't Hoff plot can be generated because $K_{eq} = \frac{k_r}{k_f}$. Therefore, a method is available to test the best fitting method, because the van't Hoff plot generated from each kinetic fit can be compared with a "known" van't Hoff plot generated from the analysis of the equilibrated spectra at each temperature. Table 4.7 shows a comparison of calculated values for change in enthalpy and entropy for each kinetic fitting method. Most van't Hoff plots generated by the equilibrium spectra yielded a change in standard enthalpy ranging from 3500 J $mol^{-1}$ to 3800 J $mol^{-1}$ and a

change in standard entropy ranging from 170 J $mol^{-1}$ $K^{-1}$ to 180 J $mol^{-1}$ $K^{-1}$. It is expected that the true change in standard enthalpy and entropy of reaction falls somewhere in those ranges, so the best fitting method appears to be using the equation $\frac{[A_2]}{[A_1]} = \frac{k_f(1-e^{-(k_f+k_r)(t-t_0)})}{k_r+k_f e^{-(k_f+k_r)(t-t_0)}}$ to fit data from cooling the matrix from 25K down to an equilibrium temperature. It is not surprising that the "Down" data provides more accurate data as the temperature range over which that method can be used is larger than the "Up" method. Using the "Down" method, almost the full equilibrium range from 19K to 22K can be tracked, but with the "Up" method, only a 1.5K range can be studied due small changes in peak intensities at low temperatures and fast equilibration at high temperatures.

**Table 4.7 Thermodynamic Constants Generated from Kinetic Rate Constants***

| Method | ΔH (J $mol^{-1}$) | ΔH Error | ΔS (J $mol^{-1}$ $K^{-1}$) | ΔS Error |
|---|---|---|---|---|
| **$[A_2]/[A_1]$ DOWN** | 3710 | 250 | 181 | 12 |
| **$[A_1]/[A_1]_0$ DOWN** | 3080 | 190 | 149 | 10 |
| **$[A_2]/[A_1]_0$ DOWN** | 3970 | 135 | 193 | 6.8 |
| **$[A_2]/[A_1]$ UP** | 4300 | 93 | 208 | 4.5 |

* Only one set of "up" data is shown, as the other two methods did not produce meaningful thermodynamic values

### 4.7.4 Temperature Dependence of $CO_2^-$

The peak located at 1657 $cm^{-1}$, which has been previously assigned to $CO_2^-$ by Andrews, reversibly responds with temperature in a manner similar to the $(CO_2)(CO_2^-)$ peak at 1652.7 $cm^{-1}$, and it initially appeared that it may also be participating in the equilibrium process. Figure 4.14 shows the normalized integrated areas of the peaks

corresponding to $(CO_2)(CO_2^-)$, $CO_2^-$, and $C_2O_4^-$. One possibility is that the peaks at 1652.7 $cm^{-1}$ and 1657.0 $cm^{-1}$ arise from a single species. If this were the case, the normalized integrated peak intensities should track directly with each other as a function of temperature, and it is clear in Figure 4.14 that the two peaks are not directly correlated. If both species were involved in the same equilibrium process, it would be expected that they would track directly with each other.

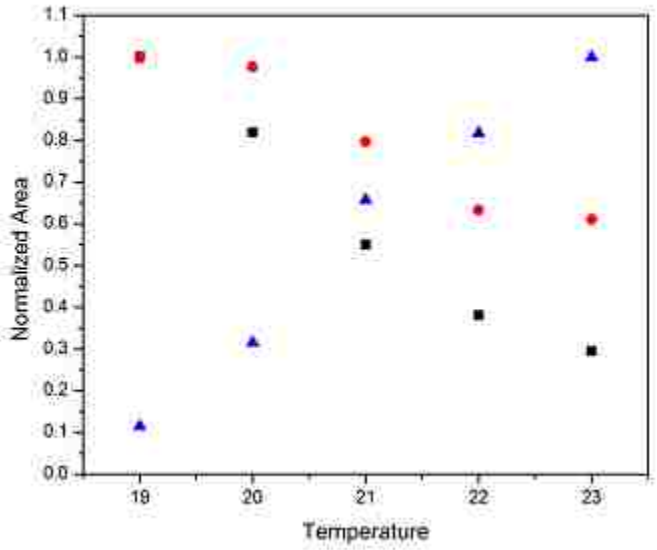


**Figure 4.14:** Normalized area of 1652.7 $cm^{-1}$ peak (Black Squares), 1657.0 $cm^{-1}$ (Red Circles), and 1856.9 $cm^{-1}$ (Blue Triangles) as a function of temperature. Note that the areas of the 1652.7 and 1657.0 $cm^{-1}$ peaks do not change at the same rate.

Since $CO_2^-$ is not involved in the same equilibrium process as $(CO_2)(CO_2^-)$, it is possible that it is involved in a separate independent equilibrium process with $C_2O_4^-$. This can be tested by following the same procedure for the van't Hoff analysis discussed in the main body of the text. Coefficients are determined to convert area to relative concentration by plotting the areas of the 1657.0 $cm^{-1}$ and 1856.9 $cm^{-1}$ peaks as a function of one another. The coefficients are used to convert the peak areas to relative

concentration, which is then used to construct the van't Hoff plot shown in Figure 4.15. Figure 4.15 (A) shows a van't Hoff plot generated from the relative concentrations of $(CO_2)(CO_2^-)$ and $C_2O_4^-$, and Figure 4.15 (B) shows the van't Hoff plot generated from relative concentrations of the 1657.0 $cm^{-1}$ $(CO_2^-)$ peak and $C_2O_4^-$. Figure 4.13 (A) shows the linear behavior expected of an equilibrium process, while the plot generated using the 1657 $cm^{-1}$ peak shows clear curvature. At this time it remains unclear why the $CO_2^-$ peak responds reversibly with temperature. Attempts have been made to locate a peak which gains intensity in conjunction with the loss of intensity of the 1657.0 $cm^{-1}$ band, but no such peak has been identified.

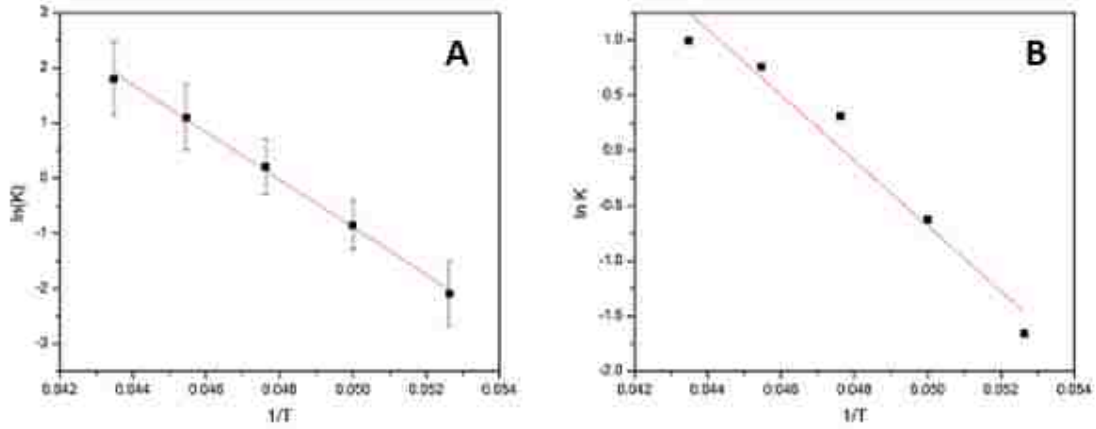


**Figure 4.15:** (A) van't Hoff plot generated using the relative concentrations of $(CO_2)(CO_2^-)$ and $C_2O_4^-$. (B) van't Hoff plot generated using the relative concentrations of $CO_2^-$ and $C_2O_4^-$. Note the clear curvature in the points not present in the plot on the left.

### 4.7.5 Other Relevant Spectroscopic Signatures

The antisymmetric stretching mode of $C_2O_4^-$ which appears at 1856.9 $cm^{-1}$ is significantly more intense than the symmetric stretch, appearing at 1185.3 $cm^{-1}$, so the integrated area of the 1856.9 $cm^{-1}$ peak has been used in calculations to track the concentration of $C_2O_4^-$ as a function of temperature. The larger signal to noise ratio serves to limit error in the calculations. Figure 4.16 shows a comparison of the

normalized integrated areas of the two peaks as a function of temperature. The direct tracking of the intensity of the two peaks with temperature shows that they arise from a single species.

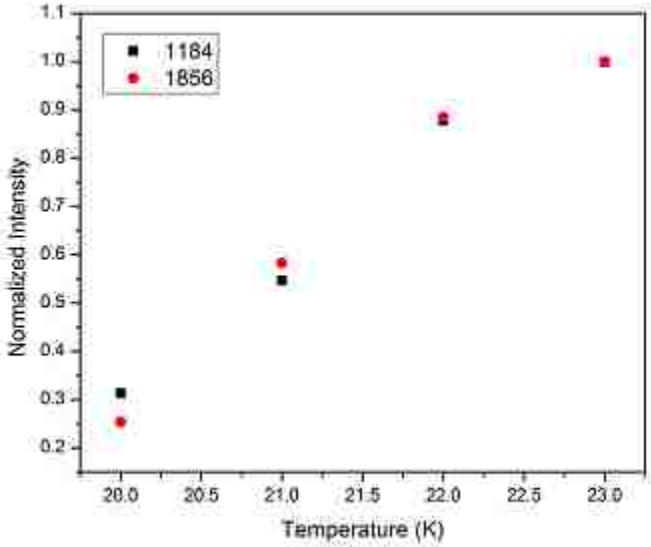


**Figure 4.16:** Comparison of the normalized integrated area of the 1185.3 $cm^{-1}$ and 1856.9 $cm^{-1}$, assigned to the symmetric and antisymmetric stretching mode of $C_2O_4^-$, as a function of temperature. The close tracking with temperature indicates peaks do in fact arise from a single species.

In the low temperature separated species, $(CO_2)(CO_2^-)$, the peak appears at 1652.7 $cm^{-1}$, which is shifted approximately 5 $cm^{-1}$ from the monomer anion $CO_2^-$, appearing at 1657.0 $cm^{-1}$. This small shift is due to perturbation by a closely associated neutral $CO_2$ molecule. It would be expected that the neutral $CO_2$ molecule in the dimer would be perturbed by the anion, and therefore its IR signal should be shifted from neutral, isolated $CO_2$. One would expect this peak to have the same temperature dependence as the peak at 1652.7 $cm^{-1}$, and could be used to track the equilibrium process. Unfortunately, in a 0.5% $CO_2$ doped matrix, the peak associated with the antisymmetric stretching mode of neutral $CO_2$ is intense enough to saturate the IR detector, and is also quite broad, so analysis of

this region of the spectrum is difficult. Two shoulder peaks on the neutral $CO_2$ peak which appear to track with temperature in the same manner as the 1652.7 $cm^{-1}$ peak have been identified. The shoulder peaks of interested are blue shifted from the fundamental antisymmetric stretching mode of $CO_2$ by 8 $cm^{-1}$ and 10 $cm^{-1}$, but our analysis has been unable to definitively confirm that one or both peaks can be assigned to $(CO_2)(CO_2^-)$.

# Chapter 5

## The Effect of Matrix-Deposition Temperature on the Formation of Matrix-Isolated Copper Carbonyl Anions

### 5.1 Abstract

The formation of matrix-isolated copper carbonyl anions shows a strong dependence on both concentration of CO in the matrix and the deposition temperature of the matrix. A series of experiments were performed in which the CO concentration in the matrix was held constant at 0.02% while varying the deposition temperature from 14K to 24K, clearly showing the direct effect of deposition temperature on copper carbonyl formation. As the deposition temperature was raised, the distribution of $CuCO^-$, $Cu(CO)_2^-$, and $Cu(CO)_3^-$ changed, favoring the formation of more highly coordinated $Cu(CO)_3^-$ and solvation complexes, $[Cu(CO)_3 \cdot nCO]^-$ at higher temperatures. Following 14K deposition, only a single small peak corresponding to $CuCO^-$ was observed, though deposition at 22K and 24K yield large peaks corresponding to $Cu(CO)_3^-$ and diminished amounts of the other two anionic carbonyl complexes. The changes in distribution upon deposition and differences in behavior following annealing of the matrix provide insights into the formation mechanism of the matrix-isolated copper carbonyl species.

### 5.2 Introduction

The deposition temperature of the matrix is an important variable in the formation of matrix isolated species. A previous publication by this group showed that a 2% CO doped argon matrix and a 0.02% CO doped argon matrix co-deposited with $Cu^-$ and $Ar^+$ at 10K and 20K, respectively, yields qualitatively similar distributions of anionic copper carbonyls upon deposition.[40] This is a result of more efficient freezing of the matrix at

10K, resulting in faster trapping of isolated species at 10K compared to 20K. It is understood that matrix isolated complexes form upon deposition as the matrix gas and dopants cool from room temperature.[3, 42] The surface of the matrix can be understood in terms of a transient mobile layer in which diffusion and reactions can occur on the surface of the matrix. Ozin and Moskovits suggested a mechanism for the formation of matrix-isolated neutral copper carbonyls in which surface reactions result in the stepwise building up of CO ligands on the copper center.[42] The formation of anionic copper carbonyls should closely resemble the neutral species, and in the transient layer $Cu^-$ and a CO molecule form $CuCO^-$, and additional CO molecules can then undergo subsequent additions to form larger anionic copper carbonyl species. Once the atoms and molecules are fully cooled, they become trapped in the matrix and can presumably no longer undergo reactions. Increasing the efficiency of cooling the matrix should reduce the time deposited species spend in this transient layer before they are immobilized in the matrix. At 20K, this transient diffusion process persists longer than at 10K, meaning that a lower concentration of CO is required to be present in the matrix to form comparable amounts of copper carbonyl anions. A 100 fold increase in CO concentration is required to make up for the 10K difference in deposition temperature.[43] In this chapter, results of a deposition temperature study of copper carbonyl anion formation will be presented. Changes in both the intensity and distribution of bands were observed, as well as interesting behavior upon annealing that depended upon the original deposition temperature.

## 5.3 Experimental Methods

All experiments presented in this chapter were carried out using the original instrument configuration without mass selection of the counter ion. Each matrix was generated and processed under identical conditions except for the deposition temperature. All matrices were 0.02% CO-doped argon co-deposited with a 4 nA beam of $Cu^-$ balanced with $Ar^+$ for a period of four hours. Deposition temperatures ranged from 14K to 24K in 2K increments. A spectrum was collected following deposition, and then the matrix was annealed to 30K for a period of 15 minutes and cooled back to 10K. Another spectrum was collected to observe changes induced by annealing. The matrix was then irradiated with a 470 nm LED for five minutes, and another spectrum was collected. Finally, the matrix was annealed to 30K for a second time, cooled to 10K, and a final spectrum was collected. The emission spectrum of the LED is shown in Chapter 2, Figure 2.9. The experiments were carried out under darkened conditions (lab lights, ion gauges, and RGA off) to ensure ambient light did not trigger photodetachment events.

## 5.4 Results

For reference, a list of known anionic and neutral copper carbonyl absorbances is provided in Table 5.1. Comparisons of three of the four spectra collected for each deposition temperature are shown in Figures 5.1-5.3. The fourth set of spectra, annealing following irradiation of the matrix, is provided in the Appendix.

**Table 5.1 Vibrational Band Assignments for Anionic and Neutral Copper Carbonyls in Argon Matrices***

| Species | Assignment ($cm^{-1}$) | Ref. | Species | Assignment ($cm^{-1}$) | Ref. |
|---|---|---|---|---|---|
| **$CuCO^-$** | 1733.5 | a | CuCO | 2007.8 | a,b |
| | | | | 2009.8 | a,b |
| **$Cu(CO)_2^-$** | 1780.7 | a | $Cu(CO)_2$ | 1890.8 | a,b |
| **$Cu(CO)_3^-$** | 1823.4 | c | $Cu(CO)_3$ | 1975.5 | a,b |
| | 1825.1 | c | | 1977.4 | c |
| | 1829.9 | b | | 1981.8 | c |
| | | | | 1983.2 | a |
| | | | | 1985.9 | a,b |

*Additional site peaks and $[Cu(CO)_3 \cdot nCO]^-$ peaks have been discussed and assigned in refs 15 and 40. A) ref 15 b) ref 40 c) ref 42

### 5.4.1 Deposition Spectra

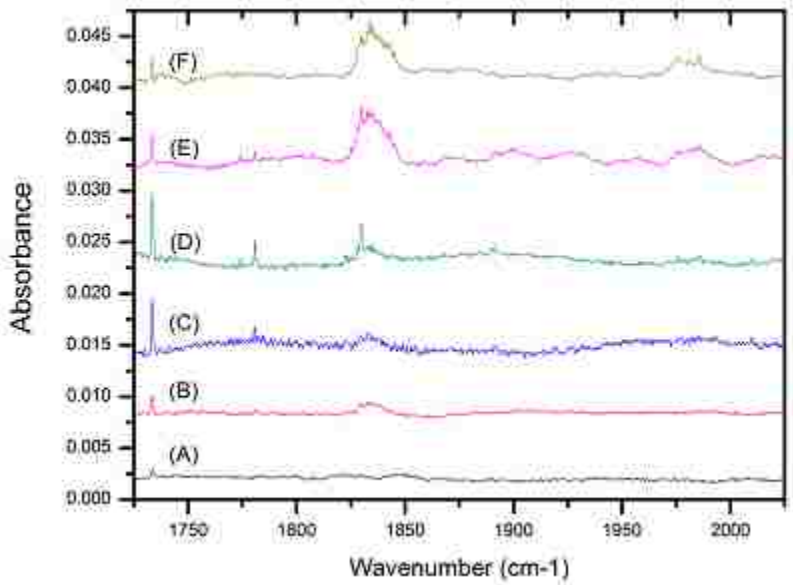


**Figure 5.1:** Temperature-dependent deposition infrared spectra of the anionic and neutral copper carbonyl region of the spectra. Each matrix contained 0.02% CO and was deposited under identical conditions except for temperature. Spectra A – F correspond to 14, 16, 18, 20, 22, and 24K deposition.

Spectra taken following deposition of the matrix across the range of temperatures are shown in Figure 5.1. The matrix was deposited at the noted temperature and then cooled to 10K for collection of the deposition spectrum. Upon deposition at 14K, a single

small peak at 1733 $cm^{-1}$, corresponding to $CuCO^-$ was observed. As the deposition temperature was increased to 20K, the intensity of the $CuCO^-$ peak increased as well. At 22K, the $CuCO^-$ intensity decreased compared to the as deposited 20K spectrum, and decreased further upon deposition at 24K. No $Cu(CO)_2^-$ is observed upon deposition at 14K, however following deposition at 16K, a small peak assigned to $Cu(CO)_2^-$ is present at 1780 $cm^{-1}$. The intensity of the peak increased as deposition temperature was warmed to 18K and 20K, and at 20K, an additional peak at 1774 $cm^{-1}$ was observed, assigned to a site peak of $Cu(CO)_2^-$. The intensity of the peak at 1780 $cm^{-1}$ begins to decrease upon deposition at 22K, but the intensity of the site peak remains approximately the same. No anionic $Cu(CO)_2^-$ signal was present upon deposition at 24K.

A broad feature located from ~1825 $cm^{-1}$ to 1850 $cm^{-1}$ was present at all temperatures above 14K. This region contained peaks assigned to $Cu(CO)_3^-$, including a particularly sharp peak at 1829 $cm^{-1}$. The broad feature is assigned to $[Cu(CO)_3 \cdot n(CO)]^-$, the copper tricarbonyl anion solvated by an unspecified number of neutral CO molecules.[40] The intensity of the $Cu(CO)_3^-$ bands increased with increasing temperature from 16K until it reaches a maximum at 22K. The intensity appeared approximately the equivalent following 22K and 24K deposition. In addition to the anionic copper carbonyls, weak bands assigned to neutral copper carbonyls were observed at some temperatures. Two small peaks were observed following 18K and 20K deposition at 1891 $cm^{-1}$ and 2010 $cm^{-1}$, assigned to the neutral species $Cu(CO)_2$ and CuCO, respectively. Neutral $Cu(CO)_3$, the broad feature around 1980 $cm^{-1}$, was present following 20K deposition, and increased in intensity after 22K and 24K deposition.

### 5.4.2 Annealing Behavior

Infrared spectra obtained following annealing of the different matrices to 30K for 15 minutes are shown in Figure 5.2. A corresponding set of difference spectra highlighting the changes between deposition and annealing are shown in Figure 5.5 in the Appendix. Some changes were observed irrespective of original deposition temperature, though others appeared to have dependence on the temperature at which the matrix was deposited. At all deposition temperatures, the intensity of the neutral copper carbonyl bands were observed to grow to some degree. The neutral copper di- and tri-carbonyl increased in intensity in all spectra, and the neutral copper monocarbonyl grew in the matrices deposited at 18K and 20K.

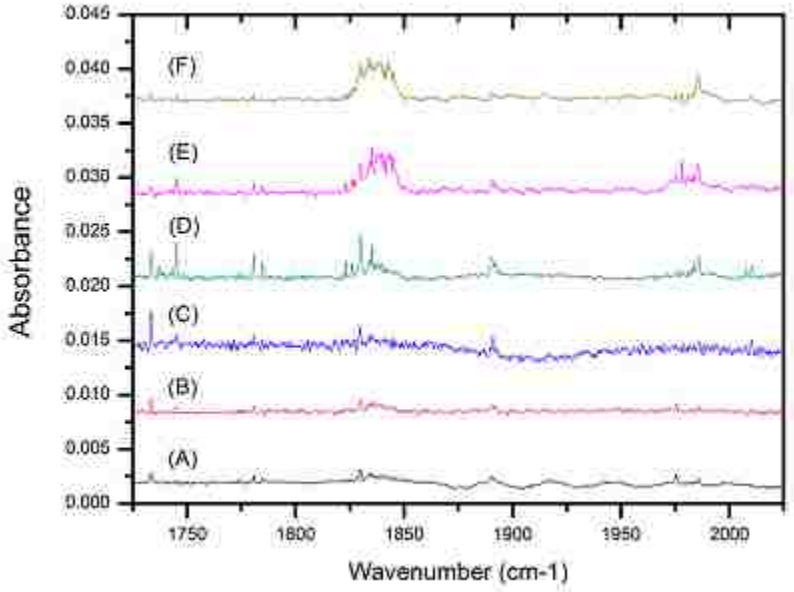


**Figure 5.2:** Infrared spectra obtained after annealing directly to 30K for 15 minutes following deposition spectrum. Spectra A – F correspond to deposition temperatures of 14, 16, 18, 20, 22, and 24K.

In the 14K spectrum, annealing resulted in the formation of both anionic and neutral copper carbonyls. Peaks corresponding to $Cu(CO)_2^-$, $Cu(CO)_3^-$, and their neutral

analogues were observed, but these species were not present initially upon deposition. No changes were observed in either $CuCO^-$ or neutral CuCO. At all deposition temperatures except 14K, the anionic copper carbonyls were observed to undergo some level of conversion to site peaks, though the degree to which this conversion occurred, and the complexity of the resulting features, was dependent upon the deposition temperature of the matrix. Most notable was the appearance of the $CuCO^-$ site peak at 1745 $cm^{-1}$. As deposition temperature increased, the peak at 1733 $cm^{-1}$ converted more completely to 1745 $cm^{-1}$. This 1745 $cm^{-1}$ peak has only been observed for samples deposited in this temperature range, and then annealed to 30K. It is assumed to correspond to a structural or electronic isomer of $CuCO^-$ that can only exist in the matrix environment.[43]

### 5.4.3 Photolysis

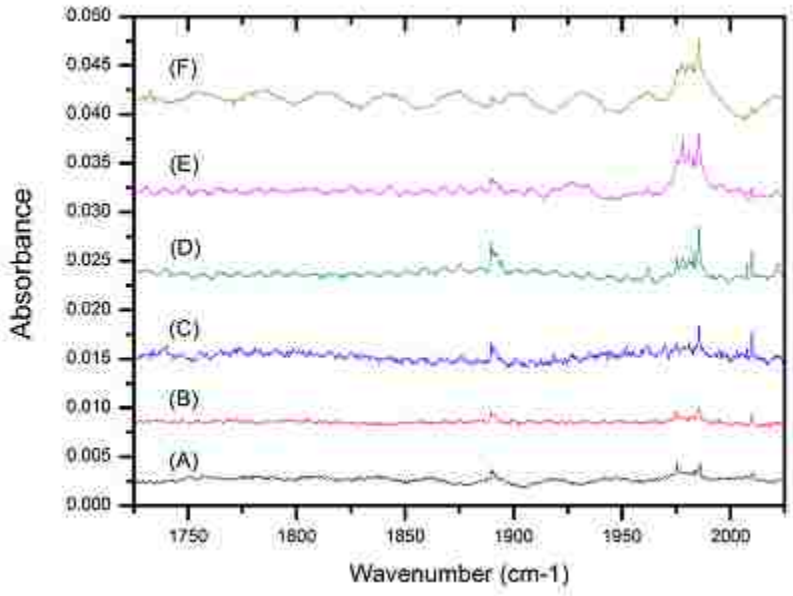


**Figure 5.3:** Infrared spectra obtained following irradiation of the matrix with a 470 nm LED light source for five minutes, resulting in the neutralization of anionic copper carbonyls and the subsequent growth of the corresponding neutral peaks. Spectra A – F correspond to original deposition temperatures of 14, 16, 18, 20, 22, and 24K.

Irradiation of the matrix with a 470 nm LED light source for five minutes at 10K results in the neutralization of the anionic copper carbonyls by photodetachment of the anionic electron. In all spectra, regardless of deposition temperature, the anionic peaks present before irradiation were depleted, and growth was observed in the corresponding neutral peaks. The relative distributions of copper mono-, di-, and tricarbonyl neutrals were preserved. The 22K and 24K spectra were dominated by the presence of the copper tricarbonyl neutral, consistent with the large amount of anionic copper carbonyl present before irradiation, and the minimal amount of the anionic copper mono- and dicarbonyls. A second 30K annealing step was performed following photolysis. The behavior of the neutral copper carbonyls in this step were consistent with previously observed behavior, including increased intensity in the CuCO and $Cu(CO)_2$ peaks and slight changes in the appearance and sharpness of the $Cu(CO)_3$ bands.[41, 43] Figure 5.4 in the Appendix shows the spectra obtained following this second annealing step.

**5.5 Discussion**

Analysis of the differences in the temperature dependent spectra, specifically those obtained immediately following deposition and after the first annealing step, Figures 5.1 and 5.2, provides interesting insight into the formation mechanism of matrix isolated copper carbonyl complexes. The strong correlation between deposition temperature and intensity of bands corresponding to copper carbonyl species confirms that matrix isolated complexes form in the time period between initial deposition and when the molecules are fully cooled and trapped in the matrix.

The appearance of a single peak at 1733 $cm^{-1}$ assigned to $CuCO^-$ following deposition at 14K appears to confirm the formation mechanism proposed by Ozin and Moskovits[42] that matrix isolated copper carbonyls form *via* a stepwise mechanism, in which CO molecules react in succession with the copper anion, first forming the monocarbonyl, and then the di- and tri-carbonyl through reaction with additional CO molecules. Longer diffusion periods at higher temperatures naturally allow more highly coordinated complexes to be formed. Based on this model, there should be deposition temperature resulting in the dicarbonyl anion peak being larger than the monocarbonyl. The electronic structure of the dicarbonyl anion is predicted to be a triplet, while both the mono- and tricarbonyl anions are singlets.[15] The difference in electronic structure may result in the lack of stability of the dicarbonyl anion. Also of note is the increased production of the dicarbonyl neutral species upon initial annealing at 30K. This may further suggest the instability of the dicarbonyl anion.

The behavior at 22K and 24K is particularly interesting, as the intensity of the copper mono- and dicarbonyl bands decrease with respect to lower temperature deposition. This behavior suggests that at the high deposition temperatures, $Cu^-$ becomes the limiting reagent, as the fast diffusion layer persists long enough to ensure that all $Cu^-$ react with at least a single CO molecule. As all anionic copper centers are at least partially saturated following 22K deposition, additional time in the fast diffusion layer results in the formation of larger quantities of $Cu(CO)_3^-$ and solvation complexes, $[Cu(CO)_3 \bullet n(CO)]^-$ at the expense of $CuCO^-$ and $Cu(CO)_2^-$. This behavior is consistent with the annealing spectra for the 22K and 24K deposition, as smaller amounts of neutral

$CuCO$ and $CuCO_2$ were created upon annealing compared to what was observed in the matrices deposited at lower temperatures.

The formation of larger anionic copper carbonyl complexes *via* stepwise addition of CO molecules cannot be used to explain the annealing behavior of the matrix deposited at 14K. Following deposition at higher temperatures, annealing resulted in the formation of new anionic site peaks, but they can be correlated with the depletion of anionic peaks observed upon deposition. Andrews reported growth of $Cu(CO)_2^-$ and $Cu(CO)_3^-$ following annealing of an argon matrix in his laser ablation studies, but these peaks were observed to grow at the expense of $CuCO^-$.[15] In the 14K matrix, annealing to 30K resulted in the formation of $Cu(CO)_2^-$ and $Cu(CO)_3^-$, which were not observed in the initial deposition spectrum. If the stepwise mechanism were the only method for formation of these complexes, it would be expected that the formation of the more highly coordinated compounds at 30K would come at the expense of existing $CuCO^-$, but the intensity of the $CuCO^-$ peak did not change upon annealing. It is possible that there is an attractive force between $Cu^-$ and CO in the fast diffusion layer, but at 14K the species are frozen out before they can form complexes, which could result in an increase in concentration of CO molecules in the matrix surrounding free $Cu^-$ ions. Upon annealing, changes in the grain boundaries and crystal structure of the matrix could move $Cu^-$ and CO molecules in close enough proximity to react, and the heat given off by the reaction causes local heating of the matrix, allowing a second or third CO molecule to diffuse and react.

It is also interesting to examine the degree of which conversion to site peaks occurs upon annealing as a function of initial deposition temperature. Previous work in

the Moore group characterized the site peaks formed upon annealing as a form of activated transient complex.[43] The clearest example is the appearance of the site peak at 1745 $cm^{-1}$ upon annealing to 30K at the expense of the $CuCO^-$ peak at 1733 $cm^{-1}$. Upon irradiation, a peak is observed at 2022 $cm^{-1}$ only when the 1745 $cm^{-1}$ peak was present, and upon annealing following the photodetachment step, the 2022 $cm^{-1}$ converted to CuCO at 2007 $cm^{-1}$ and 2010 $cm^{-1}$. The peak at 2022 $cm^{-1}$ was attributed to the neutral analogue of the anionic matrix-only isomer of $CuCO^-$ appearing at 1745 $cm^{-1}$.[43] It is clear that the formation of the transient peak at 1745 $cm^{-1}$ is dependent upon the deposition temperature of the matrix. At 20K deposition and higher, upon annealing the intensity of the 1745 $cm^{-1}$ peak was comparable to or greater than the intensity of the remaining 1733 $cm^{-1}$ peak, but below 20K deposition the conversion is greatly suppressed. The matrix is partially annealed when deposited at higher temperatures, as evidenced by decreased light scattering in spectra of matrices deposited at 20K compared to 10K, suggesting the matrix is more polycrystalline. It is possible that matrix deposited under these higher temperature conditions can trap $CuCO^-$ in an environment conducive to the formation of the activated $CuCO^-$ isomer appearing at 1745 $cm^{-1}$. Interestingly, the 1745 $cm^{-1}$ peak is not observed following 30K deposition, suggesting the property of the matrix which facilitates the conversion is only present when the matrix is deposited near 20K.

## 5.6 Appendix

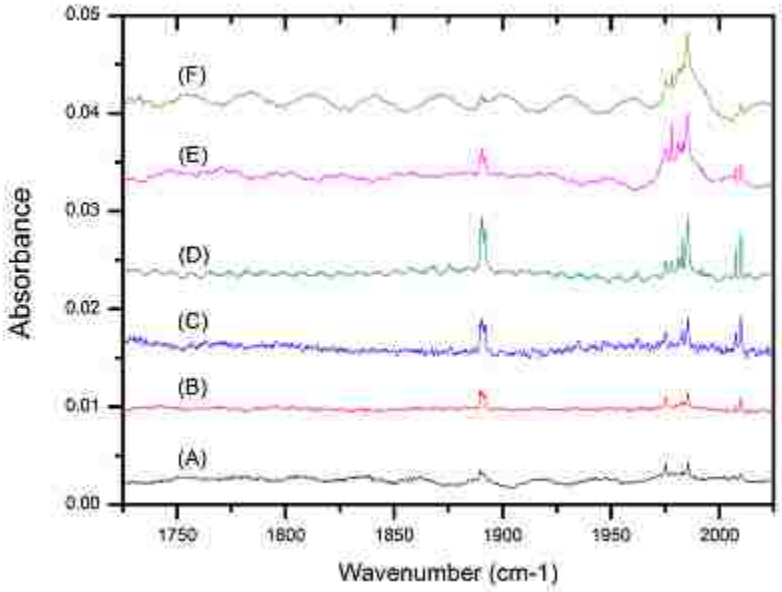


**Figure 5.4:** Infrared spectra obtained following annealing to 30K after the photolysis step was performed. Behavior of the neutral copper carbonyls as expected based on previous results, and is consistent across all deposition temperatures. The peaks corresponding to CuCO and $Cu(CO)_2$ sharpen and appear to gain intensity, and sharpening and slight changes in peak shape occur in the $Cu(CO)_3$ bands in the spectra corresponding to matrices deposited at 18K and above. Spectra A – F correspond to deposition temperatures of 14, 16, 18, 20, 22, and 24K.

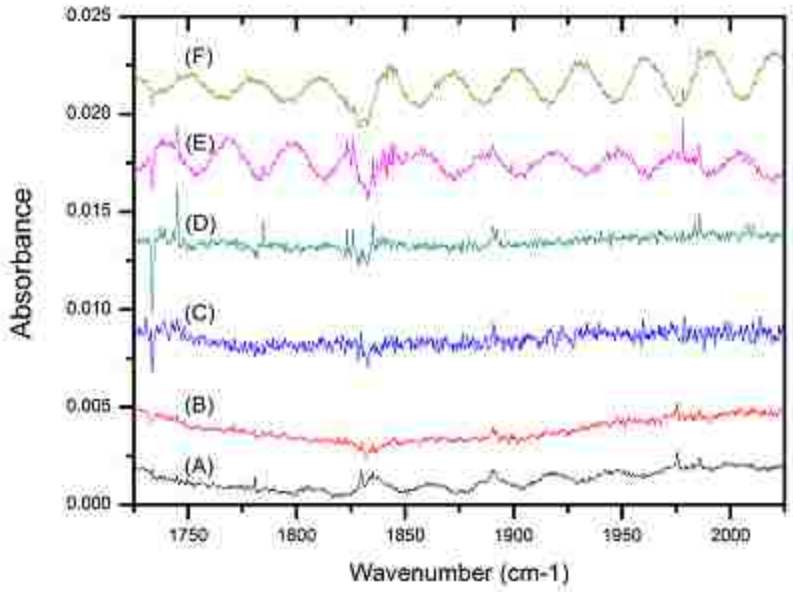


**Figure 5.5:** Infrared difference spectra highlighting changes following annealing to 30K after deposition (Annealing spectrum minus deposition spectrum). Some changes appear consistent across all deposition temperatures while some changes appear dependent upon the temperature at which the matrix was originally deposited. Spectra A – F correspond to deposition temperatures of 14, 16, 18, 20, 22, and 24K. Note the conversion of the $CuCO^-$ band from 1733 $cm^{-1}$ to 1745 $cm^{-1}$ that is especially clear in the 20K and 22K spectra.

# Chapter 6

## Improvements in Ion Delivery for Matrix-Isolation Spectroscopy: Simultaneous Deposition of Mass Selected Anions and Cations

### 6.1 Abstract

Improving ion deposition methods for matrix-isolation spectroscopy to provide greater control over deposited ionic species, while minimizing contamination of undesired neutral species, has been a focus of the work in the Moore lab. In this chapter, I discuss the implementation of the method for simultaneous deposition of mass selected anions and cations into a cryogenic matrix. Initial experiments involving mass selection of $Ar^{2+}$ with the copper carbonyl system are discussed, and it is shown that the charge of the counter ion does not affect other species present in the matrix. Then, experiments in which a specific cationic fragment of $SF_6$, $SF_5^+$ or $SF_3^+$, were co-deposited with $Cu^-$ into CO doped matrices will be presented. Upon deposition, metal carbonyl anions are observed, along with the mass selected counter ion $SF_5^+$. Following photodetachment of electrons by irradiation with narrow band LEDs, the neutral analogues of the metal carbonyls are observed. Additionally, the photodetached electrons combine with cation centers in the matrix, as evidenced by a lowering of the $SF_5^+$ signal and the growth of a neutral $SF_5$ band. This improved characterization of the fate of photodetached electrons is possible due to the presence of a cationic spectroscopic signature in the matrix upon deposition. The method of simultaneous deposition of mass selected ions allows more complete characterization of charge transfer processes in cryogenic matrices and could be used in future experiments to study other ion-ion interactions in the environment of a cryogenic matrix.

## 6.2 Introduction

Matrix isolation spectroscopy has long been recognized as a useful method for the study of unstable species, such as ions, weakly bound complexes, and reactive intermediates.[27, 98-100] The study of these reactive species in cryogenic matrices was facilitated by rapid stabilization due to the fast energy dissipation of the matrix, and by the caging effect of the matrix, which created a physical barrier between possible reactants.[3, 5] The requirement that the matrix remain charge-balanced imposes a limitation on matrix-isolation experiments involving ions. Any method for the study of ions in matrices must result in the trapping or formation of both anions and cations. A number of techniques have been developed to ensure this condition is maintained. In early examples of such experiments, ions were generated *in situ* from precursor molecules through photo- or chemi-ionization, resulting in the formation of ion pairs.[22, 101] Ions can be generated by electron bombardment of the matrix during formation.[102] Several methods generate ions in close proximity to the matrix, which are then co-deposited with the matrix gas. Two significant examples of these methods include laser ablation of metals, developed by Andrews,[27] and microwave discharge plasmas of noble gases, developed by Jacox.[82, 103] These ion deposition methods result in the formation of both positively and negatively charged ions, which inherently satisfies the charge balance requirement. The spectroscopic signature of both anions and cations trapped in the matrix are generally present when these methods are employed.

A downside to the generation of ions in proximity to the matrix is minimal direct control over the energy or identity of trapped ionic species. For example, laser ablation of a metal near the matrix creates anionic, cationic, and neutral metal species, which results

in the formation of anionic, cationic, and neutral metal complexes upon deposition.[27] The Maier group was the first to develop a method to increase control over the identity and energy of trapped ions by coupling the output of a mass spectrometer to a matrix isolation deposition system.[32] An externally generated ion beam was mass selected in a quadrupole mass filter before being co-deposited with a matrix gas, and the spectroscopic signatures of the mass selected ion was present upon deposition. Additional ionic species were also observed because the species could fragment due to high (150 eV+) deposition energy. Counter ions are generated by secondary ionization events during the deposition of the high energy cations.[32, 104]

In previous publications from this group,[40, 41] the method of counter ion co-deposition has been introduced, which provided increased control over the identity and energy of ions deposited into a matrix. Similar to Maier's technique, counter ion co-deposition couples ion delivery to the output of a mass spectrometer. However, this technique uses deposition of distinct beams of anions and cations, so secondary ionization events are not necessary to generate counter ions in the matrix, allowing for lower ion deposition energies. Earlier work from this group highlights results from the simultaneous deposition of low energy, mass selected copper anions with argon counter cations into argon matrices doped with carbon monoxide.[40] This deposition procedure resulted in the formation of a clean distribution of only copper mono-, di-, and tri-carbonyl anions with no presence of the neutral analogues. Photodetachment of the anions via irradiation of the matrix with light from a tungsten filament bulb led to the appearance of neutral copper carbonyl species.

In these earlier publications, the counter ion co-deposition system allowed mass resolution of the anionic copper beam, but not the counter cation. A beam of copper anions was generated in a magnetron sputtering source and passed through a mass resolving quadrupole. Counter cations were generated in an electron impact ionization source. The two beams entered into opposite sides of a quadrupole bender, where they were combined and directed toward the matrix deposition window. The original system lacked the ability to mass resolve the counter cation, so in order to maintain the desired level of control over the identity of deposited species, only molecular gases, such as argon or krypton, were used as counter ion sources. Due to this limitation, there was no spectroscopic signature to track cations in the matrix throughout an experiment. The original instrumental design was modified to include a second mass resolving quadrupole between the electron impact ionization source and the bender, which granted simultaneous mass resolution of both the anions and cations deposited into the matrix. To my knowledge, this is the first time multiple mass selected ion beams have been simultaneously deposited into a cryogenic matrix. Results of a preliminary system in which mass selected $Cu^-$ and $SF_5^+$ have been deposited into a CO-doped argon matrix are discussed.

**6.3 Experimental Methods**

Experiments presented in this chapter were carried out using the updated counter ion co-deposition system with simultaneous mass resolution of both the anionic and cationic beams. The first test of the system was carried out using mass selected $Ar^{2+}$ co-deposited with $Cu^-$. Subsequent results are presented for a $Cu^-/SF_6$ cation derivative system. Low-energy copper anions are generated in a magnetron sputtering source, pass

through a quadrupole ion guide and are then mass selected in a mass resolving quadrupole. A beam of counter cations (22 eV $SF_5^+$, 60 eV $SF_5^+$, or 22 eV $SF_3^+$) is generated in an electron impact ionization source and is directed into a second mass resolving quadrupole. The two beams are combined in a quadrupole ion bender and turned toward the matrix deposition window. The beams are detected on a Faraday plate, and current of the two beams are matched which ensures an equal flux of anions and cations will be deposited in the matrix. The bender also ensures that there is no line of sight for neutral metal species to contaminate the matrix, though some neutral $SF_6$ is observed in the spectrum. The ions are co-deposited with a matrix gas consisting of argon doped with 0.02% CO. The matrix is deposited for a period of four hours onto a CsI window maintained at 20K using a closed cycle helium cryostat. The entire experiment was performed under darkened conditions, as it was found that the ambient light in the lab could result in the photoneutralization of anionic species in the matrix. After deposition, a series of annealing or irradiation steps were performed. For irradiation, the matrix was illuminated for ~5 minutes with a 590 or 470nm LED, and for annealing, the matrix was warmed as high as 35K and held for ~15 minutes at the given temperature. Following each processing step, the matrix was cooled to 10K and a transmission mode FTIR spectrum was recorded.

**6.4 Results and Discussion**

Upon installation of the new ion source and quadrupole providing mass resolution of the counter ion beam, initial optimization of the optics and quadrupole were carried out using argon cations generated in the new electron impact ionization source. The resulting mass spectrum revealed that the EI source was generating both $Ar^+$ and $Ar^{2+}$,

which was unexpected but not surprising. This observation meant that in all previous experiments in which argon was the counter ion gas, the deposited counter cation beam was a mixture of both $Ar^+$ and $Ar^{2+}$. The first experiments performed using the new deposition system involved mass selecting specifically for $Ar^{2+}$, which would determine if the charge of the counter ion present in the matrix had an effect on other observed reactions.

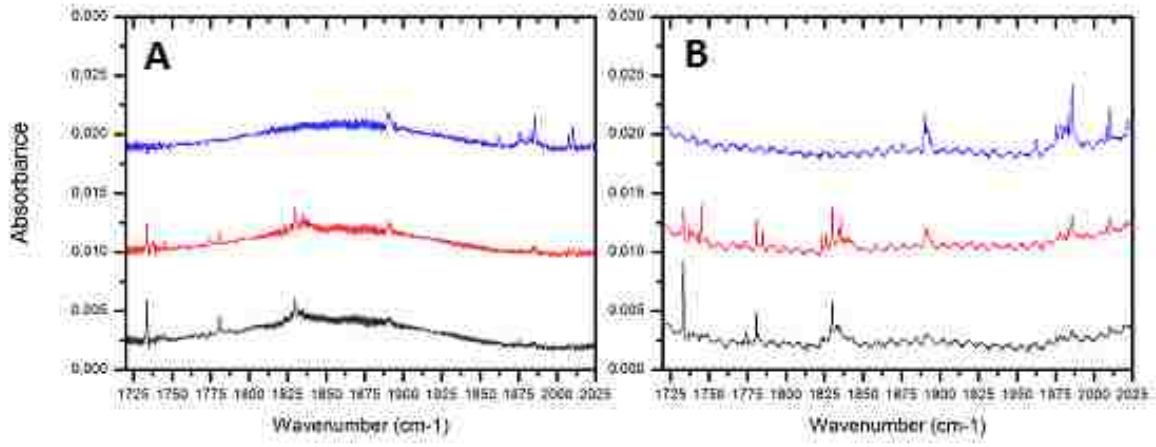


**Figure 6.1:** Comparison of copper carbonyl infrared spectral region with updated and original ion delivery method. (A) Co-deposition of simultaneous mass selected beams of $Cu^-$ and $Ar^{2+}$ and (B) co-deposition using original ion delivery method resulting in deposition of mass selected $Cu^-$ with a mixture of $Ar^+$ and $Ar^{2+}$. Results show qualitatively similar results for deposition (20K, 0.02% CO in Ar, black spectra), annealing to 30K (red spectra), and 470 nm photolysis (blue spectra).

Figure 6.1 shows a comparison of an experiment in which mass selected $Ar^{2+}$ was the counter ion (Fig. 6.1 A), and one from the original deposition method in which a mixture of $Ar^+$ and $Ar^{2+}$ was deposited (Fig. 6.1 B). The difference in intensity between the two methods is likely due to reduced ion abundance in the $Ar^{2+}$ experiment. A maximum of approximately 2nA of $Ar^{2+}$ could be produced, while the earlier experiments were limited by the $Cu^-$ flux of approximately 4-5 nA. Upon annealing to 30K, the red spectra in Figure 6.1 A and B, anionic copper carbonyl site peaks appear,

which are discussed in the previous chapter. There are some noticeable differences in the appearance of the site peaks, especially the conversion of the peak at 1733 $cm^{-1}$ to 1745 $cm^{-1}$ upon annealing, and subsequent formation of the peak at 2022 $cm^{-1}$ upon photolysis. This difference may be due to abundance of the copper carbonyl anions in the matrix, but it may also be due to the difference in cations, because using $SF_5^+$ as the counter ion also has an effect on site peak formation. With the exception of site-peak behavior, the appearance of copper carbonyl peaks upon deposition and through processing is qualitatively the same, which suggests the charge of the cation has minimal effect on the anion behavior in the matrix.

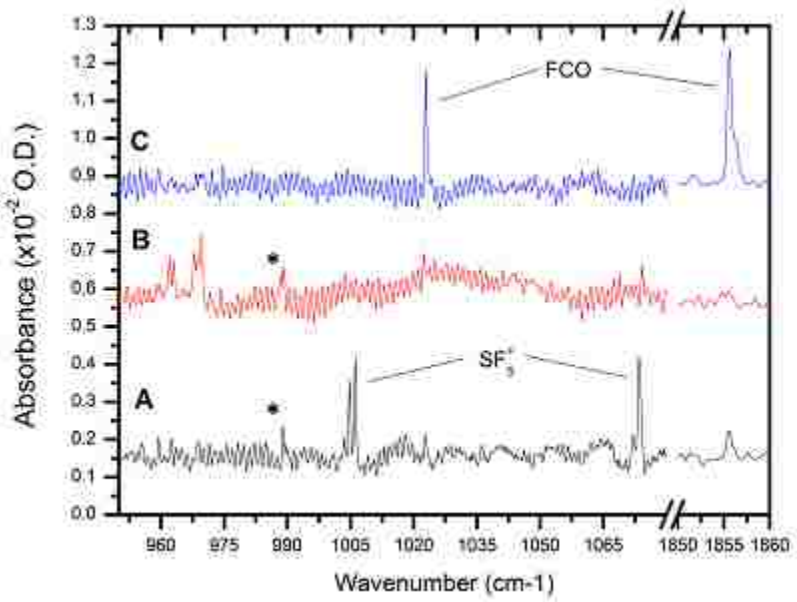


**Figure 6.2:** Infrared spectra showing the effect of counter ion selection upon deposition of (A) 22eV $SF_5^+$, (B) 22eV $SF_3^+$, and (C) 60eV $SF_5^+$. Each spectrum was taken following otherwise identical deposition conditions: co-deposition with $Cu^-$ into an argon matrix doped with 0.02% CO at 20K. Peaks arising from anionic copper carbonyls upon deposition were identical, independent of counter ion choice. *The peak at ~990 $cm^{-1}$ was not considered in our analysis, but may arise due to neutral $SF_6$ in the matrix.

Figure 6.2 illustrates the control over both counter cation energy and identity using the improved method of counter ion co-deposition. In all three spectra shown, $SF_6$

was introduced into the electron-impact ionization source. Figure 6.2 (A) shows bands associated with $SF_5^+$ observed upon co-deposition of low energy, 22 eV, mass-selected $SF_5^+$ and $Cu^-$ into a 0.02% CO doped argon matrix. A pair of doublets is observed at 1004.7 and 1006.1 $cm^{-1}$, and 1072.2 and 1073.4 $cm^{-1}$, and the small band observed at 1855.6 $cm^{-1}$ has been previously assigned to the C-O stretching mode of FCO.[105] The spectrum obtained upon deposition of mass selected $SF_3^+$, under otherwise identical experimental conditions, is shown in Figure 6.2 (B). A doublet at 962.5 and 963.5 $cm^{-1}$, as well as a broader feature at 969 $cm^{-1}$ are present. The feature at 989 $cm^{-1}$ has been assigned to an overtone band of $SF_6$.[106] The doublet of peaks observed upon deposition of $SF_5^+$ is absent. An assignment for $SF_5^+$ in argon has not been previously reported. We assign the pair of doublets at 1004.7 and 1006.1 $cm^{-1}$, and 10072.2 and 1073.4 $cm^{-1}$ to $SF_5^+$ based on a previous assignment by Jacox's of $SF_5^+$ in a neon matrix at 1008.2 and 1074.8 $cm^{-1}$,[107] and the fact that the bands are not observed upon deposition of mass selected $SF_3^+$. It is not yet clear why $SF_5^+$ appears as a pair of doublets in argon, while it was only reported as two single peaks in neon. Additionally, it is somewhat surprising that the shifts between argon and neon are so small, considering that one would expect nearby argon atoms in the matrix to interact more strongly with the cationic center than neon would due to the difference in polarizability between argon and neon.

Figure 6.2 C shows the effect of depositing high energy (60 eV) $SF_5^+$, instead of 22eV $SF_5^+$. The pair of doublets which have been assigned to $SF_5^+$ are not present in the spectrum. Instead, a peak at 1022.8 $cm^{-1}$, previously assigned to the F-C stretching mode of FCO,[105] is observed. The C-O stretching mode of FCO at 1855.6 $cm^{-1}$ is also shown to increase in intensity by a factor of five compared to low energy $SF_5^+$ experiments. These

results show that $SF_5^+$ does not survive deposition, indicating that depositing at 60eV provides sufficient energy to break the S-F bonds of $SF_5^+$ upon deposition, and that neutral F atoms are released into the matrix, which then react with free CO. Presumably, the cations in the matrix are either $S^+$ or $SF_x^+$ (x<5), but no peaks which could be attributed to cations are observed under these deposition conditions. High-energy deposition of $SF_5^+$ could be useful for providing an F atom source for matrix isolation experiments while simultaneously acting as a source of cations in the matrix. Other peaks in the spectrum, including a band at 938 $cm^{-1}$ assigned to neutral $SF_6$,[106] and the bands assigned to copper carbonyl anions are not affected by cation deposition conditions.

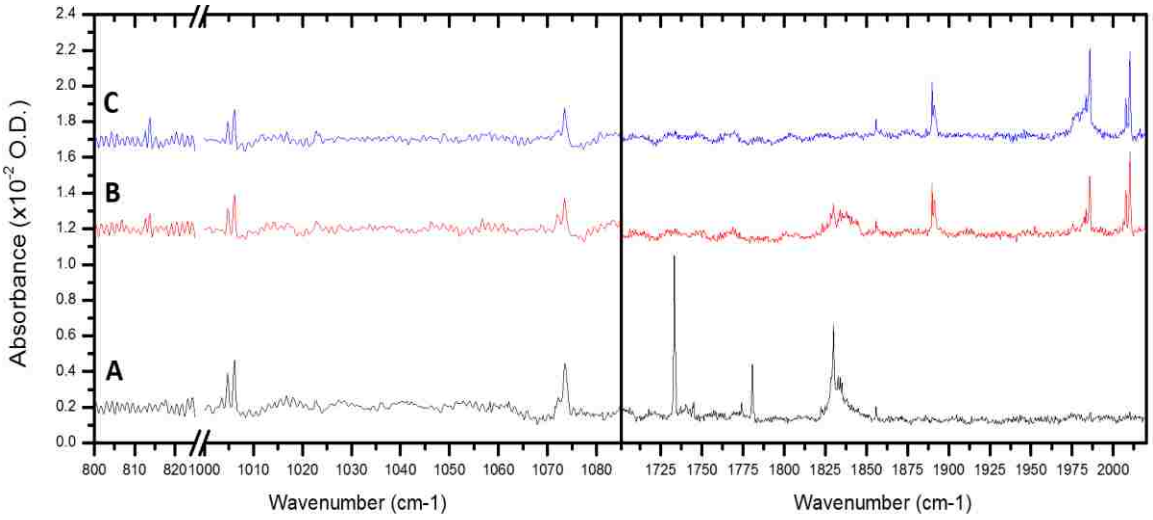


**Figure 6.3:** Infrared spectra of $SF_5$ (L) and copper carbonyl I regions after co-deposition of $Cu^-$ and $SF_5^+$ for four hours with 0.02% CO in argon at 20K (A) After cooling to 10K following deposition. (B) After 5 minutes of irradiation with 590nm LED. (C) After 5 minutes of irradiation with 470nm LED.

In experiments before the system modification, a cationic spectroscopic signature was not present in the matrix because the counter cation choice was either $Ar^+$ or $Kr^+$. A previous publication from this group discussed photochemistry induced by photodetached electrons from anionic copper carbonyls.[41] It was found that these electrons could

combine with van der Waals CO dimers to form the covalently bound $OCCO^-$ species. This result was surprising as we had hypothesized that these electrons should combine with cation centers in the matrix, but previously there was no direct way to measure if this was occurring. Use of $SF_5^+$ as the counter ion now allows direct spectroscopic observation of the fate of photodetached electrons. Figure 6.3 (A) shows the anionic copper carbonyl bands, appearing between 1730 and 1840 $cm^{-1}$, and $SF_5^+$ bands before irradiation. Figure 6.2 (B) and (C) shows the resulting spectra after five minutes of irradiation first with a 590 nm narrow band LED, followed by five minutes of irradiation with a 470 nm narrow band LED (Emission spectra for the LEDs are shown in Figure 2.11). In spectra (B) and (C), the anionic copper carbonyl bands are depleted, and are replaced with their neutral analogues, appearing between 1880 and 2010 $cm^{-1}$, due to photodetachment of the extra electron. The behavior of copper carbonyl complexes trapped in argon matrices has been characterized in depth previously by this group and others.[15, 40, 42] The pair of doublets assigned to $SF_5^+$ are depleted slightly upon 590 nm irradiation, and a doublet with peaks at 812.6 and 813.5 $cm^{-1}$ appears. A peak at 813.1 $cm^{-1}$ has been previously assigned to neutral $SF_5$ in argon,[108] so we attribute the growth of this doublet to the formation of neutral $SF_5$. It is interesting to note that the splitting observed by the cationic peaks is also observed in the neutral analogue. The depletion of $SF_5^+$ and growth of $SF_5$ continues as the remaining copper carbonyl anions are neutralized during 470nm irradiation. These results show that photodetached electrons from the anionic copper carbonyl complexes travel through the matrix and combine with cationic $SF_5^+$, resulting in the formation of $SF_5$.

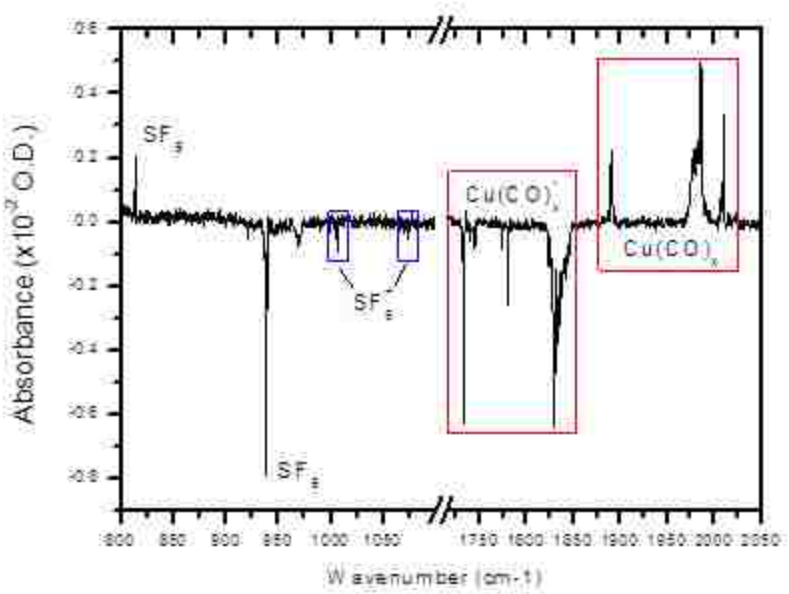


**Figure 6.4:** Difference IR spectrum highlighting spectral changes due to irradiation of the matrix with visible light, including the depletion of copper carbonyl anions, the growth of the corresponding copper carbonyl neutral species, and the depletion and subsequent growth of $SF_5^+$ and $SF_5$. A significant depletion in the neutral $SF_6$ band at 938 $cm^{-1}$ is also observed upon irradiation.

The difference spectrum shown in Figure 6.4 highlights the spectral changes due to irradiation. In addition to the changes discussed previously, it shows a large negative peak at 938 $cm^{-1}$, due to loss of neutral $SF_6$. This difference represents a depletion in the band of approximately 7% of its original intensity (Figure 6.6). The only positive peaks in the difference spectra following photodetachment can be attributed to neutralization of the copper carbonyl species or neutralization of $SF_5^+$. It has been noted by Jacox that upon irradiation of a neon matrix containing anions and neutral $SF_6$ with a mercury arc lamp, $SF_6$ captures photodetached electrons, but the 254 nm radiation used in that work has sufficient energy to destroy the $SF_6^-$ ion, resulting in the formation of $SF_5^-$ + F.[107] Previous assignments for $SF_5^-$ indicate it should appear at 795.5 $cm^{-1}$ in an argon matrix,[108, 109] but no band is observed to grow at that location following irradiation. It is

possible that the 470nm LED source used for irradiation is gentle enough that it does not destroy $SF_6^-$; however, based on the assignment of $SF_6^-$ in neon,[107] any bands associated with that species would appear outside of the limit of our detector.

Since the cationic $SF_5^+$ bands are not fully depleted through capturing photodetached electrons, it is interesting that the neutral $SF_6$ band is also observed to be depleted. It raises the question of why electrons would be captured by a neutral molecule while cationic species are present in the matrix. The answer may simply involve the relative abundance of each species. Despite the fact that the electron impact ionization source, where $SF_6$ is introduced into our vacuum system, is two differentially pumped chambers from the deposition region, neutral $SF_6$ is trapped during matrix formation. Based on pressure measurements in the deposition region, it can be estimated that the matrix contains ~0.01% $SF_6$, or 1 $SF_6$ atom per $10^5$ argon atoms. Previous calculations for our deposition system suggest an ion concentration of 3 cations per $10^7$ argon atoms,[40] or approximately a two order of magnitude difference between $SF_6$ and $SF_5^+$ concentration. It is possible that the driving force for the photodetached electrons to seek out a cation is overcome by the increased likelihood of interacting with an $SF_6$ molecule. Future work could include experiments testing different irradiation wavelengths to determine if more or less energetic electrons favor attachment to the neutral or cationic species, which could give additional insight into the electron capture mechanisms of these species. The ability to deposit two mass selected beams of ions simultaneously into a matrix presents advantages beyond being able to spectroscopically track anionic and cationic species and the behavior of the system following photodetachment of electrons. Simultaneously depositing multiple mass selected ions into a matrix will provide the

opportunity to do more advanced and controlled studies of specific ion-ion interactions in cryogenic matrices.

## 6.5 Appendix

### 6.5.1 Neutral $SF_6$

An additional benefit of the new deposition system design is an extra stage of differential pumping between the counter ion gas delivery and the matrix deposition window. Previously, the counter ion gas was introduced in the bender chamber. When an IR-active species was used as the counter ion, such as $SF_6$ or NO, significant contamination by the gas was observed in the matrix following deposition. The improved pumping of the new system is shown in Figure 6.5, which compares the neutral $SF_6$ peaks observed in the matrix between the old and new deposition system.

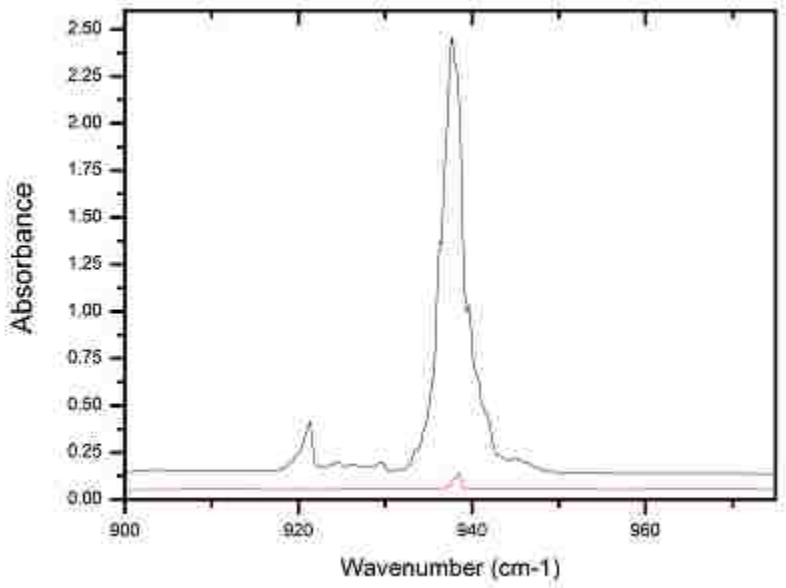


**Figure 6.5:** The black spectrum shows the peak associated with neutral $SF_6$ in an experiment using the original deposition system, compared with the red spectrum showing the neutral $SF_6$ peak with the new deposition system.

As mentioned in the body of the chapter, a reduction in the neutral $SF_6$ peak is observed following irradiation of the matrix, meaning electrons which have been photodetached from the anionic copper carbonyls in the matrix are combining with neutral $SF_6$ molecules. Figure 6.6 shows the difference in the $SF_6$ peak before (black spectrum) and after (red spectrum) irradiation. The reduction in the integrated intensity is approximately 7%.

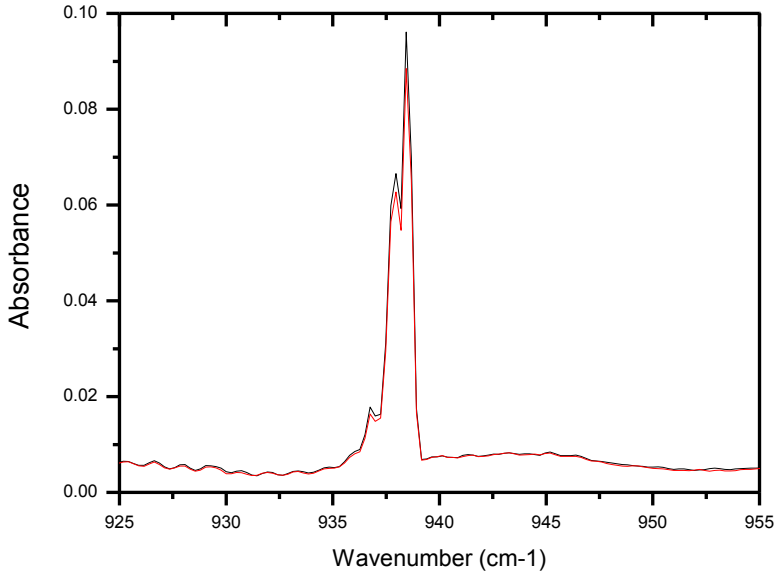


**Figure 6.6:** Overlay of spectra showing change in neutral $SF_6$ peak before (Black spectrum) and after (Red Spectrum) irradiation with 590 and 470nm LED each for five minutes. Integration of both peaks reveals a ~7% reduction in intensity following irradiation.

### 6.5.2 Stopping-Potential Curves

The energy distribution of the counter cation beams were found by generating stopping-potential curves. Ideally the ion energy should match the bias applied to the ion region of the electron impact ionization source, which is the potential the ion feels when it is created. The cation current was measured at the Faraday plate as a function of bias applied to the octupole exit plate, which is the final optic the ions feel before the beam

enters the deposition chamber. The results were then integrated, yielding the distributions shown in figures 6.7 – 6.9.

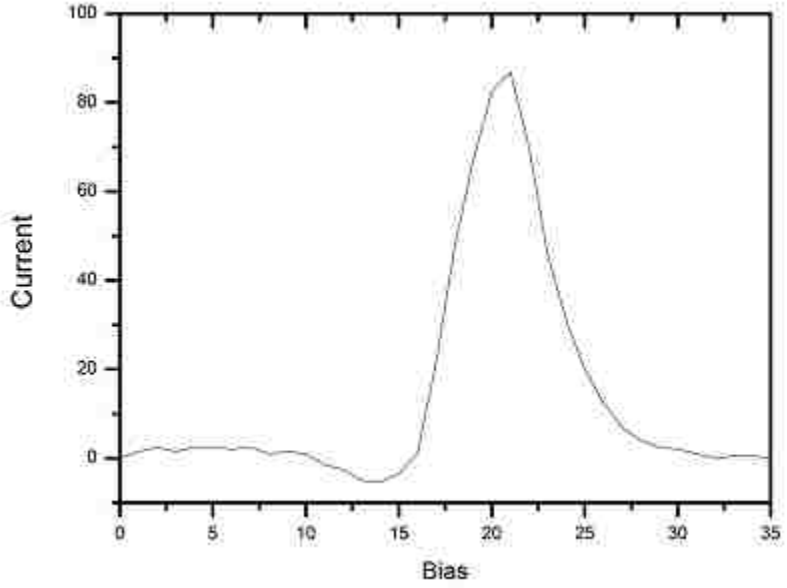


**Figure 6.7:** Stopping-potential curve for 22 eV (as set at the EI ion region) $SF_5^+$. The peak occurs at 21 eV.

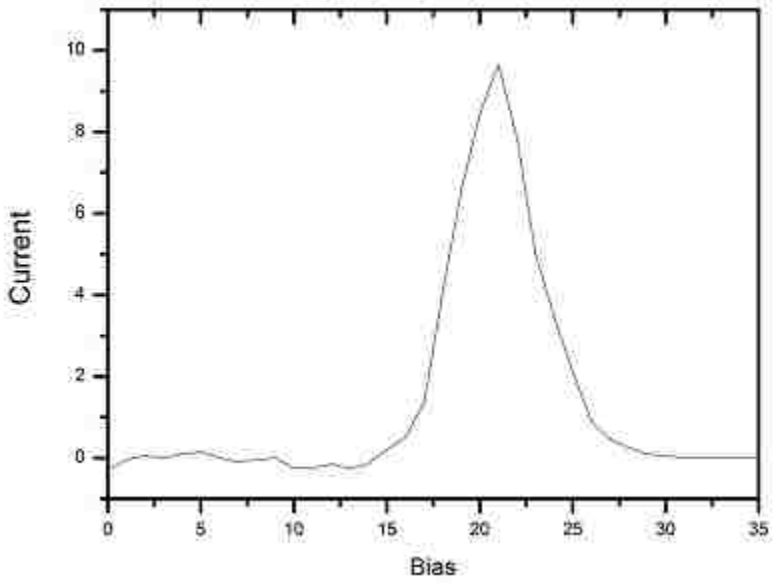


**Figure 6.8:** Stopping-potential curve for 22 eV $SF_3^+$. The peak occurs at 21 eV.

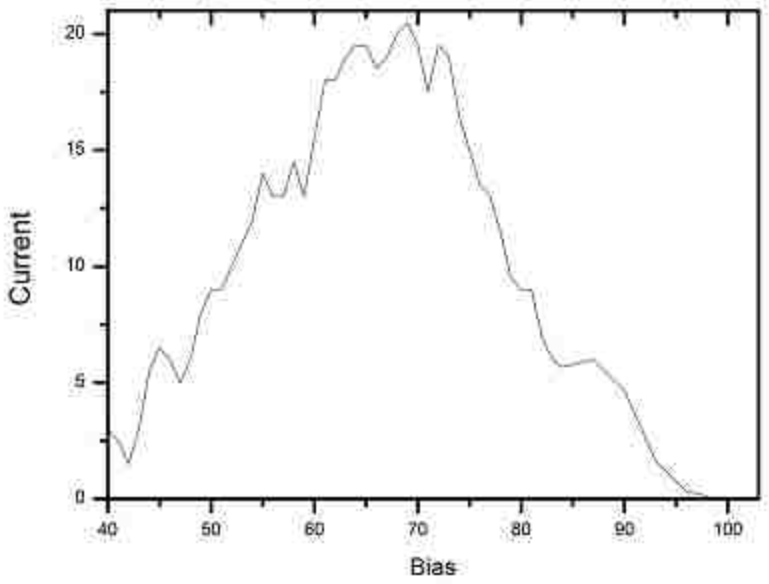


**Figure 6.9:** Stopping-potential curve of 60 eV $SF_5^+$. The broad distribution is likely due to the octupole exit lens not being thick enough to fully reject the fast, heavy $SF_5^+$ cations. The beam was confirmed to have energy close to 60 eV by adjusting the pole bias of the resolving quadrupole. Above 60V, no ion current could be detected passing through the quadrupole.

# Chapter 7

## Conclusions and Future Work

### 7.1 Conclusions

The results in this dissertation show the broader applicability of the counter ion co-deposition technique beyond the metal carbonyl system, and presented a method to improve the technique by broadening the scope of ionic species which can be studied. Ionic $CO_2$ and copper $CO_2$ complexes have been characterized using the new technique. The formation of $CO_2$ anions only after irradiation of an argon matrix following co-deposition of $Cu^-$ and $Ar^+$ shows that the charge remains localized on $Cu^-$ following deposition. Comparing this observation with the results of high energy $Ar^+$ deposition, in which ionic $CO_2$ complexes are formed immediately upon deposition shows that the low energy deposition of the counter ion co-deposition technique successfully minimizes secondary ionization events, thereby limiting the number of ionic species in the matrix. I also found that high temperature deposition resulted in appearance of new bands which could be assigned to anionic $CO_2$ complexes. The observation of increased spectral complexity following high temperature deposition is similar to that of the anionic copper carbonyl system upon deposition at 20K and may arise from an increase in the number of available trapping environments at higher temperatures.

The discovery of a temperature dependent equilibrium of $(CO_2)(CO_2^-)$ and $C_2O_4^-$ while studying $CO_2$ doped matrices was unexpected. A thermodynamic characterization was performed in the manner of previously reported matrix isolated equilibrium processes, and it was found that the process was endothermic and driven by an increase in the entropy of the system. Unlike earlier reported equilibrium processes, a complete

temperature dependent characterization of the forward and reverse reactions were performed, and the thermodynamic constants for the reaction were calculated independently of the thermodynamic characterization. The two methods were found to be in agreement. Use of the Eyring equation to determine entropic and enthalpic barriers between reactants and transition states allowed the visualization of a crude but experimentally determined potential energy surface for the reaction. Despite our confidence in assigning a large entropic gain as the driving force for the reaction, we have been unable to determine the exact nature of the change, beyond the fact that we believe that it arises from the matrix and not the species directly involved in the equilibrium. Comparison with existing gas phase experiments showed a discrepancy between the assigned minimum energy structure, and it seems likely that the matrix preferentially stabilizes the separated $(CO_2)(CO_2^-)$ structure at low temperature.

The temperature dependent deposition of a CO-doped argon matrix with $Cu^-$ and $Ar^+$ provided interesting insights into the formation mechanism of anionic copper carbonyls. As was expected, the concentration of copper carbonyls was found to increase with deposition temperature, and trends in the distribution of mono-, di-, and tri-carbonyls showed that formation of the copper tri-carbonyl is favored at higher temperatures, consistent with a longer diffusion period on the matrix surface. These results can also explain the increase in intensity of ionic $CO_2$ complexes observed following deposition at higher temperatures. Deposition at the highest temperatures in the study showed that eventually, $Cu^-$ becomes the limiting reagent in the formation of copper carbonyl anions, as the total intensity seemed to reach a maximum at 22K and did not increase more at 24K. Behavior upon annealing following deposition at low

temperatures also indicated that "precursor" complexes may form, in that only small changes in the structure of the matrix induced by annealing are required to generate higher coordinated copper carbonyl anions, which suggests that the molecules are frozen out just before formation of the anionic species.

Finally, the broader applicability of the counter ion co-deposition technique has been increased by adding the ability for simultaneous co-deposition of mass selected anions and cations. The initial results of the mass selected $Cu^-/SF_5^+$ system produced peaks in the spectrum which could be assigned to anions and cations immediately upon deposition, and were directly correlated with the mass selected ions. The cationic signal allowed for characterization of the fate of photodetached electrons following irradiation of the matrix, which neutralized the copper carbonyl anions. Reduction in the $SF_5^+$ peaks and subsequent growth of an $SF_5$ neutral peak shows that photodetached electrons combine with cation centers in the matrix, generating the corresponding neutral species.

## 7.2 Future Directions

### 7.2.1 Characterization of the $CO_2$ Dimer Anion Equilibrium

An obvious direction for future work is to further attempt to characterize the large entropy change which is driving the $CO_2$ dimer anion equilibrium. Characterization of the system in both krypton and argon has yielded the same difference in entropy between the low and high temperature species. It would be interesting to test additional matrix materials, including neon and xenon, to see if entropy change remains consistent or changes. Computational studies that model the system within the matrix may be required to obtain an accurate visualization of how the reaction proceeds.

Deposition of a $CO_2$ doped argon matrix at 20K produced additional peaks which were believed to correspond to additional site peaks of both $C_2O_4^-$ and $(CO_2)(CO_2^-)$. Initial analysis has revealed that conversion between these peaks occurs at lower temperatures than the main peaks previously assigned to the dimer anion species. This conversion was observed to occur between 13K and 19K, compared to the conversion occurring between 19K and 23K for the main peaks. Isotopic substitution experiments could be performed to determine if these peaks are due to larger $(CO_2)_n^-$ clusters. If so, further characterization of the equilibrium process could provide additional insight into the role of the matrix in the core ion switching mechanism. If larger clusters are indeed being formed due to high temperature deposition, additional studies could be performed to determine if specific cluster sizes do not undergo the change from $(CO_2)(CO_2^-)$ to $C_2O_4^-$. It would also be interesting to observe if any cluster size resulted in the stabilization of the dimer anion at low temperature, potentially indicating a symmetric stabilization of the anion similar to previously observed experimental results in the gas phase.[79, 80]

### 7.2.2 Utilizing the Chemical Ionization Source

Introduction of simultaneous mass selection of the counter-ion beam provides more opportunities for interesting experiments beyond the simple test case of observing spectroscopic signatures following the controlled deposition of cations and anions simultaneously. The chemical ionization source allows for the generation of anionic counter ions and cations which can only form *via* gas phase reactions. Anionic counter ions would open up the possibility of testing cationic metals, which are formed in the magnetron sputtering source. Initial tests of the source indicated that $Cu^+$ currents

exceeding 20 nA can be detected at the Faraday plate, so the only barrier to those experiments has been the production of a suitable counter ion, and previous works have shown that $SF_6^-$ can be readily generated under conditions achievable in a chemical ionization source.[110, 111]

## Chapter 8

### List of References


(1) Whittle, E.; Dows, D. A.; Pimentel, G. C. Matrix Isolation Method for the Experimental Study of Unstable Species *J. Chem. Phys.* **1954**, *22*, 1943.

(2) Becker, E. D.; Pimentel, G. C. Spectroscopic Studies of Reactive Molecules by the Matrix Isolation Method *J. Chem. Phys.* **1956**, *25*, 224-228.

(3) Cradock, S.; Hinchcliffe, A. J. In *Matrix Isolation a Technique for the Study of Reactive Inorganic Species;* Cambridge University Press: New York, NY, 1975.

(4) Moskovits, M.; Ozin, G. A. In *Techniques of Matrix Cryochemistry;* Moskovits, M., Ozin, G. A., Eds.; Cryochemistry; John Wiley & Sons, Inc.: New York, 1976; pp 9-60.

(5) Dunkin, I. R. In *Matrix isolation techniques: A practical approach;* Oxford University Press: Oxford; New York, 1998.

(6) Jacox, M. Vibrational and Electronic Energy Levels of Polyatomic Transient Molecules. Supplement B *J. Phys. Chem. Ref. Data* **2003**, *32*, 1-441.

(7) Jacox, M. Vibrational and Electronic Energy Levels of Polyatomic Transient Molecules. Supplement A *J. Phys. Chem. Ref. Data* **1998**, *27*, 115-393.

(8) Jacox, M. E. The Spectroscopy of Molecular Reaction Intermediates Trapped in the Solid Rare Gases *Chem. Soc. Rev.* **2002**, *31*, 108-115.

(9) Hoops, M. D.; Ault, B. S. Matrix Isolation Study of the Early Intermediates in the Ozonolysis of Cyclopentene and Cyclopentadiene: Observation of Two Criegee Intermediates *J. Am. Chem. Soc.* **2009**, *131*, 2853-2863.

(10) Girardet, C.; Maillard, D. In *Interpretation of Infrared and Raman Spectra of Trapped Molecular Impurities from Interaction Point Calculations;* Barnes, A. J., Ed.; Matrix Isolation Spectrsocopy; D. Reidel Publishing Company: Dordrecht, Holland, 1981; pp 275-346.

(11) Kolb, D. M.; Forstmann, F. In *Matrix Induced Changes in the Electronic Spectra of Isolated Atoms and Molecules;* Barnes, A. J., Ed.; Matrix Isolation Spectroscopy; D. Reidel Publishing Company: Dordrecht, Holland, 1981; pp 347-398.

(12) Milligan, D. E.; Jacox, M. E. Infrared Spectroscopic Evidence for the Stabilization of $HAr_n^+$ in Solid Argon at 14 K *J. Mol. Spectro.* **1973**, *46*, 460-469.

(13) Leroi, G. E.; Ewing, G. E.; Pimentel, G. C. Infrared Spectra of Carbon Monoxide in an Argon Matrix *J. Chem. Phys.* **1964**, *40*, 2298-2303.

(14) Forstmann, F.; Kolb, D. M.; Leutloff, D.; Schulze, W. Analysis of Matrix Induced Changes in Optical-Spectra of Matrix-Isolated Noble-Metal Atoms *J. Chem. Phys.* **1977**, *66*, 2806-2813.

(15) Zhou, M.; Andrews, L. Infrared Spectra and Density Functional Calculations of $Cu(CO)_{1-4}^{+}$, $Cu(CO)_{1-3}$, and $Cu(CO)_{1-3}^{-}$ in Solid Neon *J. Chem. Phys.* **1999**, *111*, 4548-4557.

(16) Barnes, A. J. In *Infrared and Raman Matrix Isolation Spectroscopy;* Barnes, A. J., Ed.; Matrix Isolation Spectroscopy; D. Reidel Publishing Company: Dordrecht, Holland, 1981; pp 13-26.

(17) Darling, J.; Ogden, J. Spectroscopic Studies on Matrix-Isolated Metal-Carbonyls .1. Use of Co-18 Enrichment to Obtain Characteristic Frequency and Intensity Patterns *J. Chem. Soc., Dalton Trans.* **1972**, , 2496-2503.

(18) Jacox, M. E. The Spectroscopy of Molecular Reaction Intermediates Trapped in the Solid Rare Gases *Chem. Soc. Rev.* **2002**, *31*, 108-115.

(19) Pimentel, G. C. Reaction Kinetics by the Matrix Isolation Method: Diffusion in Argon; cis-trans isomerization of Nitrous Acid *J. Am. Chem. Soc.* **1958**, *80*, 62-64.

(20) Fausto, R.; Khriachtchev, L.; Hamm, P. In *Conformational Changes in Cryogenic Matrices;* Khriachtchev, L., Ed.; Physics and Chemistry at Low Temperatures; Pan Stanford Publishing: Singapore, 2011; pp 51-84.

(21) Kundig, E.; Ozin, G. Trigonal Bipyramidal Chromium Pentacarbonyl and its Implications to Structure and Bonding Considerations of Pentacarbonyls and Pentacarbonyl Anions *J. Am. Chem. Soc.* **1974**, *96*, 3820-3823.

(22) Kasai, P.; McLeod, D. Electron Spin Resonance Study of Molecular Anions Generated in Argon Matrix at 4 Degrees K - ESR Spectrum of $B_2H_6^-$ *J. Chem. Phys.* **1969**, *51*, 1250-1251.

(23) Bondybey, V. E.; English, J. H. Laser-Induced Fluorescence of Metal-Clusters Produced by Laser Vaporization - Gas-Phase Spectrum of $Pb_2$ *J. Chem. Phys.* **1981**, *74*, 6978-6979.

(24) Gong, Y.; Zhou, M.; Andrews, L. Spectroscopic and Theoretical Studies of Transition Metal Oxides and Dioxygen Complexes *Chem. Rev.* **2009**, *109*, 6765-6808.

(25) Andrews, L.; Zhou, M.; Gutsev, G.; Wang, X. Reactions of Laser-Ablated Chromium Atoms, Cations, and Electrons with CO in Excess Argon and Neon: Infrared Spectra and Density Functional Calculations on Neutral and Charged Unsaturated Chromium Carbonyls *J. Phys. Chem. A* **2003**, *107*, 561-569.

(26) Andrews, L. Matrix Infrared Spectra and Density Functional Calculations of Transition Metal Hydrides and Dihydrogen Complexes *Chem. Soc. Rev.* **2004**, *33*, 123-132.

(27) Zhou, M.; Andrews, L.; Bauschlicher, C. W. Spectroscopic and Theoretical Investigations of Vibrational Frequencies in Binary Unsaturated Transition-Metal Carbonyl Cations, Neutrals, and Anions *Chem. Rev.* **2001**, *101*, 1931-1961.

(28) Zhou, M.; Andrews, L. Reactions of Laser-Ablated Co, Rh, and Ir with CO: Infrared Spectra and Density Functional Calculations of the Metal Carbonyl Molecules, Cations and Anions in Solid Neon *J. Phys. Chem. A* **1999**, *103*, 7773-7784.

(29) Wight, C. A.; Ault, B. S.; Andrews, L. Microwave-Discharge Sources of New Chemical Species for Matrix-Isolation Spectroscopy and Identification of Charged Species *J. Chem. Phys.* **1976**, *65*, 1244-1249.

(30) Jacox, M. E. Matrix-Isolation Study of Products of Interaction between Metastable Ar and Kr Atoms and Chloroform - Photodecomposition of $HCCl_2^+$ and $HCCl_2^-$ *Chem. Phys.* **1976**, *12*, 51-63.

(31) Jacox, M. E.; Thompson, W. E. The Production and Spectroscopy of Molecular-Ions Isolated in Solid Neon *Res. Chem. Intermed.* **1989**, *12*, 33-56.

(32) Forney, D.; Jakobi, M.; Maier, J. Absorption Spectroscopy of Mass-Selected Ions in Neon Matrices *J. Chem. Phys.* **1989**, *90*, 600-601.

(33) Godbout, J.; Halasinski, T.; Leroi, G.; Allison, J. Matrix Isolation of Mass-Selected Cations: Are Counterions Present and how are they Formed? *J. Phys. Chem.* **1996**, *100*, 2892-2899.

(34) Halasinski, T. M.; Godbout, J. T.; Allison, J.; Leroi, G. E. Infrared Detection of Matrix-Isolated, Mass-Selected Ions *J. Phys. Chem.* **1994**, *98*, 3930-3932.

(35) Bondybey, V.; Lorenz, M. Mass Selected Ions in Solid Neon: Matrix Damage and Site Effects *J. Low Temp. Phys.* **2001**, *122*, 509-525.

(36) Fulara, J.; Jakobi, M.; Maier, J. P. Electronic and Infrared-Spectra of $C_{60}^+$ and $C_{60}^-$ in Neon and Argon Matrices *Chem. Phys. Lett.* **1993**, *211*, 227-234.

(37) Harbich, W.; Fedrigo, S.; Buttet, J.; Lindsay, D. M. Optical Spectroscopy on Size Selected Gold Clusters Deposited in Rare-Gas Matrices *Zeitschrift Fur Physik D-Atoms Molecules and Clusters* **1991**, *19*, 157-159.

(38) Lindsay, D.; Meyer, F.; Harbich, W. Neutralization and Matrix Deposition Experiments on Mass-Selected Silver Atoms and Clusters *Zeitschrift Fur Physik D-Atoms Molecules and Clusters* **1989**, *12*, 15-18.

(39) Sabo, M.; Allison, J.; Gilbert, J.; Leroi, G. Bridging the Gap between what Mass Spectrometrists Want and what Spectroscopists can do - an Instrument for Spectroscopic Investigation of Matrix-Isolated, Mass-Selected Ions *Appl. Spectrosc.* **1991**, *45*, 535-542.

(40) Ludwig, R. M.; Moore, D. T. Formation of Ionic Complexes in Cryogenic Matrices: A Case Study using Co-Deposition of $Cu^-$ with Rare Gas Cations in Solid Argon *J. Chem. Phys.* **2013**, *139*, 244202.1-244202.9.

(41) Ludwig, R. M.; Moore, D. T. Chemical Reactions Triggered Using Electrons Photodetached from "Clean" Distributions of Anions Deposited in Cryogenic Matrices via Counterion Codeposition *J. Phys. Chem. Lett.* **2014**, *5*, 2947-2950.

(42) Huber, H.; Kundig, E. P.; Moskovits, M.; Ozin, G. A. Binary Copper Carbonyls - Synthesis and Characterization of $Cu(CO)_3$, $Cu(CO)_2$, CuCO, and $Cu_2(CO)_6$ *J. Am. Chem. Soc.* **1975**, *97*, 2097-2106.

(43) Ludwig, R. M. Simultaneous Counter-Ion Codeposition: A Technique Enabling Matrix Isolation Spectroscopy Studies Using Low-Energy Beams of Mass-Selected Ions, Lehigh Univserity, Bethlehem, PA, 2015.

(44) Haberland, H.; Karrais, M.; Mall, M. In *In A New Type of Cluster and Cluster Ion-Source;* Zeitschrift Fur Physik D-Atoms Molecules and Clusters; Springer Verlag: New York; 175 Fifth Ave, New York, NY 10010, 1991; Vol. 20, pp 413-415.

(45) Haberland, H.; Karrais, M.; Mall, M.; Thurner, Y. Thin Films from Energetic Cluster Impact: A Feasibility Study *J. Vac. Sci. Techol. A* **1992**, *10*, 3266-3271.

(46) Ibrahimkutty, S. Production, Deposition and Characterization of Metal Nanoclusters Using a Gas Aggregation Source, Doctoral Dissertation, University of Greifswald, 2005.

(47) Haberland, H.; Mall, M.; Moseler, M.; Qian, Y.; Reiners, T.; Thurner, Y. Filling of Micron-Sized Contact Holes with Copper by Energetic Cluster-Impact *J. Vac. Sci. & Technol. A* **1994**, *12*, 2925-2930.

(48) Smith, R.; Clampitt, R.; Lee, M. Magnetron-Based Nanocluster Source: Capabilities, Limitations and Future Possibilities, Technical Bulletin.

(49) Maier, J. P. Spectroscopic Characterization of Mass-Selected Ions *Mass Spectrom. Rev.* **1992**, *11*, 119-135.

(50) Munson, M.; Field, F. Chemical Ionization Mass Spectrometry .I. General Introduction *J. Am. Chem. Soc.* **1966**, *88*, 2621-2630.

(51) Vigasin, A.; Schriver-Mazzuoli, L.; Schriver, A. An Attempt to Systematize the Vibrational Shifts in $CO_2$ Monomers and Dimers Trapped in Various Matrices *J Phys Chem A* **2000**, *104*, 5451-5456.

(52) Schriver, A.; Schriver-Mazzuoli, L.; Vigasin, A. A. Matrix Isolation Spectra of the Carbon Dioxide Monomer and Dimer Revisited *Vib. Spectrosc.* **2000**, *23*, 83-94.

(53) Irvine, M.; Mathieson, J.; Pullin, A. The Infrared Matrix-Isolation Spectra of Carbon-Dioxide .2. Argon Matrices - the $CO_2$ Monomer Bands *Aust. J. Chem.* **1982**, *35*, 1971-1977.

(54) Guasti, R.; Schettino, V.; Brigot, N. Structure of Carbon-Dioxide Dimers Trapped in Solid Rare-Gas Matrices *Chem. Phys.* **1978**, *34*, 391-398.

(55) Castano, J. A. G.; Fantoni, A.; Romano, R. M. Matrix-isolation FTIR Study of Carbon Dioxide: Reinvestigation of the $CO_2$ Dimer and $CO_2 \cdot\cdot N_2$ Complex *J. Mol. Struct.* **2008**, *881*, 68-75.

(56) Fredin, L.; Nelander, B.; Ribbegard, G. On the Dimerization of Carbon Dioxide in Nitrogen and Argon Matrices *J. Mol. Spectroscopy* **1974**, *53*, 410-416.

(57) Thompson, W.; Jacox, M. E. The Vibrational Spectra of $CO_2^+$, $(CO_2)_2^+$, $CO_2^-$, and $(CO_2)_2^-$ Trapped in Solid Neon *J. Chem. Phys.* **1999**, *111*, 4487-4496.

(58) Thompson, W. E.; Jacox, M. E. The Vibrational-Spectra of Molecular-Ions Isolated in Solid Neon .7. $CO^+$, $C_2O_2^+$, and $C_2O_2^-$ *J. Chem. Phys.* **1991**, *95*, 735-745.

(59) Zhou, M.; Andrews, L. Infrared Spectra of the $CO_2^-$ and $C_2O_4^-$ Anions Isolated in Solid Argon *J. Chem. Phys.* **1999**, *110*, 2414-2422.

(60) Zhou, M.; Andrews, L. Infrared Spectra of the $C_2O_4^+$ Cation and $C_2O_4^-$ Anion Isolated in Solid Neon *J. Chem. Phys.* **1999**, *110*, 6820-6826.

(61) Jacox, M. E.; Milligan, D. E. Vibrational-Spectrum of $CO_2^-$ in an Argon Matrix *Chem. Phys. Lett.* **1974**, *28*, 163-168.

(62) Zhou, M.; Andrews, L. Infrared Spectra and Density Functional Calculations for OMCO, OM-(eta(2)-CO), $OMCO^+$, and $OMOC^+$ (M = V, Ti) in Solid Argon *J. Phys. Chem. A* **1999**, *103*, 2066-2075.

(63) Zhou, M.; Andrews, L. Infrared Spectra and Density Functional Calculations for OScCO, Sc-(eta(2)-OC)O, OSc-(eta(2)-CO), and three $OScCO^+$ Cation Isomers in Solid Argon *J. Am. Chem. Soc.* **1998**, *120*, 13230-13239.

(64) Zhou, M.; Liang, B.; Andrews, L. Infrared Spectra of OMCO (M = Cr-Ni), $OMCO^-$ (M = Cr-Cu), and $MCO_2^+$ (M = Co-Cu) in Solid Argon *J. Phys. Chem. A* **1999**, *103*, 2013-2023.

(65) Gutsev, G.; Bartlett, R.; Compton, R. Electron Affinities of $CO_2$, OCS, and $CS_2$ *J. Chem. Phys.* **1998**, *108*, 6756-6762.

(66) Hunter, E.; Lias, S. Evaluated Gas Phase Basicities and Proton Affinities of Molecules: An Update *J. Phys. Chem. Ref. Data* **1998**, *27*, 413-656.

(67) Lias, S. G.; Bartmess, J. E.; Liebman, J. F.; Holmes, J. L.; Levin, R. D.; Mallard, W. G. In *Ion Energetics Data;* Linstrom, P. J., Mallard, W. G., Eds.; NIST Chemistry WebBook, NIST Standard Reference Database Number 69; National Institute of Standards and Technology: Gaithersburg MD, 20899, .

(68) Schwentner, N.; Skibowski, M.; Steinmann, W. Photoemission from Valence Bands of Solid Rare-Gases *Phys. Rev. B* **1973**, *8*, 2965-2968.

(69) Tanaka, Y.; Jursa, A. S.; LeBlanc, F. J. Higher Ionization Potentials of Linear Triatomic Molecules $CO_2$, $CS_2$, COS, $N_2O$ *J. Chem. Phys.* **1958**, *28*, 350-351.

(70) Fisher, E.; Kickel, B.; Armentrout, P. Collision-Induced Dissociation and Charge-Transfer Reactions of $SF_x^+$ (X=1-5) - Thermochemistry of Sulfur Fluoride Ions and Neutrals *J. Chem. Phys.* **1992**, *97*, 4859-4870.

(71) Himpsel, F.; Schwentner, N.; Koch, E. Ultraviolet Photoemission Spectroscopy of Solid Nitrogen and Oxygen *Physica Status Solidi B-Basic Research* **1975**, *71*, 615-621.

(72) Schriver, A.; Schriver-Mazzuoli, L.; Vigasin, A. Matrix Isolation Spectra of the Carbon Dioxide Monomer and Dimer Revisited *Vib. Spectrosc.* **2000**, *23*, 83-94.

(73) Fleischman, S.; Jordan, K. Theoretical-Study of the Structures and Stabilities of the $(CO_2)_2^-$ Ions *J. Phys. Chem.* **1987**, *91*, 1300-1302.

(74) Saeki, M.; Tsukuda, T.; Nagata, T. Ab Initio Study of $(CO_2)_n^-$: Structures and Stabilities of Isomers *Chem. Phys. Lett.* **2001**, *340*, 376-384.

(75) Saeki, M.; Tsukuda, T.; Nagata, T. Ab Initio Study of $CO_2^-\cdot CO_2$ $C_2O_4^-$ Isomerization *Chem. Phys. Lett.* **2001**, *348*, 461-468.

(76) Herbert, J.; Ortiz, J. Ab Initio Investigation of Electron Detachment in Dicarboxylate Dianions *J. Phys. Chem. A* **2000**, *104*, 11786-11795.

(77) Sommerfeld, T.; Posset, T. Electron Attachment to $CO_2$ Clusters *J. Chem. Phys.* **2003**, *119*, 7714-7724.

(78) Mabbs, R.; Surber, E.; Velarde, L.; Sanov, A. Effects of Solvation and Core Switching on the Photoelectron Angular Distributions from $(CO_2)_n^-$ and $(CO_2)_n^- \cdot H_2O$ *J. Chem. Phys.* **2004**, *120*, 5148-5154.

(79) Tsukuda, T.; Johnson, M.; Nagata, T. Photoelectron Spectroscopy of $(CO_2)_n^-$ Revisited: Core Switching in the $2 \leq n \leq 16$ Range *Chem. Phys. Lett.* **1997**, *268*, 429-433.

(80) Shin, J.; Hammer, N.; Johnson, M.; Schneider, H.; Gloss, A.; Weber, J. An Infrared Investigation of the $(CO_2)_n^-$ Clusters: Core Ion Switching from both the Ion and Solvent Perspectives *J. Phys. Chem. A* **2005**, *109*, 3146-3152.

(81) Mabbs, R.; Surber, E.; Sanov, A. An Experimental Manifestation of Distinct Electronic-Structural Properties of Covalent Dimer Anions of $CO_2$ and $CS_2$ *Chem. Phys. Lett.* **2003**, *381*, 479-485.

(82) Jacox, M. E.; Thompson, W. E. The Vibrational-Spectra of Molecular-Ions Isolated in Solid Neon .1. $CO_2^-$ and $CO_2^-$ *J. Chem. Phys.* **1989**, *91*, 1410-1416.

(83) Cooper, C. D.; Compton, R. N. Metastable Anions of $CO_2$ *Chem. Phys. Lett.* **1972**, *14*, 29-32.

(84) Alexander, M. L.; Johnson, M. A.; Levinger, N. E.; Lineberger, W. C. Photodissociation of Mass-Selected $(CO_2)_n^-$ Clusters - Evaporation Leading to Magic Numbers in Fragment-Ion Distributions *Phys. Rev. Lett.* **1986**, *57*, 976-979.

(85) Sanov, A.; Lineberger, W. C. Cluster anions: Structure, Interactions, and Dynamics in the Sub-Nanoscale Regime *Phys. Chem. Chem. Phys.* **2004**, *6*, 2018-2032.

(86) Deluca, M. J.; Niu, B.; Johnson, M. A. Photoelectron-Spectroscopy of $(CO_2)_2^-$ Clusters with $2 \leq N \leq 13$ - Cluster Size Dependence of the Core Molecular Ion *J. Chem. Phys.* **1988**, *88*, 5857-5863.

(87) Felder, P.; Gunthard, H. Freezing of Conformational Isomer Distribution in a Supersonic Jet Detected by Matrix Infrared-Spectroscopy *J. Mol. Struct.* **1980**, *60*, 297-300.

(88) Huber-Walchli, P.; Gunthard, H. Trapping of Unstable Molecular-Conformations in Argon Matrices - Gauche-1,2-Difluoroethane and Trans-1,2-Difluoroethane *Chem. Phys. Lett.* **1975**, *30*, 347-351.

(89) Schweiger, A.; Wolf, R.; Gunthard, H.; Ammeter, J.; Deiss, E. Proton Hyperfine Data and Temperature-Dependence of the Dynamics of Ring Rotation in Bis-Benzene-Vanadium - a Powder Endor Study *Chem. Phys. Lett.* **1980**, *71*, 117-122.

(90) Serrallach, A.; Meyer, R. Rotamer Interconversion of Partially Deuterated Methanol Species in Rare-Gas and Nitrogen Matrices *J. Mol. Spectrosc.* **1976**, *60*, 246-258.

(91) Barnes, A. J.; Whittle, G. C. In *In Molecular Spectroscopy of Dense Phases;* Proc. 12th European Congress on Molecular Spectroscopy; 1976.

(92) Murto, J.; Kivinen, A.; Mutikainen, I. Reversible Temperature Effects in Matrix IR-Spectra of Halogenated 2-Propanols *Chem. Phys. Lett.* **1975**, *36*, 369-371.

(93) Barns, A. J. In *Conformational Isomerism Studied by Matrix Isolation Vibrational Spectroscopy;* Orville-Thomas, W. J., Barnes, A. J., Muller, A. and Gaufres, R., Eds.; Matrix Isolation Spectroscopy; D. Reidel Publishing Company: Dordrecht, 1981; pp 531-550.

(94) Misochko, E. Y.; Akimov, A. V.; Goldschleger, I. U.; Boldyrev, A. I.; Wight, C. A. Endothermic Formation of a Chemical Bond by Entropic Stabilization: Difluoronitroxide Radical in Solid Argon *J. Am. Chem. Soc.* **1999**, *121*, 405-410.

(95) Eyring, H. The Activated Complex in Chemical Reactions *J Chem Phys* **1935**, *3*, 107-115.

(96) Evans, M. G.; Polanyi, M. Some Applications of the Transition State Method to the Calculation of Reaction Velocities, Especially in Solution *Trans. Faraday Soc.* **1935**, *31*, 875-894.

(97) Steinfeld, J. I.; Francisco, J. S.; Hase, W. L. *Chemical Kinetics and Dynamics;* Winget, K., Ed.; Prentice Hall: Englewood Cliffs, NJ, 1989.

(98) Andrews, L. Infrared Spectra of Free Radicals and Chemical Intermediates in Inert Matrices *Annu. Rev. Phys. Chem.* **1971**, *22*, 109-132.

(99) Jacox, M. E. The Infrared Spectroscopy of the Products of Ion-Molecule Reactions Trapped in the Solid Rare Gases *Int. J. Mass Spectrom.* **2007**, *267*, 268-276.

(100) Andrews, L. Spectroscopy of Molecular-Ions in Noble-Gas Matrices *Annu. Rev. Phys. Chem.* **1979**, *30*, 79-101.

(101) Kasai, P. Generation and Trapping of Charged Species in Rare-Gas Matrix at 4 Degrees K - ESR Spectra of $Cd^+$ $Cr^+$ and $Mn^+$ *Phys. Rev. Lett.* **1968**, *21*, 67-69.

(102) Suzer, S.; Andrews, L. Matrix-Isolation Study of Electron-Impact on $H_2O^-$ Infrared-Spectrum of $OH^-$ in Solid Argon *J. Chem. Phys.* **1988**, *88*, 916-921.

(103) Thompson, W. E.; Jacox, M. E. The Vibrational-Spectra of Molecular-Ions Isolated in Solid Neon .2. $O_4^+$ and $O_4^-$ *J. Chem. Phys.* **1989**, *91*, 3826-3837.

(104) Godbout, J. T.; Halasinski, T. M.; Leroi, G. E.; Allison, J. Matrix Isolation of Mass-Selected Cations: Are Counterions Present and how are they Formed? *J. Phys. Chem.* **1996**, *100*, 2892-2899.

(105) Jacox, M. The Reaction of F-Atoms with CO in an Argon Matrix - Vibrational and Electronic-Spectra of FCO *J. Mol. Spectrosc.* **1980**, *80*, 257-271.

(106) Swanson, B.; Jones, L. Matrix-Molecule Interactions, Dynamics, and Exchange Phenomena in Low-Temperature Matrices - $SF_6$ in Argon and Krypton *J. Chem. Phys.* **1981**, *74*, 3205-3215.

(107) Lugez, C.; Jacox, M.; King, R.; Schaefer, H. Experimental and Ab Initio Study of the Infrared Spectra of Ionic Species Derived from $SF_6$ and $SF_5$ and Trapped in Solid Neon *J. Chem. Phys.* **1998**, *108*, 9639-9650.

(108) Smardzewski, R.; Fox, W. Vacuum UV Photolysis of Sulfur-Hexafluoride and its Derivatives in Argon Matrices - IR-Spectrum of $SF_5$ Radical *J. Chem. Phys.* **1977**, *67*, 2309-2316.

(109) Hassanzadeh, P.; Andrews, L. Matrix Reactions of Sulfur-Atoms and Fluorine - Infrared-Spectra of SF, $SF_2$, and $SF_3$ in Solid Argon *J. Phys. Chem.* **1992**, *96*, 79-84.

(110) Huey, L.; Hanson, D.; Howard, C. Reactions of $SF_6^-$ and $I^-$ with Atmospheric Trace Gases *J. Phys. Chem.* **1995**, *99*, 5001-5008.

(111) Hearn, J.; Smith, G. A Chemical Ionization Mass Spectrometry Method for the Online Analysis of Organic Aerosols *Anal. Chem.* **2004**, *76*, 2820-2826.

**Michael E. Goodrich**

**Curriculum Vita**

Institutional Address:
Lehigh University
Chemistry Department
6 East Packer Ave.
Bethlehem, PA 18105

## EDUCATION

Ph.D., Physical Chemistry, Lehigh University, Chemistry Department 2017
Research Advisors: Dr. David T. Moore and Dr. Xiaoji Xu
B.S., Chemistry, Muhlenberg College, Chemistry Department 2011

## DISSERTATION

Matrix-Isolation studies of ionic $CO_2$ clusters and improvements on the counter ion co-deposition technique

## TEACHING EXPERIENCE

### Lehigh University

General Chemistry Laboratory (Instructor: Spring 2017)
(Teaching Assistant: Fall 2012 – Summer 2013)
Physical Chemistry Laboratory (Teaching Assistant: Fall 2013 – Spring 2016)

### Manuscripts in Preparation

Goodrich, M. E.; Moore, D. T. Simultaneous Deposition of Mass Selected Anions and Cations: Improvements in Ion Delivery for Matrix Isolation Experiments

Goodrich, M. E.; Moore, D. T. Characterization of a Matrix-Isolated Thermodynamic Equilibrium of Isomerization of Dimeric $CO_2$ Anions

## CONFERENCE PARCIPITATION

### Oral Presentations

2016 Michael E. Goodrich, David T. Moore "Low Temperature Thermodynamic Equilibrium of $CO_2$ Dimer Anion Species in Cryogenic Argon and Krypton Matrices." 71$^{st}$ Meeting: International Symposium on Molecular Spectroscopy, Champaign-Urbana, Illinois, June 20-24, 2016

2016 Michael E. Goodrich, David T. Moore, "Simultaneous Deposition of Mass Selected Anions and Cations: Improvements in Ion Delivery for Matrix Isolation Experiments" 71st Meeting: International Symposium on Molecular Spectroscopy, Champaign-Urbana, Illinois, June 20-24, 2016

2014 Michael E. Goodrich, David T. Moore, "Carbon Dioxide Clusters and Copper Complexes Formed in Argon Matrices" 69th Meeting: International Symposium on Molecular Spectroscopy, Champaign-Urbana, Illinois, June 16-20, 2014

## RESEARCH EXPERIENCE

### Dissertation Research

Studied ion behavior and interactions in cryogenic matrices using the counter ion co-deposition technique

Helped to design and install a new chamber for existing high vacuum matrix deposition system

Performed first deposition of simultaneously mass selected beams of anions and cations into a cryogenic matrix

Discovered and performed kinetic and thermodynamic characterizations of a matrix-isolated low temperature equilibrium of dimeric $CO_2$ anions

Designed and constructed gas mixing and deposition lines for the controlled delivery of gases for matrix-isolation experiments

### Undergraduate Research

Developed improved methods for the laser synthesis of linear polyynes

Analyzed products using IR spectroscopy and GC/MS

## PROFESSIONAL AFFILIATIONS

2015 American Chemical Society